Inkjet Printing of Inks of Large Flakes of Reduced Graphene Oxide

A thesis submitted to The University of Manchester
for the degree of Doctor of Philosophy in the Faculty of Science and Engineering

2023

Wentao Zou

School of Natural Sciences

Department of Materials

Contents

Word count: 50063

List of Figures

List of Tables

List of Symbols and Abbreviations

0 D	0 Dimension
1 D	1 Dimension
2 D	2 Dimension
3 D	3 Dimension
AFM	Atomic force microscope
Ar	Argon
ATRP	Atoms transfer radical polymerization
CCA	Constant contact angle
CCD	Constant contact diameter
CIJ	Continuous inkjet
CMC	Critical micelle concentration
C-ME	Co-solvents induced Marangoni effect
CNT	Carbon nanotube
CO	Carbon monoxide
CO_2	Carbon dioxide
CRE	Coffee ring effect
CVD	Chemical vapor deposition
DMF	Dimethylformamide
DMSO	Dimethyl sulfoxide
DOD	drop-on-demand
DI	Deionized water
EC	Ethyl cellulose
EDL	Electrostatic double layer
EG	Ethylene glycol
GNP	Graphene nanoplatelet
GO	Graphene oxide
H_2O_2	Hydrogen peroxide
H_2SO_4	Sulfuric acid
H_3PO_4	Phosphoric acid
HI	Hydrogen iodide
HNO_3	Nitric acid
IR	Infrared
$KClO_3$	Potassium chlorate
$KMnO_4$	Potassium permanganate
L-AA	L-ascorbic acid
LPE	Liquid phase exfoliation
MPF	Maximum printing frequency
N_2H_4	Hydrazine
$NaBH_4$	Sodium borohydride
$NaNO_3$	Sodium nitrate
NMP	N-methyl pyrrolidone
Oh	Ohnesorge number
PAH	Polyaromatic hydrocarbon
PEDOT:PSS	Poly(3,4-ethylene dioxythiophene):poly(styrene sulfonate)
PI	Polyimide
PL	Photoluminescence

PSA	Sodium pyrene-1-sulfonate
PVA	Polyvinyl alcohol
PVP	Polyvinylpyrrolidone
QHE	Quantum Hall effect
Re	Reynolds number
rGO	Reduced graphene oxide
SC	Sodium cholate
SEM	Scanning Electron Microscopy
SDS	Sodium dodecyl sulfate
SiC	Silicon carbide
STEM	Scanning Transmission Electron Microscopy
S-ME	Surfactant induced Marangoni effect
We	Weber number
WHL	White Light Interferometry
XPS	X-ray photoelectron spectroscopy
ZA phonon	Out-of-plane acoustic transport of phonon
ρ_{xy}	Hall resistance
S	Spreading coefficient
γ	Surface energy/tension

List of Appendix

Abstract

The graphene-related materials frequently used for flexible and transparent electrodes (FTEs) — graphene oxide (GO) and graphene nanoplatelets — suffer from the insulating nature or the limited flake size, which degrades the electrical conductivity and limits the available range of substrate of FTEs. Another derivative of graphene, reduced graphene oxide (rGO), is used in the project due to its relative advantages in conductivity and flake size compared to the other two materials.

This project aims to use the advantages of this material to prepare a series of novel inkjet printable large rGO inks, which can overcome the above challenges at the same time. This project also aims to be the first to formulate this type of ink with water as the main solvent which make the ink more eco-friendly as well.

In this project, we used a team-made polyaromatic hydrocarbon stabiliser to prepare large rGO water-based inks due to its high stabiliser/graphene ratio and check inkjet printability of these inks on the picolitre printhead based on the reported inkjet printability of ultra-large GO flakes through similar type of printhead in microlitre. Then, advantages of rGO could be applied in the preparation of printed FTEs with higher resolutions.

During the printing of these rGO inks, a new waveform was developed to suppress the satellite issue due to their rheological properties. Two unique drying issues were observed during exploration, missing front and waviness (in printed squares only). The first dot problem, which is common in inkjet printing leads to the first issue. The dual-ring structure with a depletion zone in dried dot, which causes miss setting of drop spacing is the key of second issue. The satellites issue can be suppressed by adding an extra filtering step before printing. To supress the waviness, the effects of printer settings, ink formulations, and substrate treatments on droplet drying were investigated. The strong Marangoni effect is the critical factor causing this unique structure and it can be controlled by optimising ink formulation and substrate treatments. Then, a guide of how to prepare this new type of rGO ink without major issues was concluded in this project.

Finally, it was the first time that DMC-11610 printhead successfully printed a rGO water-based ink with average flake size up to 1.5 µm. This achievement expands the potential of rGO as a functional material for future printed FTEs.

Declaration

No portion of the work referred to in the thesis has been submitted in support of an application for another degree or qualification of this or any other university or other institute of learning.

Copyright Statement

i. The author of this thesis (including any appendices and/or schedules to this thesis) owns certain copyright or related rights in it (the "Copyright") and he has given The University of Manchester certain rights to use such Copyright, including for administrative purposes.

ii. Copies of this thesis, either in full or in extracts and whether in hard or electronic copy, may be made only in accordance with the Copyright, Designs and Patents Act 1988 (as amended) and regulations issued under it or, where appropriate, in accordance with licensing agreements which the University has from time to time. This page must form part of any such copies made.

iii. The ownership of certain Copyright, patents, designs, trademarks and other intellectual property (the "Intellectual Property") and any reproductions of copyright works in the thesis, for example graphs and tables ("Reproductions"), which may be described in this thesis, may not be owned by the author and may be owned by third parties. Such Intellectual Property and Reproductions cannot and must not be made available for use without the prior written permission of the owner(s) of the relevant Intellectual Property and/or Reproductions.

iv. Further information on the conditions under which disclosure, publication and commercialisation of this thesis, the Copyright and any Intellectual Property and/or Reproductions described in it may take place is available in the University IP Policy (see http://www.campus.manchester.ac.uk/medialibrary/policies/intellectual-property.pdf), in any relevant Thesis restriction declarations deposited in the University Library, The University Library's regulations (see http://www.manchester.ac.uk/library/aboutus/regulations) and in The University's policy on presentation of Theses.

Acknowledgements

I would like to thank many people for their support and advice during my Ph.D. First of all, I would like to thank my supervisor, Professor Aravind Vijayaraghavan, for his guidance in this research area. His patient guidance and sincere advice were the greatest support for my Ph.D. Also, I would like to thank him for his understanding and help with my health condition during the time.

In addition, I would like to thank all the colleagues in my group and the staff of the National Graphene Institute (NGI), especially Mr. Robert Mcmaster, Dr. Adam Parry. Furthermore, I would like to especially thank Dr. Rachel Saunders for her genuine help with my equipment training. I would also like to thank Dr. Jinxing Yang, Dr. Fei Zheng and Mr. Andy Wallwork for their help in my study. I would also like to thank Professor Mike Turner and Dr. Steve Edmondson for their support of my project and advice for the annual viva. I would also like to thank Mr Andrij Zadoroshnyj, Mrs Polly Greensmith and other support staff in the Department of Materials.

Moreover, I would thank Dr. Dai Luan, Miss Kaiwen Nie, Dr. Yizheng Shao, Dr Boyang Mao, Professor Fengchao Wang, Dr Yang Su and Professor Kaige Zhou for their sincerely supports. The full list of people I want to thank is endless. I want to thank you all for giving me such wonderful and meaningful life in Manchester.

Last but not the least, I want to thank my family. Without their support, I would not go this far. Their unconditional supporting and caring through all these years is the spring of my faith and life. Thank you all.

The truth is rarely pure and never simple.

Oscar Wilde

Chapter 1. Introduction

Graphene has been intensively studied since 2004 due to its remarkable physicochemical properties[1]. Graphene is a one-atom thick, two-dimensional material in which sp^2 hybridised carbon atoms are configured in a hexagonal structure. Figure 1 illustrates the structure of graphene and its function as the building block for other carbon allotropes, such as C_{60} (zero-dimensional), carbon nanotube (one-dimensional), and graphite (three-dimensional)[2]. Graphene has numerous fascinating properties, such as high strength and stiffness (up to 130 GPa tensile strength and 1 TPa Young's modulus)[3], up to 5300 W/mK thermal conductivity at ambient temperature[4], electron ballistic transport (at the micrometre scale) in ambient condition[5], and 2.3% of visible light absorption per layer[6]. These properties make it a promising candidate for various applications in areas such as energy storage[7], composites[8], sensors[9], transistors[10], optoelectronics[11], and flexible electronics[12], among others. In particular, inkjet printing of graphene-based flexible and transparent electrodes (FTEs) has grown in popularity in recent years[13].

Inkjet printing is one of the popular techniques to achieve low-cost, high-efficiency, and mass production of electronic products. It has advantages in printing speed, precision, and resolution compared to others. At the same time, it can deposit material onto a substrate without any contact, making it an ideal tool

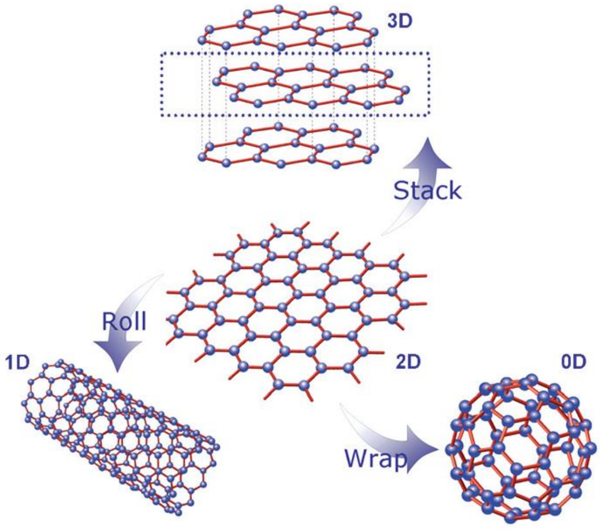

Figure 1 2D structure of graphene and its function as a building block for carbon allotropes in other dimensions, such as graphite (3D), carbon nanotube (1D), and Fullerenes (0D)[2].

for fabricating flexible electronics[14]. Hence, it is used as the printing technique in this project, and the terms ‘printed/printings’ used in this project all refer to inkjet printing unless otherwise specified. Pristine graphene is not an ideal material for the preparation of graphene-based inks due to its sophisticated production method[15]. Rather, graphene oxide (GO) and graphene nanoplatelets (GNPs) are the most used materials in inkjet printing, as the techniques for mass production of these two materials are established and cost-effective[13,16,17].

GO-based inks have advantages like high graphene loading and large flake size[13]. However, the reduction of the process of printed GO is always necessary for this type of ink. This process usually applies either high-temperature annealing or a strong reducing agent, which severely limits the available substrates for the final applications, especially for FTEs. GNP-based inks generally have better electrical conductivity[13]. However, aggressive production methods typically limit the flake size of GNPs and lead to increased contact resistance of final printed patterns, which further restricts the electrical, mechanical, and optical properties of final FTEs[13].

By contrast, rGO-based inks may have the opportunity to combine the advantages of both GO and GNPs at the same time[13]. Since GO is the precursor of rGO, rGO capitalises on GO’s advantages, like hydrophilicity and flake size during ink preparation. In the meantime, rGO’s electrical conductivity is better than GO’s, as more sp^2 domains are restored in its structure. Additionally, the reported printability of ultra-large GO flakes indicates that printing large 2D flakes from small nozzles is possible with the help of laminar flow[18]. Thus, the formulation of an inkjet printable large rGO water-based ink for picolitre printhead may be a new route for preparing high-quality, printed FTEs as no such type of ink has been formulated yet. This project aims to be the first to investigate the printability of large rGO flakes on Dimatix DMC-11610 printhead and to determine the preparation of this type of water-based ink, as no inkjet printable large rGO water-based inks have yet been reported. In addition, the use of water as the main solvent can both reduce the difficulty of the annealing process and make the ink more environmentally friendly.

Since the aim of this project is to formulate a series of novel large rGO water-based inks suitable for inkjet printing of FTEs, several suggested criteria for the ideal inks are proposed based on the existing requirements[19,20,21]:

(1) rGO loading around 1 mg/ml;
(2) sheet resistance below 100 Ω/□;
(3) visible light transparency of approximately 90%;
(4) stable sheet resistance after hundreds of bending cycles.

In order to achieve the goal of this project, four major steps have been conducted:

(1) Formulation and printing of Ink 1 (0.25 mg/ml rGO, 0.1/1 [by volume] EG/DI, 0.1 mg/ml Triton X-100, short for 'Ink 1-(0.25rGO, 0.1/1EG, 0.1Tri)-1.5µm' in following sections) with different flake sizes;
(2) Suppression of drying issues of Ink 1-(0.25rGO, 0.1/1EG, 0.1Tri)-1.5µm via the printer settings and substrate modifications;
(3) Exploration of the suppression of the drying issues by various ink formulations and substrate modifications;
(4) Printing of the inks formulated based on the guideline proposed from step (3).

The aim of step (1) is to check the printability, specifically the upper limits of the printable size, of inks loaded with large rGO flakes. Three major flake sizes (1.5, 5.8, and 11.8 µm) of rGO are printed from Dimatix DMC-11610 printhead. Meanwhile, a modified waveform is applied to suppress the satellites issue, so the jetting stability of Ink 1-(0.25rGO, 0.1/1EG, 0.1Tri)-1.5µm could be controlled during the printing process. Finally, the successful printing of Ink 1-(0.25rGO, 0.1/1EG, 0.1Tri)-1.5µm serves as a milestone of this step.

Step (2) suppresses the drying issues found during the printing of Ink 1-(0.25rGO, 0.1/1EG, 0.1Tri)-1.5µm via different printer settings and substrate modifications. Four major drying issues are discovered in this step, which are the coffee-ring effect (CRE), first dot issue, missing front, and waviness. Various printer settings and substrate modifications are selected to explore their effects on the suppression of these issues. The maximum printing frequency (MPF), drop spacing, and UV time are mainly used to explore the relationship between droplet coalescence and drying issues. Subsequently, the cartridge and platen temperatures are used to explore the relationship between the evaporation rate and drying issues. This step's milestone is to provide a set of optimised printer settings and substrate modifications for future printing. Additionally, this step addresses the mechanisms behind the missing front and waviness issues and suggests that the printer settings and substrate modifications only have limited effects on drying issues.

Step (3) explores the relationship between ink formulation and drying issues. The exploration is conducted by placing sessile droplets from various formulations on the modified substrates. A new formulation and a certain combination of substrate modifications are set as a reference point. The first exploration investigates how changes in individual formulation and substrate modification factors affect the drying of droplets. Then, the effects of the modifiers on droplet drying are explored. The modifiers are the mixture of EG and Triton, used for modulating the rheological properties of the inks. After that, the effects of rGO loading, platen temperature, and UV time on the grouping effect of modifiers have been further investigated. Thus, a guideline of how to formulate ideal inks concludes this step.

In the final step, seven inks are formulated and printed based on the guidelines from the previous step. The Ink 1 – 1.5 µm (0.25rGO, 0.1/1EG, 0.1Tri) is used as the starting point, as it is easy to compare the difference before and after the application of the guidance. However, further exploration on reduction of resistance, among other topics, could not be done due to the COVID-19 pandemic; thus, the project stops at this step.

All in all, this project is motivated by the high stabiliser/graphene ratio of polyaromatic hydrocarbons stabiliser and the printability of ultra-large GO. So, the aim is to prepare a series of novel inkjet printable large rGO inks to fill the gap of printing large rGO flakes form picolitre printhead. Thus, both the advantages of large flake size and properties of rGO could be applied in the preparation of future FTEs.

Chapter 2 Literature review

2.1 Synthesis of GO

2.1.1 GO structure and oxidation methods

Figure 2 The GO structure proposed by Lerf and Klinowski, wherein the majority of hydroxyl and epoxy groups are located on the basal plane, and most carboxylic acid groups are located at the edge[22].

GO is a popular option for the mass production of graphene due to its simplicity and high yield. The preparation of GO can be divided into two steps: (1) oxidation of graphite and (2) exfoliation of graphite oxide[23]. Accurate structure prediction of GO remains challenging due to limitations in analysis techniques, and it is believed that its structure is largely dependent on the structure and oxidation process of the graphite used[24,22]. Figure 2 illustrates a widely accepted GO structure, which is supported by transmission electron microscopy (TEM) observations[25,26]. In this structure, graphene-like sp^2 domains and distorted sp^3 domains are randomly distributed throughout the structure, and the hydroxyl and epoxy groups are concentrated on the basal plane, while carboxylic acid groups are often located at the edges of the structure[22].

Table 1 presents the evolution of the GO oxidation method. The first method – Brodie's method – was developed in 1859[27]. In this technique, potassium chlorate ($KClO_3$) and fuming HNO_3 are used to oxide the graphite. The collected compound has a C:H:O ratio of 61.04: 1.85: 37.11. While this method is a pioneer in GO research, it has many limitations, as it is a time-consuming process (usually 3 – 4 days), and it releases toxic gas (mainly ClO_2). Moreover, $KClO_3$ is potentially explosive, which greatly limits the safety of this method. Therefore, it is no longer used widely. Following this, an improved method was proposed in 1898 by L. Staudenmaier[28].

Method	**Brodie (1859)[27]**	**L. Staudenmaier (1898)[28]**	**Hofmann (1937)[29]**	**Hummer (1958)[30]**	**Modified Hummer (1999)[31]**
Materials	Graphite; Fuming HNO_3; $KClO_3$	Graphite; Fuming HNO_3; $KClO_3$; Conc. H_2SO_4	Graphite; Conc. HNO_3; $KClO_3$; Conc. H_2SO_4	Graphite; Conc. H_2SO_4; $KMnO_4$; $NaNO_3$	Graphite; Conc. H_2SO_4; $KMnO_4$; $NaNO_3$; $K_2S_2O_4$; P_2O_5
Pros	Pioneer in the area	Simplification of the oxidation process; Increase in the oxidation degree of GO	Improvements in safety	Short reaction time (up to hours)	Short reaction time (up to hours); Improvements in the yield of GO
Cons	Long reaction time (up to days); Toxic gas (ClO_2); Potential explosive ($KClO_3$)	Long reaction time (up to days); Toxic gas (ClO_2); Potential explosive ($KClO_3$)	Long reaction time (up to days); Toxic gas (ClO2); Potential explosive (KClO3)	Toxic gases (ClO_2, NO_x); Potential explosive intermediate (Mn_2O_7); Large amount of unoxidised graphite	Toxic gases (ClO_2, NO_x); Potential explosive intermediate (Mn_2O_7)

Table 1 The evolution of historical methods used for GO synthesis is presented and compared with information on the major materials used and the main limitations and advantages of these methods.

The main differences between these two methods are the use of excessive oxidising agent ($KClO_3$) and concentrated H_2SO_4. With these, the oxidation degree of graphite is further increased and can be completed in one step. Hence, the preparation process is simplified. However, the drawbacks of this method remain the same as Brodie’s method. Therefore, further modifications were needed. The fuming HNO_3 used in the previous method was replaced with concentrated HNO_3 in 1937 to improve the safety of the entire process by Hofmann[29]. Nonetheless, other limitations remain. The next widely used method for GO research was proposed in 1958[30]. Hummers and his colleagues used a mixture of concentrated H_2SO_4, $NaNO_3$, and $KMnO_4$ to oxidise the graphite powder. The oxidation time can be shortened to about 2 hours, and the fuming nitric acid is avoided. Both the production time and safety of this method had been improved compared to previous methods. However, the intermediate Mn_2O_7 is potentially explosive, which requires adequate control of the experiment. In the meantime, the release of toxic gases (NO_x) is still a challenge of this method. In addition, Hummer’s method leaves a large amount of unoxidised graphite after production, which limits the yield of GO. Therefore, various modifications have been applied to this method to overcome this issue, such as using $K_2S_2O_4$ and P_2O_5 to conduct a pre-oxidation of graphite[31], adding additional $KMnO_4$[32], or using high-mesh graphite[33], among others. All these methods are classified as modified Hummer's methods and have become common options for GO production in recent years. Generally, these methods increase the oxidation degree of graphite by pre-treating the material, adding additional oxidising agents, or using exfoliated graphite. Thus, the final yield of GO is increased with these methods. Furthermore, another improved Hummer's method was reported in 2010 and is shown in figure 3[16].

The improved method demonstrates advantages in oxidation efficiency by excluding the $NaNO_3$ and adding more $KMnO_4$. Additionally, a ratio of 9:1 of H_2SO_4:H_3PO_4 mixture was used to improve the oxidation efficiency. The process generates no toxic gases due to the absence of $NaNO_3$, and the oxidation degree has been improved compared to the original Hummers' method. However, the modified Hummer's method is still challenged by the explosive intermediate Mn_2O_7 and requires careful control of the experiment.

In all, the oxidation method for producing GO has been continuously improved. The initial problems were the release of toxic gases, the use of explosives, and the time-consuming process. After Hummer's method was proposed, the oxidation time reduced from days to hours.

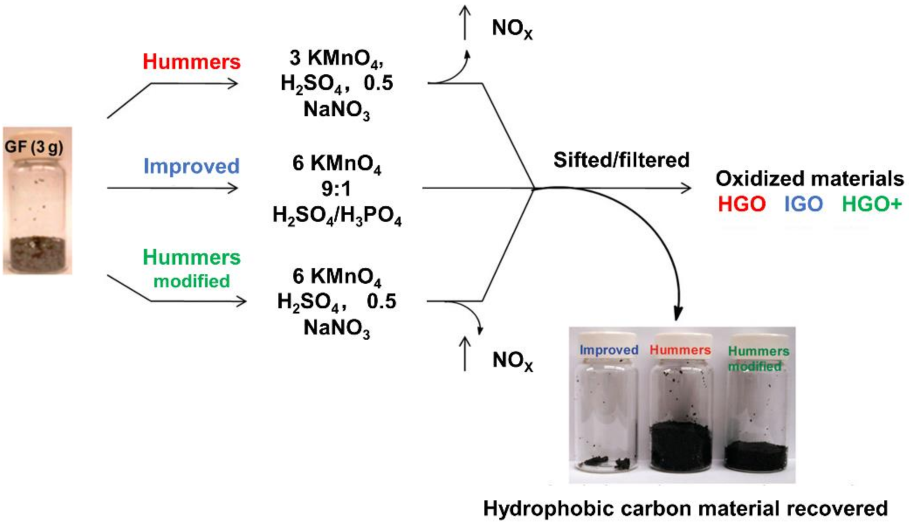

Figure 3 Illustration of GO synthesis via different Hummers' methods, which are Hummers' method and improved and modified Hummers' methods. The minimal hydrophobic carbon residuals are found in the improved method, which means it has the best oxidisation effect among these three methods[16].

Although Hummer's method still has limitations, like low yield, explosive intermediates, and release of toxic gases, the short oxidation time has made it a popular option in GO production.

2.1.2 Oxidation mechanisms and preparation of large GO

The mechanism of the modified Hummer's method is presented in figure 4[34]. The process can generally be divided into three steps:

(1) intercalation of acid molecules;
(2) diffusion of oxidising agents;
(3) exfoliation of graphite oxide.

In the first step, an intercalation compound of sulfuric acid and graphite is formed. The acid molecules intercalate into the layers of graphite from the edge to the centre after mixing these two materials. Then, the oxidising agents diffuse into the graphite interlayers and replace the acid molecules to oxidise the carbon atoms in the graphite. Thus, the graphite oxide has been formed in this step. Subsequently, the graphite oxide is transformed into GO by soaking it in water.

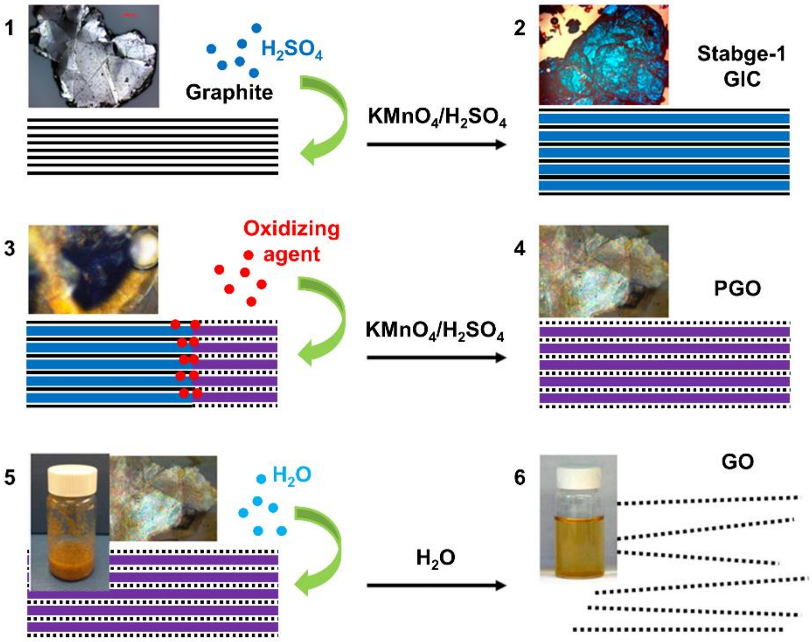

Figure 4 Diagrams of how graphite is oxidised and transformed into GO. The microscopy images and sample photos of different stages during the oxidation process are accompanied by illustrations of the oxidation mechanism of each step. Intercalation (1 – 2), diffusion (3 – 4), and exfoliation (4 – 5) are the three main steps of GO preparation in the modified Hummer's method[34]. The acid molecules intercalate into the layers of graphite from edge to centre in the first step, and then the oxidising agents diffuse into the graphite interlayers and replace the acid molecules to oxidise the carbon atoms in graphite. The final step is to exfoliate the graphite oxide into GO by soaking it in water.

Graphite oxide has numerous oxygen-containing groups in its structure after its oxidation and becomes extremely hydrophilic. Simultaneously, the interlayer distance is increased due to the addition of these functional groups; this results in weakened interactions between the layers. Therefore, the water molecules easily penetrate the structure and exfoliate the graphite oxide[34]. However, the exfoliation efficiency of graphite oxide by water only is considered low, and additional sonication is required unless the graphite is fully oxidized[35].

The pursuit of large GO flakes is also an important goal of this project, as it can effectively reduce the contact resistance of the final printed pattern. The desired characteristic of large GO flakes depend on their final application. For example, for inkjet printing, any flake larger than 1/50 the size of the nozzle diameter is considered a large flake[36]. Thus, flakes with a lateral size > 430 nm are denoted as large for this project. The main restrictions of GO flake size are the oxidising cutting and mechanical cutting of the flakes during the preparation process. Thus, various methods have been used to obtain large GO flakes, which can be divided into four categories[37]:

(1) using large graphite flakes;
(2) optimising the oxidation process of GO;
(3) optimising the exfoliation process of GO;
(4) using expanded graphite.

The use of large graphite flakes is the most direct method to obtain large GO, as it does not require any changes to the oxidation or exfoliation processes. The combination of the typical modified Hummer's method and sonication is enough to obtain GO with average flake sizes up to approximately 36 µm[18]. In addition, sieved graphite[38] and mild sonication[32] have also been applied to generate large graphite flakes, and the average flake sizes of GO were approximately 38 µm and 83 µm, respectively. However, these methods yield low amounts of large GO, and size-fractionation is time-consuming. In addition, the main reason large GO is obtained in this method is attributed to the large size of the graphite flakes, but the oxidising and mechanical cutting of GO flakes are not controlled.

The second method aims to optimise the oxidation process of GO by controlling the oxidising cutting of GO. Two-step oxidation has been applied to achieve this goal. In general, concentrated H_2SO_4 is used to conduct a pre-oxidation of used graphite, and a mild sonication process is applied to perform a pre-exfoliation at this step. Then, the collected mixture goes through the modified Hummer's method with a less vigorous oxidation process. Thus, the oxidising cutting of GO is controlled, and large GO flakes up to approximately 100 µm can be obtained[39,40]. However, the low yield and the time-consuming size-fractionation of large GO flakes remain challenges for this method. Notably, the use of two-step oxidation minimises the oxidising cutting rather than increases the oxidation degree, which is different from some modified Hummer's methods[31].

As for the mechanical cutting of flake size, small molecules like CO_2 and tetrabutylammonium hydroxide (TBA) have been used to replace sonication to achieve a gentle exfoliation process[41,42]. In the case of CO_2, the rapid melting of dry ice and the release of CO_2 increase the pressure between the interlayer of graphite oxide and exfoliate it without sonication. For TBA, the exfoliation mechanism is based on the increased interlayer distance and weakened interactions between layers due to the diffusion of TBA. Although the GO flake sizes reach 18 µm and 35 µm for these two cases, the scalability and reaction time for these two methods limit the mass production of GO.

Finally, the use of expanded graphite is also an effective way to obtain large GO flakes. The advantage of this method is the increased distance between the interlayers of expanded graphite. Thus, the oxidising agents are easy to diffuse into the graphite and further promote the oxidation of graphite. Hence, fewer oxidising agents are needed to obtain fully oxidised GO. The oxidising cutting can be controlled in this case. Meanwhile, since the graphite is fully oxidised, further mechanical exfoliation can be avoided as well due to the strong hydrophilicity of the obtained GO[43]. However, the yield and time-consuming size-fractionation are still issues in producing expanded graphite. In general, thermally expanded graphite maintains these challenges, as it rapidly releases gas during the preparation process, while chemically expanded graphite has a chance to suppress these issues due to its gentle expansion process[44].

In all, although there are various methods to synthesise GO with flake sizes up to hundreds of micrometres, the use of large graphite has been selected in this project for its simplicity. The obtained GO flake size is large enough to be used in the printhead as well.

2.2 Reduction of GO

Reduction type	Method	C/O ratio	Conductivity (S/m)	Ref.
Chemical	Hydrazine 100 °C 24 hrs	10.3	2400	45
	Hydrazine & ammonia solution 95 °C 15 mins	12.5	9960	46
	Ascorbic acid 23 °C 24 hrs	N/A	800	47
	Vitamin C & ammonia solution 95 °C 15 mins	12.5	7700	46
	HI & acetic acid 40 °C 24 hrs	15.27	7.85×10^3	48
Thermal	Rapid heating by a pre-heated furnace 1050 °C in argon 30 s	10	2300	49
	2200 °C in argon 30 mins	N/A	1.57×10^5	50
	2700 °C in argon 1 hr	> 1000	5.77×10^5	51
Microwave	700 W 1 min	2.75	274	52

Table 2 Comparison of three major types of GO reduction methods. The C/O ratio and conductivity of rGO are used as indexes to compare the reduction degrees of GO from these methods.

Mass production of graphene is paramount for its commercialisation. The reduction of GO into rGO is one of the most popular options. Reduction strategies vary; the most common ones are chemical reduction, thermal reduction, and microwave reduction[53]. Table 2 summarises the various reduction methods for GO. The C/O ratios and conductivity of obtained films have been used as proxies for the comparison of reduction degree.

2.2.1 Chemical reduction of GO

In terms of the chemical reduction of GO, several typical reducing agents are introduced in this section, including hydrazine (N_2H_4)[54], hydroiodic acid (HI)[55], and L-ascorbic acid (L-AA)[46]. These reducing agents can reduce GO either in liquid or vapour forms under moderate conditions, which makes the process simple and scalable. Once the oxygen-containing groups of GO have been removed during reduction, the hydrophobicity of the material is increased. Then, the rGO flakes tend to aggregate, and the brown GO dispersion becomes black precipitates. This can also be used as a measure of GO reduction.

Hydrazine is a strong reductant often used to reduce GO. It is usually added directly into the GO dispersion to achieve the reduction process. Ruoff et al. added the hydrazine directly into the GO dispersion at 100 °C for 24 hours and obtained the rGO film with a conductivity of 2400 S/m[45]. The conductivity of rGO film could be further increased to 9960 S/m by additionally using ammonia solution[46], which improves the stability of rGO dispersion after the use of hydrazine. In addition, the conductivity of obtained rGO film could be increased by adding more hydrazine into the GO dispersion. However, it was found that excessive hydrazine results in the agglomeration of rGO dispersion, which should be avoided[56]. Although strong reducing agents like hydrazine are often used to obtain a higher reduction degree of GO, it is a highly toxic chemical, so the reduction process needs to be well controlled to ensure safety. Therefore, the application of a green reductant like L-AA has been reported to avoid safety issues. The reduction degree of GO in the methods based on L-AA is not comparable to methods using strong reducing agents. However, these methods make the reduction process user-friendly and green to the environment. Initially, L-AA was simply mixed with the GO dispersion at room temperature[47]. The conductivity of obtained rGO film was 800 S/m. Since then, an improved method has been developed to further increase the conductivity of rGO film to 7700 S/m, which is similar to the ones reduced by hydrazine. In this method, the addition of ammonia solution and the application of 95 °C temperatures during the reduction process have effectively helped the reduction of GO[46]. In the meantime, the improved stability of dispersion indicates that the final conductivity of rGO is not only decided by its reduction degree but also affected by the interconnections among the rGO flakes in the final thin film.

Apart from hydrazine and L-AA, hydroiodic acid (HI) is also worthy of noting. It is also a strong reducing agent used for GO reduction. The conductivity of obtained rGO paper reduced by HI can be one magnitude higher than that of hydrazine[48]. Apart from this, the obtained film also exhibits better mechanical properties than the film reduced by hydrazine, likely due to the densification of the obtained film. However, HI is still a strong and unstable acid, which could easily form iodine vapour. Hence, safety is still a critical challenge for the application of HI.

2.2.2 Thermal reduction of GO

In thermal reduction, GO is generally heated at high temperatures under a vacuum with an inert or reducing atmosphere to remove oxygen-containing groups and defects[57]. The degree of reduction of GO is mainly dependent on the applied temperature. The critical temperatures for thermal reduction and exfoliation are reported to be between 127 °C and 2400 °C[58].

Figure 5 presents key temperatures that correspond to different reduction degrees of GO. The initial thermal exfoliation of GO starts at 127 °C when the stacked GO layers have been exfoliated by the sudden release of gases due to the decomposition of oxygen-containing groups. Then, the sp^3 carbons are converted into sp^2 carbons at 600 °C. When the temperature rises to 1000 °C, the hydroxyl group content drops, and only < 2% of oxygen is left in the structure. Finally, when the temperature reaches 2400 °C, the restoration of the sp^2 structure

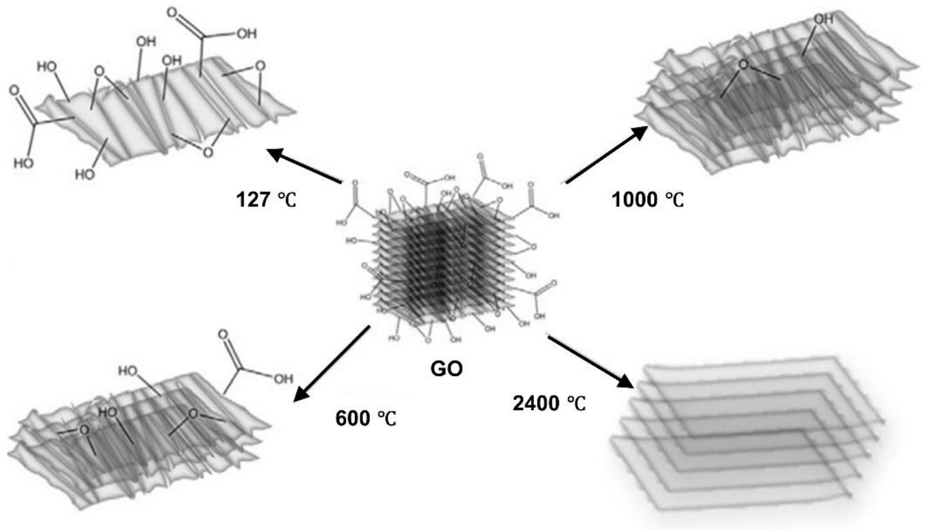

Figure 5 Key temperatures during GO thermal reduction and GO structures at each point, which start from 127 °C, where structures are left with many oxygen groups, to 2400 °C, where structures are close to pristine graphene. Oxygen-containing groups have been removed by thermal reduction, and the buckling behaviours in the GO structure are due to the carbon atoms lost during the reduction. Such behaviour is supressed by the re-graphitisation of graphene at high temperatures (2400 °C)[58].

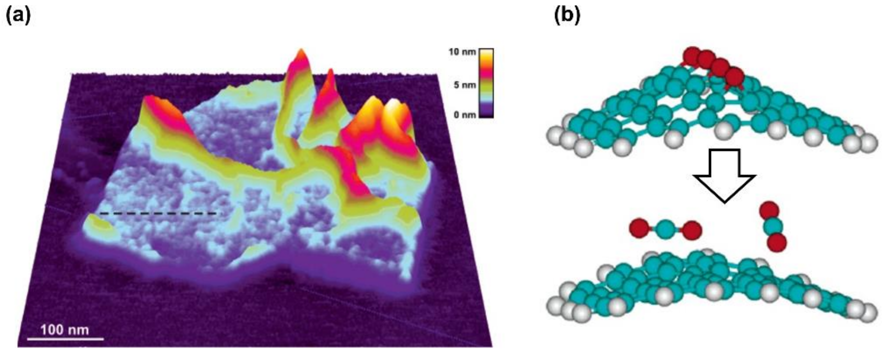

Figure 6 (a) Illustration of a thermally reduced GO flake with typical wrinkled structure; (b) atomistic model of gas generation during the thermal reduction of GO; such loss of carbon atoms during the release of gases leave GO flakes with a wrinkled structure[49].

increases dramatically, and the re-graphitisation starts. An AFM scan of wrinkled rGO and an atomistic model of gas generation during GO thermal reduction is illustrated in figure 6[49]. The CO/CO_2 gases are generated due to the decomposition of oxygen-containing groups under high temperatures. Hence, carbon atoms are lost in the basal plane of GO during this process, which results in the formation of topographical defects. This also explains why the buckling behaviours in figure 5 happen in thermally reduced GO. The buckling behaviours continue until 2000 °C, at which point the oxygen-containing groups have been almost fully removed, and the re-graphitisation starts. Consequently, the graphite-like structure can be seen again. As table 2 demonstrates, the electrical conductivities of thermally reduced GO vary from 2300 to 5.77×10^5 S/m[49,50,51]. All these methods have used temperatures up to 1000 °C, but the electrical conductivities of rGO films are quite different. The preparation of GO into free-standing graphene paper is considered an effective way to further improve the electrical conductivity due to the improved interconnections among the flakes. Although thermal reduction could reduce the GO effectively, it is still a time- and energy-consuming technique. In addition, when the temperature is too high, most flexible substrates like polymeric materials, paper, and fibre are not available. Therefore, the application of thermal reduction is restrained in many situations.

2.2.3 Microwave reduction of GO

Microwave reduction has a similar mechanism to thermal reduction. The graphene structure is an efficient microwave absorber, as it contains abundant delocalised π electrons[59]. Therefore, when the microwave is applied to GO, the sp^2 domains are effectively heated by the microwave. Thus, a thermal reduction can be conducted in sp^3 domains next to these sp^2 domains, and the reported electrical conductivity of rGO prepared using this method reaches 274 S/m[52]. Although the value is not as high as the rGO formed by the thermal reduction method, the reduction time of this method is about 1 minute. Hence, microwave reduction is a rapid way to prepare reduced GO, and it simultaneously exfoliates the graphene due to the vigorous gas-releasing process. However, the vigorous process brings similar limitations as thermal reduction.

Overall, the L-AA method has been chosen as the reduction method for this project. Since the final application of the project is to print FTEs, the targeted substrates will be mainly polymeric substrates. Thus, the high-temperature annealing of thermal reduction is not feasible. For the same reason, microwave reduction is also not suggested. Accordingly, chemical reduction is a more practical approach. As highly oxidised GO usually contains carbonyl and ether groups, which are difficult to remove by chemical-reducing agents[60], the electrical conductivities of chemically reduced GO may not be comparable to that of thermally reduced GO. Nevertheless, the ‘green’ nature of L-AA makes it an ideal option for this project.

2.3 Preparation of graphene-based dispersions and inks

2.3.1 Preparation of graphene-based dispersions

Graphene-based dispersions are used in a wide variety of applications, ranging from composites[8] to wearable electronics[12] and more. Two main challenges must be overcome to obtain high-quality graphene-based dispersions, namely van der Waals forces between graphene layers and the hydrophobic nature of graphene. The preparation of graphene-based dispersions can be generally divided into two steps:

(1) exfoliation of graphene from the precursor;
(2) formation of a stable graphene-based dispersion.

In the first step, the graphene flakes should be exfoliated from the bulk materials, and the interactions between graphene layers should be disrupted. This usually

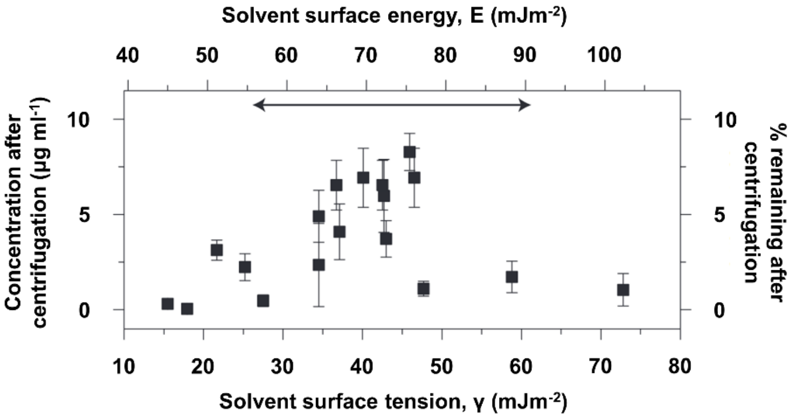

Figure 7 Surface energies or surface tensions that are favourable for graphene production via the pure-solvents method[61]. Solvents that have surface energy within 70 – 80 mJ/m^2 or surface tension within 40–50 mN/m are useful for the exfoliation of graphite.

requires external energy to be exerted on the bulk materials. As mentioned in the previous section, GO requires much less energy, as its interlayer distance has been expanded following oxidation[34]. Nonetheless, the exfoliation of graphite still requires vigorous processing, as the van der Waals forces between graphene layers are strong[17]. The most typical method used for the exfoliation of graphite is sonication. Sonication has advantages in production scale, yield, condition simplicity, and low cost. These benefits make sonication a popular choice for graphene production for both lab and industry scales[17]. To maximise the exfoliation effect, a similar surface energy difference between solvents and graphite is preferred. Hernandez et al. investigated the relationship between solvents with various surface energy and their corresponding graphite concentration after sonication and estimated an optimal surface energy range for many solvents[61]. Solvents that have surface energy within 70 – 80 mJ/m^2 or surface tension within 40 – 50 mN/m are considered favourable for exfoliating graphite, as shown in figure 7. In addition, the mechanism of sonication-assisted graphene exfoliation is depicted in figure 8[17]. The liquid cavitation initiates bubbles in the solvent. When a large number of the bubbles around the graphite collapse, micro jets and shock waves are generated and impact the graphite. These numerous impacts exert intensive compressive stress on graphite and result in strong normal tensile stress, which is reflected from the free interface of graphite.

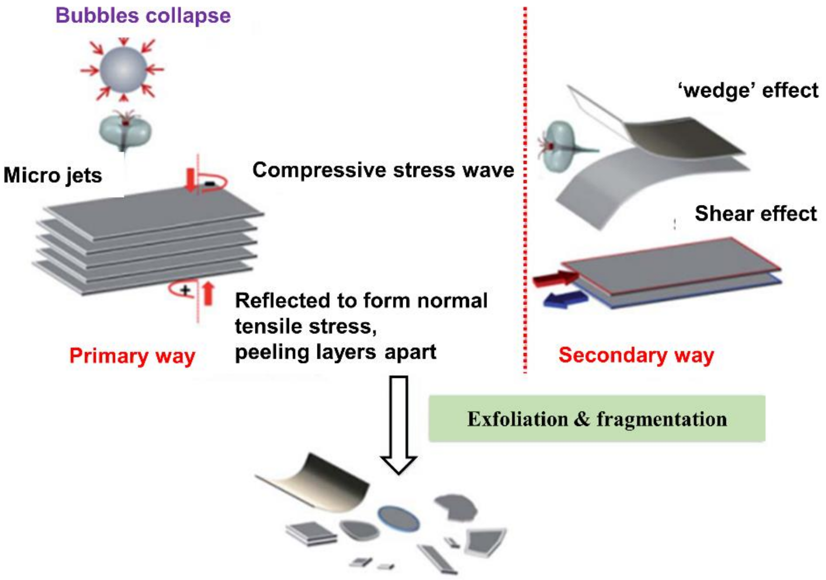

Figure 8 Mechanism of sonication on graphene exfoliation. The primary method of exfoliation features collapsing bubbles that apply micro jets to compress the graphite, and the reflected forces start to 'peel' the graphene off the graphite. Wedge and shear effects also contribute to graphene exfoliation as well[17].

As such, the peeling of graphite starts. Furthermore, shear stress in the lateral direction, caused by unbalanced compressive stress and the micro jets wedging effect, also influences the exfoliation process. Since sonication is such a harsh method for the exfoliation of graphene, the damage and oxidisation of the graphene sheet are inevitable[62].

Once the graphene flakes have been exfoliated from the bulk materials, the formation of stable graphene-based dispersion starts. GO is a material with strong hydrophilicity. Simultaneously, its carboxyl groups provide electrostatic repulsion in water for its stabilisation. Therefore, water is an ideal solvent for the preparation of highly concentrated GO dispersions[63]. However, the situation is different for hydrophobic materials like rGO and GNPs. Their flakes easily re-aggregate in water. In general, there are two strategies to fix this issue[64,65]:

(1) adding stabilisers between the graphene and solvent;

(2) matching the surface energies of graphene and the solvent.

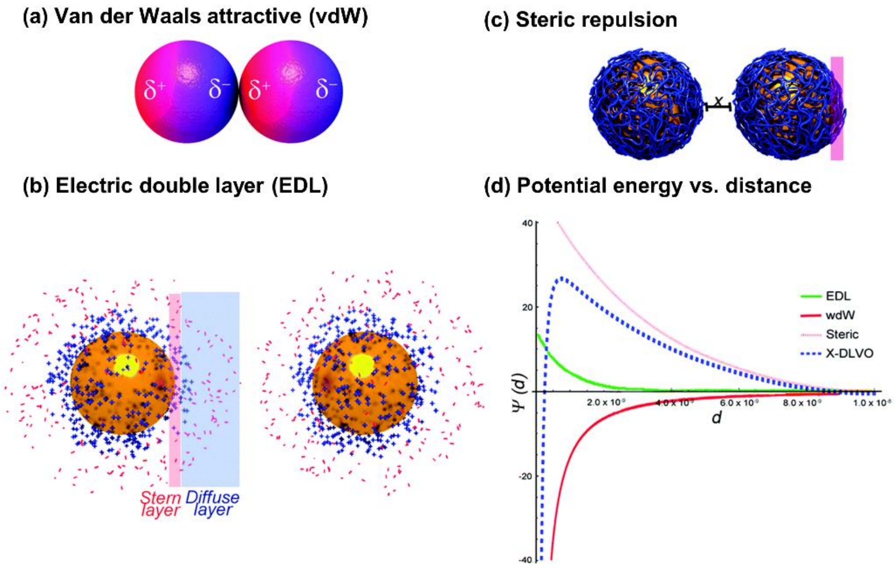

Figure 9 Three main interactions in colloidal: (a) van der Waals forces, which are the aggregation of nanoparticles at the most basic level; (b) steric repulsion, which is provided by the macromolecules attached to the nanoparticles; (c) EDL, which is formed due to the surface charge of nanoparticles; and (d) the curve of potential energy vs. distance, which indicates different contributions of various stabilisation mechanisms as a function of a particle distance[66].

Figure 9 (a)–(c) show different types of particle interactions in the dispersion, and (d) presents a plot of energy–distance that reports when the aggregation of particles happens in solvent[66]. The graphene flakes are easy to aggerate in the solvent due to the strong van der Waals forces among the flakes. Two types of repulsive interactions are usually used during the preparation of stable graphene dispersions, namely electrostatic and steric repulsion. Steric repulsion is attributed to the macromolecules attached to the graphene surface. These macromolecules form a protective layer of graphene and keep the graphene spatially separated from each other[67]. In electrostatic repulsion, electrostatic double-layer (EDL)-induced Coulomb repulsion is the key to preventing aggregation. Figure 10 (a) illustrates EDL formation and zeta potential definitions for a negatively charged graphene surface[68]. The double layers refer to the stern and diffuse layers, where one is the layer bound to the surface with oppositely charged ions, and the other is a loose layer with attracted ions. The diffuse layer consists of free ions, and the movements of these ions are influenced by both electrical attraction and thermal motion. The potential of a slipping plane, as depicted in figure 10 (a), is defined as zeta potential; the ions below this plane and graphene together are considered one kinetic unit. A general range of sufficient stabilisation has been shown in

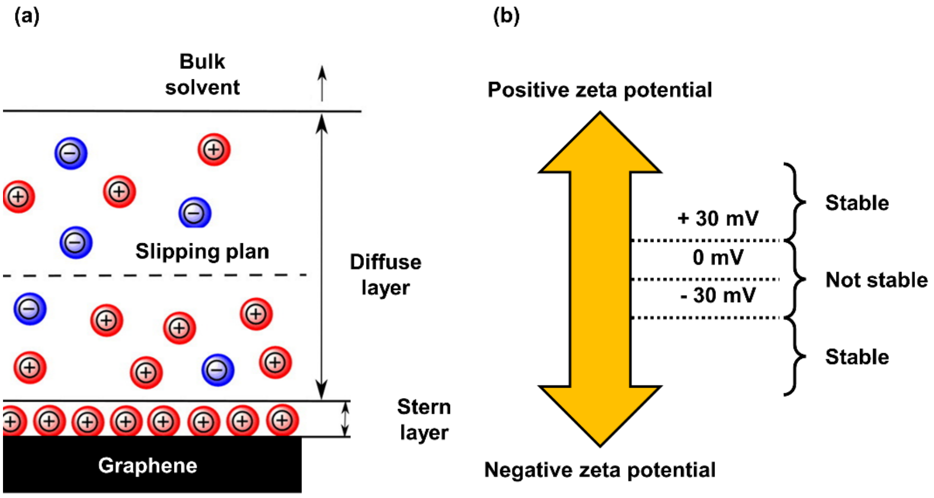

Figure 10 (a) Illustration of EDL on a negatively charged graphene surface; the potential between the slipping plane and the graphene surface is defined as zeta potential[68]; (b) the suggested relationship between Zeta potential and a stabilised solvent, values between -30 and +30 mV indicate the formulation of an unstable solvent[69].

figure 10 (b), which indicates zeta potentials larger than 30 mV or smaller than -30 mV provide a better stabilisation effect on graphene[69]. The first strategy to avoid the aggregation of graphene by either electrostatic or steric means uses stabilisers. Numerous factors influence the choice of stabilisers, and the selection is also largely dependent on the final application. Therefore, some popular stabilisers have been introduced below, including pyrene derivatives, polymers, and surfactants (ionic and non-ionic). A comparison of graphene to stabiliser ratios is shown in figure 11[64]. It reports that pyrene derivatives result in the highest graphene to stabiliser ratio compared to other stabilisers due to their graphene-like structure. In other words, the amount needed for the pyrene stabiliser to support the same loading of graphene dispersion is the least compared to other types of stabilisers. Pyrene derivatives are one type of polyaromatic hydrocarbons (PAHs), which have similar sp^2 domains to graphene. π–π stacking is the key interaction between pyrene derivatives and graphene[70]. These pyrene derivatives are mostly used for the stabilisation of graphene and rGO, which have large extended sp^2 domains in their structures. In addition, most pyrene derivatives used in graphene dispersions are small molecules[64,71], which also have high graphene to stabiliser ratios. Additionally, the electronegativity of pyrene derivatives has an influence on the strength of the π–π interaction. Sulfonyls, which can be used to strengthen the π–π interaction, demonstrate the best

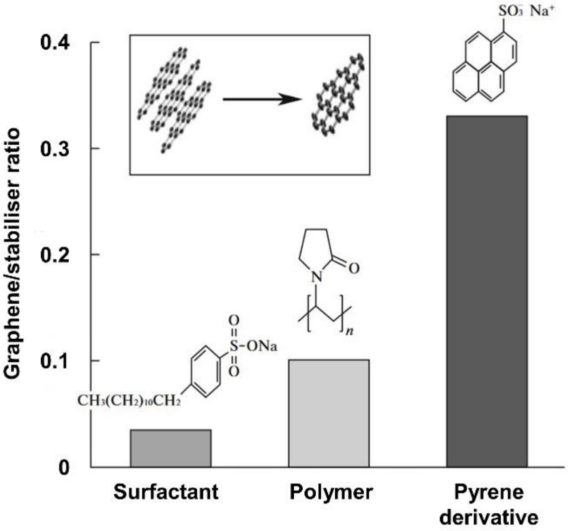

Figure 11 A graphene to stabiliser ratio comparison of various types of stabilisers. The pyrene derivatives have the highest graphene to stabiliser ratio compared to surfactants and polymers[64].

dispersibility of graphene in aqueous solvents compared to other functional groups like amines[64]. Furthermore, a designed analogue of sodium pyrene-1-sulfonate (PSA) has been reported, which increased graphene concentration around two times in water compared to that of other pyrene-stabilised graphene[72]. A design concept of a new pyrene stabiliser for graphene dispersion has been proposed and is illustrated in figure 12. The figure shows that the addition of an alkyl spacer (n-butyl chain in the reference) between the aromatic core and sulfonate group can improve the parallel and binding strength between the pyrene and graphene surfaces. The interaction between polar sulfonate residues and water is also improved due to the conformational freedom from the spacer. Overall, the structure changes of this analogue show a potential way to design a new graphene stabiliser with a larger graphene to stabiliser ratio. In addition, another bis-pyrene stabiliser has been reported, which could dramatically improve the exfoliation efficiency and stabilisation of graphene. The bi-pyrene binding groups in the stabiliser could also strengthen the π–π interaction between graphene and the stabiliser and provide a high exfoliation efficiency and an improved stabilisation of graphene[73]. Thus, the stabiliser based on pyrene derivatives shows great potential in the preparation of highly concentrated graphene dispersion with a small amount of stabiliser. However, the conductivity of this type of stabiliser is limited and usually results in an increase of resistance of rGO/stabiliser compound[74]. In addition, the strong interactions between stabilisers and graphene make the removal of these molecules a challenge[75]. In terms of polymer stabilisers, conductive polymers like polyvinylpyrrolidone (PVP)[76], poly(3,4-ethylene dioxythiophene):poly(styrene sulfonate) (PEDOT:PSS)[77], and polyvinyl alcohol (PVA)[78] can all stabilise and improve the electrical conductivity of graphene-based dispersions. These polymers interact with graphene via π–π interactions or van der Waals forces and maintain stable graphene-based dispersions either sterically or electrostatically. Thus, conducting composite inks can be formulated based on these dispersions[79]. Non-conductive polymers like ethyl cellulose (EC) are another popular option for graphene-based dispersions/inks. The presence of EC sterically hinders the aggregation of graphene by changing the ink into an emulsion system. Like conductive polymers, printing stability is improved once EC has been used as a stabiliser. Additionally, the viscosity of formulated ink can also be tuned using EC. The use of EC brings advantages like long-term stability (up to 9 months) and a ‘green’ printing process[80].

However, the use of polymers as stabilisers for graphene-based inks also has limitations. Polymers have strong interactions with the graphene, which make the stabiliser hard to fully removed[75]. A high temperature is generally needed in the annealing process and results in a limited range of available substrates. Concurrently, polymers like PEDOT:PSS and PVA are sensitive to moisture. Although the inks formulated based on these stabilisers have good conductivity at the beginning, the long-term stability of the printed patterns is limited[81,82].

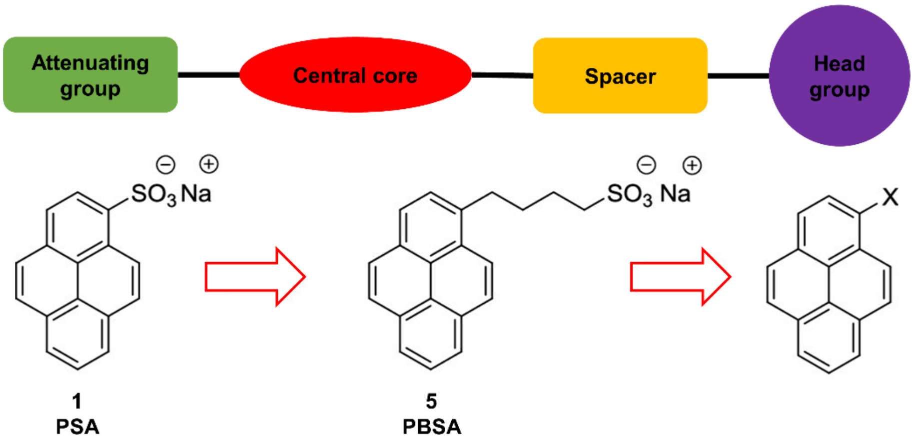

Figure 12 The design concept of a novel pyrene stabiliser; the addition of a spacer exhibits the potential to obtain a higher graphene to stabiliser ratio, as it can improve the parallel and binding strength between the pyrene and graphene surfaces[72].

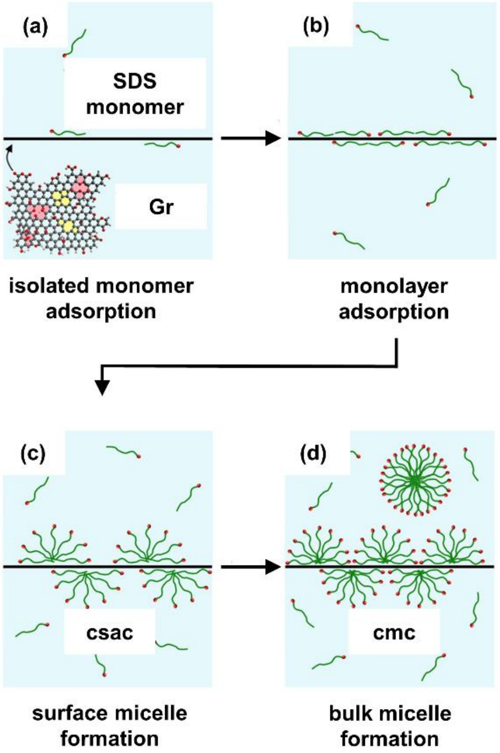

Figure 13 Illustration of how SDS monomers are absorbed onto a graphene surface; (a) & (b) the formation of the SDS layer on the graphene surface; (c) & (d) the formation of a micelle on the graphene surface (critical surface aggregation concentration [csac]) and in the solvent bulk (critical micelle concentration [cmc])[83].

Surfactants are another significant family of stabilisers; they can be divided into ionic and non-ionic surfactants. Sodium dodecyl sulfate (SDS) is a typical ionic surfactant for graphene dispersion. Figure 13 illustrates step by step how SDS monomers are absorbed onto the graphene surface [83]. Hsieh et al. stressed that the best dispersion stability could be achieved by increasing SDS loading up to ~40 μM. The other common type of surfactant is the non-ionic surfactant. A schematic of a general non-ionic surfactant structure and its interactions with a graphene surface is shown in figure 14[84]. Generally, the use of surfactants improves the hydrophilicity of the graphene surface. Then, the interfacial energy between graphene and solvent is reduced, and the graphene can be dispersed in the water like GO does with the assistance of applied external energy. Attached surfactant molecules also hinder the re-aggregation of the exfoliated graphene flakes. Smith and his colleagues have concluded the working mechanisms of different types of surfactants used to generate graphene-based inks[85]. They believed that the electrostatic repulsion dominates the stabilisation of graphene in the ionic surfactants stabilised inks, while graphene stabilisation relies more on the steric stabilisation in non-ionic surfactants.

Overall, the stabilisers mentioned above can all prevent the re-aggregation of graphene (GNPs or rGO) and form stable dispersions. Pyrene derivatives yield better stabiliser to graphene ratios compared to other types of stabilisers. Since most stabilisers are hard to remove and most have an insulating nature (except conductive polymers), the stabiliser residuals strongly limit the electrical conductivity of the final deposited patterns[75]. Therefore, using a stabiliser with a better stabiliser to graphene ratio is a route to improve the electrical conductivity of the final deposited patterns. However, the stabiliser used in this project is a team-made perylene derivative, which is a PAH designed based on the concept of adding a spacer between the centre core and head group. The aim of using this stabiliser is to capitalise on its high stabiliser to graphene ratio to form a stable graphene dispersion with better electrical conductivity.

The second strategy to form stable graphene-based dispersions using either electrostatic or steric means can be performed when the surface energies between the graphene and solvent match. Thus, no stabilisers are needed to form a stable dispersion in this strategy. Regarding GNPs and rGO, popular options for preparing pure solvent, graphene-based dispersions contain N-methyl pyrrolidone (NMP), dimethyl sulfoxide (DMSO), and dimethylformamide (DMF), among others[61,86,87].

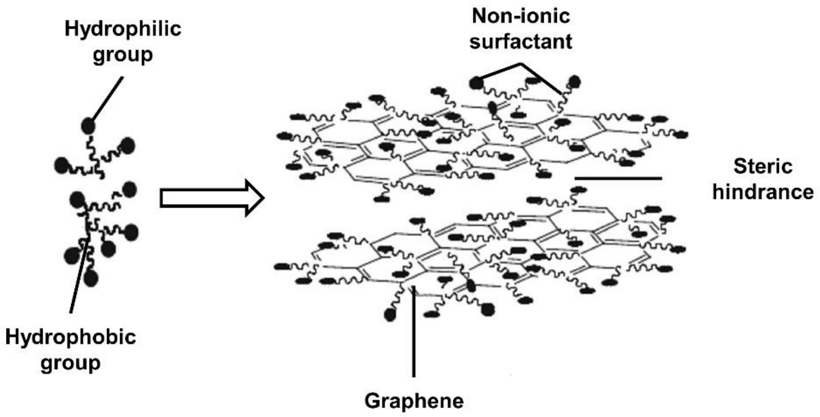

Figure 14 The typical structure of non-ionic surfactant and their interactions with a graphene surface; the hydrophilic groups face the bulk solvent, and the hydrophobic groups attach to the graphene surface. Steric repulsion is the main repulsion interaction provided by the non-ionic surfactant is the steric repulsion[84].

It is believed that interfacial energy between the above solvents and graphene plays an important role in both the exfoliation and dispersion processes. An inequality that represents the surface energy relationship between solvent and pristine graphene for stabilisation is presented below[65]:

Equation 1

$$S_{g/s} = \gamma_g - \gamma_s - \gamma_{gs} > 0$$

where $S_{g/s}$ is the spreading coefficient, γ_g is the surface energy of graphene, γ_s is the surface energy of the solvent, and γ_{gs} is the interfacial energy between graphene and solvent.

When $S_{g/s}$ is positive, the spontaneous wetting of graphene by the selected solvent occurs. Consequently, the interaction between graphene and the solvent molecule overcomes the interactions between the graphene sheets. The exfoliation of graphene can be achieved in this case. As the wetting happens, the used solvents generally have a stronger affinity to the surface of graphene and can provide higher exfoliation efficiency and better stabilisation at the same time. Once the graphene flakes have been exfoliated from the bulk materials, the next step is to prevent aggregation. For the stabilisation of pure solvent graphene-based dispersions, a molecular dynamics simulation reveals that steric hindrance is the key to preventing graphene sheet aggregation[88]. The interactions between graphene sheets and solvent molecules must be stronger than that between solvent molecules. Hence, the solvent molecules prefer to attach to graphene sheets and prevent graphene aggregation. By selecting a suitable solvent like NMP and combining it with a centrifugation technique, a dispersion with graphene loading up to 60 mg/ml with long-term stability could be achieved[89]. However, the range of solvents that have suitable graphene/solvent interfacial energy is limited, and most of these solvents are either toxic or have high boiling points. Thus, safety and the annealing process remain challenges in this case.

The covalent modification of graphene has been reported as another route to improve its dispersibility in various solvents. The grafting of radicals on graphene is a common method used in this area. The reactive species are used to modify graphene surface energy, so the solubility of graphene can be altered via these adducts. The typical reactive intermediates used are radicals, nitrenes, and aryne, among others, and they can be grafted onto graphene surfaces via various methods such as free radical addition, cycloaddition reactions, and CH insertion[90]. However, the functionalisation of graphene degrades the properties of graphene, especially the electrical properties, as the integrity of its sp^2 structure has been changed. Furthermore, the modification methods mentioned above all require sophisticated processes, which limit their mass production and applications.

In all, the major challenge of preparing graphene dispersion based on a pure solvent is matching the surface energies of graphene and solvent. This could be done either by selecting suitable solvents or modifying the graphene. However, the most suitable solvents are highly toxic, and the covalent modification of graphene generally degrades its properties. Thus, the preparation of graphene dispersion based on pure solvent is not suggested in this project.

2.3.2 Preparation of graphene-based inks

In general, the main challenges to formulating graphene-based inks are divided into two parts:

(1) the preparation of a stable dispersion;
(2) the optimisation of the ink's printability.

The details of the first challenge have been introduced in the previous section. As for the second challenge, the printability of formulated inks can generally be adjusted using modifiers. However, the printability of this research requires more than that. Since the aim of this project is to print large rGO flakes, the printing of large graphene flakes is also a critical challenge. Similarly, the ideal range of the ink's rheological properties required by the DMP-2831 printer is hard to reach, as DI is the major solvent, and the aimed application is printed FTEs. While the modifiers could make the ink's rheological properties fit the printer's requirements, the electrical properties of the printed FTEs are sacrificed when too much non-conductive modifier is used. Thus, the modification of ink printability using waveform is another commonly used method for inkjet printing of inks with non-ideal rheological properties[91]. In this technique, less modifier can be used to formulate the printable ink, which benefits the electrical conductivity of the final printed patterns.

During the modification of rheological properties, additives are used to modify the surface tension and viscosity of the ink so that these values can fall into the suitable range of the selected printer. The inkjet printer used in this project is the

DMP-2831 from Fujifilm. It has several suggested fluid properties for formulated inks, including the following[92]:

(1) Surface tension: 28 – 42 mN/m at printing temperature;
(2) Viscosity: 10 – 12 mPa.s at printing temperature;
(3) Density: Specific gravity > 1.

There are two types of surfactants commonly used for modulating the surface tension of formulated ink, which are ionic and non-ionic surfactants. Numerous examples have been reported on the use of these surfactants during the preparation of graphene-based inks, such as SC, SDS, SDBC, Triton X-100, and Tween, among others[13]. Notably, most can be used as both surfactants and stabilisers to make graphene-based inks. In terms of the modulation of viscosity, polymers are commonly used. The most reported polymers are EC, PVP, PVP, PVA, and PEDOT:PSS, among others[13]. Polymers also serve as both thickeners and stabilisers to graphene-based inks. However, the removal of these polymers for the final printed patterns is a challenge.

All these reported additives can tune the rheological properties of formulated inks into a suitable range for the selected printer. However, a critical prerequisite must be fulfilled during the selection of these additives, which is that the stabilisation of the ink should not be disturbed by the added additives. Since the stabilisation mechanism used in this project is electrostatic repulsion provided by a team-made perylene stabiliser, non-ionic surfactants are preferred in this project. Triton X-100 has been used as the surfactant in a water-based GNP ink and did not disturb the electrostatic stabilisation provided by a pyrene stabiliser, which is suitable for this project[74]. As for the selection of thickener, EG has been selected, as it can increase the viscosity of formulated inks, and its residuals can be removed under relatively mild annealing conditions[18,74]. Thus, the electrical conductivity of printed FTEs is further improved. It is worth noting that these two additives are not the only options for the ink modifiers; any other option that does not interrupt the stabilisation of the inks and improves the final properties of printed FTEs would be favourable in this project.

In addition, the mechanism of printing large graphene flakes must be explained. The benefit of using large graphene flakes has been mentioned in previous sections. The large flake size is an effective way to improve the conductivity of the final deposited graphene patterns due to its improved interconnections among the flakes[32]. As for inkjet printing, modifiers are usually required to modulate the printability of formulated ink, but most of these additives are not conductive[69]. Therefore, the use of large graphene flakes is a promising option to improve the conductivity of final printed patterns. However, the main challenge for this method is the upper limit of the particle size able to be used in the printhead. In general, the particle size used in inkjet printing should not be larger than 1/50 of the diameter of the nozzle[36]. Otherwise, nozzle clogging is unavoidable. However, this guideline was revised in 2017, as Pei et al. had successfully printed GO flakes with an average size larger than the radius of the nozzle diameter[18]. The paper indicated that GO could be aligned under a high shear rate and can distribute in order along the flow in the pipe/nozzle during printing. Simultaneously, the capillary force could also maintain the jetted droplet without breaking, even when loaded with ultra-large GO flakes. The prerequisite to achieving this successful printing is the formation of laminar flow during printing. Thus, as long as the laminar flow has been formed, large GO flakes can be aligned in the flow and have the opportunity to be expelled from the nozzle without clogging. Thus, ultra-large GO flakes could be jetted out from the used printhead in the project. However, it is worthy to note that the maximum average flake size printable in this project is about the radius of the nozzle. In addition, since the laminar flow improves the alignment of large flakes in the nozzle, a small Reynolds number is preferred, as it could help the formation of laminar flow in the pipeline[93]. Thus, a higher viscosity of ink might be needed during the ink formulation. However, DI water has been selected as the major solvent for both Pei's project and this work. Thus, the addition of thickener would help the printing of large flakes. It is also worth noting that although water has a low viscosity of ~1 mPa.s, the Reynolds numbers of inks formulated in Pei's project were all < 2000, so their flows could be considered laminar flows[93].

Overall, this project provides a theory for printing large rGO flakes from the reported literature that used the same type of printhead. With a similar 2D material combined with the same printhead, ultra-large rGO may be printed successfully, improving the electrical properties of printed FTEs.

2.4 Inks and FTEs based on GO and rGO

2.4.1 Simple comparison of GO and rGO

GO and rGO are the most commonly used graphene derivatives. They are produced to capitalise on the superior properties of graphene while expanding its application. Since the properties of GO and rGO are strongly dependent on their oxidation degree[94], there are no standard properties. Generally, these two materials are used in the form of flakes. Therefore, the flake size plays an important role in the properties of their final applications[32]. Thus, a simple comparison of GO and rGO is presented in this section to evaluate how the properties change with their oxidation degrees and sizes. Since the final application of this project is FTEs, the electrical conductivity, optical transparency, and mechanical flexibility of the flakes are the main concerns. The ratio of sp^2 domains to sp^3 domains in the structure of GO and rGO contributes to the conductivity. The sp^2 domains form conductive paths for carriers, while the sp^3 domains are more like the transport barriers for carriers[95]. GO has an insulating nature due to the high proportion of sp^3 domains in its structure. As the reduction degree of GO increases, so too does its electrical conductivity. The transportation of electrons in the reduced GO can be altered from tunnelling and hopping to conduction when the sp^2 ratio is larger than 60%.

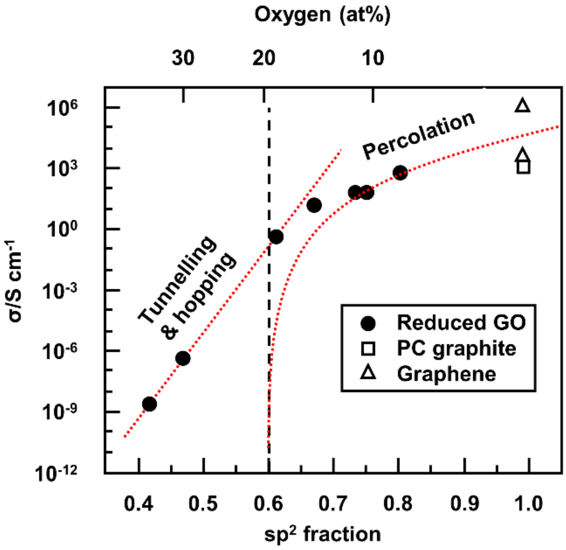

Figure 15 The electrical conductivity of thermally reduced GO as a function of sp^2 proportion in its structure. A 0.6 sp^2 proportion is proposed as the percolation threshold for GO conductivity. Tunnelling and hopping dominate below this proportion, and percolation dominates after this value[96].

Figure 15 shows the proportion of sp^2 domains in the rGO structure, which has been used as an indicator of the electrical conductivity of the final reduced GO[96]. However, the final conductivity of the printed FTE is not determined solely by the degree of reduction of GO. Since the electrode consists of numerous deposited flakes, the resistance caused by the junctions among the flakes also plays a vital role in the final properties of printed FTEs. As mentioned in previous sections, the large flake size is an efficient way to reduce this resistance. Fewer junctions emerge when large flakes are used, as fewer flakes are needed to form the conduction path for the electrons[32].

In terms of mechanical properties, the oxidation of graphene can significantly change the hybrid state of the carbon atoms, which leads to many changes in its performance. In addition, since the oxygen groups are attached to the basal plane of the graphene, the lattice defects and higher surface roughness are induced during the oxidation process, which degrades the properties of graphene. By using an AFM probe to interact with suspended GO flakes, Rouff et al. measured the Young's modulus of a suspended single-layer, double-layer, and triple-layer graphene oxide and found them to be 156.5 ± 23.4 GPa, 223.9 ± 17.7 GPa, and 229.5 ± 27.0 GPa, respectively[97]. The strong interlayer bonding of graphene oxide has been reported to effectively avoid interlayer sliding, so the Young's modulus of few-layer graphene oxide is not very different from each other.

As for the oxidation degree, various molecular dynamics and molecular mechanics simulations have been conducted to investigate the effect of oxidation degree on GO’s mechanical properties. Zheng et al. showed that the Young's modulus of graphene oxide decreases linearly with increased functionalisation levels, and a decrease of 33% in the Young’s modulus could be reached at a 15% degree of functionalisation. An increase in the proportion of sp^3 hybrid bonds is believed to destroy the original π bond of graphene and results in a depreciation of the mechanical properties[98]. A similar result has been reported by Khoei et al.; both the modulus and tensile strength are reduced with an increase in the oxidation degree of GO. However, it was found that induced oxygen groups have more influence on GO’s tensile strength than on its modulus. The induced oxygen groups increase the C–C bond length and reduce the tensile strength severely[99]. Finally, another simulation has shown that the oxidation degree would affect not only the mechanical properties of GO but also the structure arrangement. Ordered GO has higher mechanical properties compared to those of amorphous GO with the same level of oxidation[100]. In all, oxidation severely degrades the mechanical properties of graphene due to the increased disorder of its structure. There is a negative correlation between the oxidation degree of GO and its mechanical properties. Thus, the use of rGO is an effective way to restore the desired mechanical properties of graphene.

Regarding the effect of flake size, it has been reported that using large flakes is a promising way to improve the mechanical properties of rGO-based films and aerogels. The stronger interactions between adjacent rGO flakes can effectively prevent the slipping effect during the deformation process. Thus, the occurrence of cracks can be reduced[101], so a similar effect could also happen for printed FTEs.

In terms of the optical transparency of GO and rGO, the aim of using these two materials is to match the superior optical transparency of pristine graphene (~97.7%)[6]. Many transparent electrodes based on rGO have been reported, and the optical transparency of these electrodes ranges from 65% to 90%[102]. Electrodes with high thickness result in better electrical conductivity but limited optical transparency. Thus, using large rGO flakes would not only improve the electrical conductivity of the final electrodes but also modify the optical transparency, as fewer flakes are needed to achieve the same level of electrical conductivity. It is well known that graphene has a broadband absorption of light from UV to IR due to its unique conjugated π system in the structure[103]. Although Gr only has 2.3% light absorption in visible light, its absorption reaches 40% in the IR and microwave range[104]. Therefore, its derivatives GO and rGO have been widely used as optical transparent absorbers to take advantage of this property of graphene. Xie et al. mixed GO with PVA to prepare an optical transparent hybrid film for shielding UV light[105]. The film maintained up to 40% transmittance of visible light and absorbed over 97% of UV light at 300 nm. It is believed that the ratio of the conjugated π system plays a vital role in absorption[106]. The effect of reduction degree on GO’s ability to absorb light has also been investigated. Marta et al. mixed rGO with PVA to investigate the effect of reduction degree on light absorption. The same amount of rGO with different reduction degrees was mixed with the same volume of PVA in their project. The transmission spectra from UV to mid-infrared of prepared films have been measured. A negative correlation exists between the transmittance of rGO to the reduction degree in all spectra. The higher reduction degree of rGO would bring stronger absorption of the light from UV to IR, which confirmed the effect conjugated π system. The stronger reduction brings rGO close to pristine graphene, so a similar light absorption ability and range can be found in rGO[107].

In conclusion, rGO is a promising alternative to pristine graphene. The reduction degree determines whether its properties are more like graphene or GO. Therefore, applications based on rGO can take advantage of GO and pristine graphene at the same time, making it an ideal functional material for this project.

2.4.2 Inks and FTEs based on GO and rGO

GO and rGO are the most relevant materials in this project. There are two strategies to prepare inkjet-printed FTEs based on GO and rGO. One use GO-based inks to print the electrodes and reduces them to restore the properties of graphene; the other uses rGO-based ink to print the FTEs directly**.** Water is the most used solvent for both GO- and rGO-based inks, not only because it is a ‘green’ solvent but also because it is easy to remove after the deposition. In the meantime, water is an ideal solvent to prepare the GO-based inks, as no stabiliser is needed in this case[63]. Table 3 summarises the different inkjet-printed FTEs based on different GO and rGO inks with water as their main solvent.

In terms of printed FTEs based on GO, Huang et al. used GO with different layers to prepare functional inks[21]. The various GO samples were directly dispersed into water to form stable inks. The viscosities were modified by modulating the GO loadings, and the average flake size did not exceed 400 nm for all inks. The electrodes were printed on flexible substrates like poly(ethylene terephthalate) (PET), polyimide (PI), and others. Thermal reduction was used to restore the conductivity of printed GO electrodes. Temperatures reaching 400 °C combined with a mixture of argon and hydrogen gases (95:5) were used to assist the reduction of GO. However, a conductivity of only 500 S/m was obtained from the electrodes printed on PI. The flexibility of the printed electrode was tested by measuring the resistance differences before and after hundreds of bending cycles. There were no obvious changes in resistance after the bending test, which proved sufficient flexibility of the printed electrodes.

Material	Solvent/ Stabiliser	Reduction / Annealing	Flake size	Sheet resistance/ Conductivity	Optical transparency	ΔR	Ref.
GO	Water	400 °C with H_2 5%, argon 95%	< 400 nm	500 S/m	-	~1	21
	Water	200 °C	530 nm	12 M Ω/□	76%	~1	108
	Water	80 °C HBr	-	150 K Ω/□	84%	-	109
	Water	Hydrazine fumes at 100 °C	0.54 - 2.2 um	8.8 × 103 to 1.6 × 104 S/m	-	-	110
	Water	HI Vapour, 95 °C, 30min	35.9 µm	2.48 × 10^4 S/m	-	-	18
rGO	Water/ Triton X-100	Ascorbic acid 80 °C	-	1500 S/m (pressed pellet)	-	-	111
	Water/ PVA	Hydrazine 80 °C + 350 °C	-	1000 S/m	83%	-	112
	Water/PVP	500 °C	~608 nm	359.88 S/m	-	-	113

Table 3 A summary of inkjet-printed FTEs from GO and rGO water-based inks. The reduction conditions, graphene flake size, electrical conductivity, and optical transparency of printed FTEs are presented.

In 2012, Kong et al. prepared inkjet-printed GO-based FTEs using IR lamps as the reduction method[108]. The lamp was placed 3 cm away from printed patterns, and the temperature was maintained at ~200 °C to reduce the GO in the ambient. The GO ink was also prepared by dispersing GO directly into water, and the average flake size was controlled in this project as well. Electrodes with optimum electrical and optical properties measured 12 MΩ/□ at a transparency of 76%. The bending test was also used in this project to measure the flexibility. Although there was some hysteresis, the resistance remained unchanged before and after the test.

In addition to the use of thermal reduction to restore the electrical conductivity of GO, chemical reduction is also important. A method of using diluted HBr acid to reduce the printed GO electrodes at 80 °C was reported by Rogala and his co-authors[109]. Propylene glycol (PEG) was used as a thickener to prepare the GO ink. PEG was chosen since it could be removed effectively by thermal annealing at a relatively low temperature (120 °C). Thus, this expanded the range of available flexible substrates. In the meantime, the printed electrodes exhibited a sheet resistance of 150 KΩ/□ with a transparency of 84%. The diluted strong acid proved to be an effective way to restore the electrical conductivity of GO and caused no damage to the polymeric substrate like PET.

The effect of GO's size on inkjet-printed FTEs was explored by Kim and his co-authors in 2016[110]. The GO suspension was directly applied as the printable ink in this project. Hydrazine fumes were used to reduce the printed GO-based FTEs at 100 ℃. The electrical conductivity of the printed FTEs was improved from 8.8×10^3 to 1.6×10^4 S/m when the flake size changed from 0.5 to 2.2 µm. The increased flake size effectively improved the conductivity of printed patterns due to the reduced sheet-to-sheet junctions.

In 2017, Pei reported a GO ink that loaded with ultra-large flakes[18]. The maximum average flake size reached 35.9 µm, which is larger than the radius of the nozzle used. The ink used ethylene glycol (EG) as the thickener. They found that a conductivity of 2.48×10^4 S/m could be measured with an annealing temperature below 100 °C and that the larger flake size results in smaller inter-flake contact resistance. Thus, an improved electrical conductivity was obtained in this study. However, a reduction process is still needed for the printed pattern due to the insulting nature of GO. Although the annealing temperature has been brought below 100 °C, the use of hydroiodic acid (HI) still limits the use of other substrates. However, this method once again validated the advantage of formulating graphene-based inks with large flake sizes.

Regarding printed electrodes based on rGO, Dua et al. prepared an rGO water-based ink to print electrodes for vapour sensors in 2010[111]. L-AA and Triton were used as the reductant and stabiliser during the preparation of the ink. GO was mixed with L-AA and reduced at 80 ℃. Then, the rGO ink was prepared by mixing the black precipitates with Triton directly under sonication. In this project, measurements for the electrical, optical, or mechanical properties of the electrodes were not taken. The only conductivity data were collected from the pressed pellet of rGO right after the reduction step. Since a large amount of Triton was used in this project, it is reasonable to assume that the conductivity of the final printed electrode is not ideal for many electrical applications. Nonetheless, this is a typical example of preparing rGO-based ink and FTEs. Briefly, the GO is first reduced to restore the properties of graphene. Then, the stabiliser is needed for the preparation of stable graphene dispersion. While the additives for adjusting fluid properties are not mentioned in this project, they are an important factor as well. As mentioned in previous sections, the chemical reduction of GO is not complete; there are still oxygen-containing groups remaining in rGO[60]. Thus, the electrical conductivity is limited in this way. The use of a stabiliser could further degrade the electrical properties of rGO-based inks and printed FTEs. Therefore, the main challenge of rGO-based inks and FTEs is the electrical conductivity.

Apart from using a surfactant to prepare the inkjet printable rGO-based inks, some inks based on water-soluble polymers have been reported as well. Lim and his co-authors reported an inkjet printable rGO/PVA ink in 2012[112]. The GO dispersion was first mixed with PVA. Then, hydrazine was used to reduce the GO/PVA mixture at 80 °C to prepare the rGO ink. The PVA was used as both the stabiliser and thickener for the ink. The best electrical conductivity and optical transparency they reported were 1000 S/m and 83%, respectively. However, this conductivity was achieved by an additional thermal reduction after the printing process. Thus, the conductivity of the initially printed FTEs was still low. Notably, the main solvent used in this project was a mixture of DMF and water, which could also be a reason for such limited conductivity, as DMF has a high boiling temperature.

In 2021, a commercial rGO water-based ink was used to print graphene lines with high conductivity[113]. It is an aqueous ink that contains a mixture of rGO flakes and PVP. Lian et al. characterised the rGO flakes (~608 nm average flake diameter) and sonicated the ink before the inkjet printing process. The highest electrical conductivity of the final electrodes was around 359.88 S/m. High-temperature annealing was also applied in this project to remove the PVP residuals from the printed patterns. In other words, the electrical conductivity of the initial FTEs is still low.

As table 3 shows, the preparation of GO-based ink is much simpler than that of rGO-based ink. The stabiliser is not necessary for GO-based ink when water is the main solvent. On the other hand, the use of stabilisers is inevitable for rGO-based ink, as the rGO is a hydrophobic material. However, the major difference between these two types of inks is the reduction process. The reduction occurs after the deposition of GO-based FTEs, while it usually happens during the preparation of rGO-based ink. This difference makes a huge impact on the inkjet printing of FTEs.

As for GO-based FTEs, the reduction temperature is limited due to the substrate used since the most flexible and transparent substrates are polymeric substrates. This also explains why the FTEs reduced by thermal reduction have lower electrical conductivity. Therefore, chemical reduction with strong reductants and the use of large GO flakes have been applied to further improve the properties of GO-based FTEs. However, the use of strong reductants jeopardises the safety of the procedure, as many of them are toxic chemicals.

In terms of rGO-based FTEs, the harsh post-treatments can theoretically be avoided, as the reduction usually happens during the ink formulation. This could broaden the available range of polymeric substrates. However, as table 3 concludes, not many rGO-based FTEs have yet been reported. The main challenge for rGO-based FTEs is currently their limited electrical conductivities. Although GO has been reduced during the ink formulation, the addition of stabilisers could strongly degrade the electrical conductivity of printed FTEs. Thus, improvements to the electrical conductivity are the priority of rGO-based FTEs. To fix this issue, another advantage of rGO must be exploited. Since GO is the precursor of rGO, the preparation of rGO-based inks loaded with large flakes is also possible. Thus, the improved interconnections in the printed FTEs could be achieved in this case. In the meantime, the effect of stabilisers on the electrical conductivity also needs to be considered. As mentioned in previous sections, the selection of a stabiliser like a perylene derivative, which has a high stabiliser to graphene ratio, is a promising option for the printed FTEs since less additive is used in this case. Thus, by combining the advantages of large rGO flakes and stabilisers with a high stabiliser to graphene ratio, there is a new possibility for preparing rGO-based inks and FTEs; this is the novelty of this project.

2.5 Inkjet printing technique

2.5.1 Inkjet printing techniques

Inkjet printing is a widely used technique in graphics printing and publishing industries[114]. In recent years, the technology has been used beyond the traditional industries and has become a versatile tool in the functional materials deposition area, especially in the electronic industry[115]. Inkjet printing has advantages in time, materials, and energy consumption compared to conventional electronic fabrication techniques, like vapour deposition and photolithographic etching[116]. The whole process of inkjet printing of entire functional materials can be defined by the following steps: (1) formulation of applicable inks; (2) generation of droplets; (3) deposition and interaction of droplets on substrates; and (4) solidification of deposited droplets on substrates. Therefore, the challenges of inkjet printing result from the above steps.

There are two types of mechanisms of droplet generation in inkjet printing: (1) continuous inkjet (CIJ) and (2) drop-on-demand (DOD) inkjet[114]. The schematic diagrams of CIJ printing systems are presented in figure 16 (a). In terms of CIJ printing, a continuous ink flow is ejected from the nozzle under pressure. Then, the flow breaks into droplets due to Rayleigh instability. The droplets are charged by a charging device at the nozzle so that they can be deposited with control after passing through a charged deflector. Since the droplets are continuously generated due to the Rayleigh instability, unwanted droplets can be recycled to the gutter via an electrical field applied by deflectors. As the recycled droplets have been exposed to the environment, the ink in the gutter may not be reused in order to maintain the ink quality. The above CIJ printing is also called binary printing since the droplets are either deposited or recycled. Regarding DOD printing, the droplets are only ejected when they are needed. This is the biggest difference between these two techniques. The droplets are generated by propagating a pulse in the chamber. The pulse suddenly changes the cavity volume in the chamber and causes high pressure in this small space. Consequently, a droplet is ejected from the nozzle due to the high pressure. DOD printing can be divided into thermal DOD and piezoelectric DOD printing, which is depicted in figure 16 (b). In thermal DOD printing, a thin film heater in the chamber heats the ink to its boiling point when a current is applied. A bubble is generated and expanded after the heating. The bubble collapses when the heater temperature is reduced after the removal of the current.

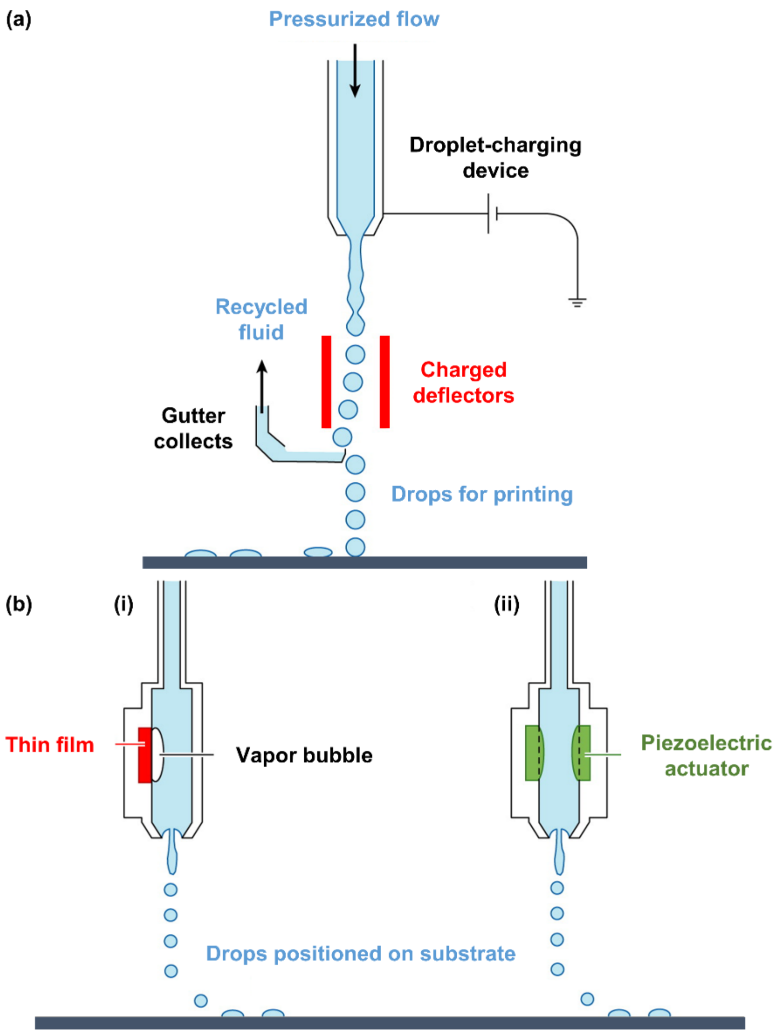

Figure 16 The schematic diagrams of (a) CIJ and (b) DOD printing systems; DOD printing can be further divided into (i) thermal DOD and (ii) piezoelectric DOD printing[114]. The droplets are continuously jetted out from the CIJ system and can be selected for by the charged deflectors; by contrast, they are jetted out on demand in the DOD system.

This expansion and collapse of the bubble generate a strong pulse in the chamber and eject a droplet from the nozzle. In terms of piezoelectric DOD printing, the change of cavity volume is actuated by a piezoelectric transducer in the chamber. The piezoelectric transducer applies direct pressure to the ink and ejects droplets from the nozzle.

Based on different actuation mechanisms, piezoelectric DOD printing can have different modes, which are squeeze, bend, push, and shear modes (Figure 17 (a) – (d), respectively)[117]. Figure 17 (a) shows the ejection mechanism of squeeze mode;

Ink first fills the chamber, which is surrounded by the piezo-ceramic tube. Then, a pulse signal is applied to the tube and causes a rapid contraction of the tube.

Therefore, a sudden decrease of volume in the chamber causes the ejection of a droplet from the nozzle. The bend and push modes have similar printhead structures. The droplet is ejected from the nozzle via either the bending of a piezo-ceramic plate (Figure 17 (b)) or the expanding of a piezo-ceramic rod (Figure 17 (c)). The last mode depicted in figure 17 (d) is the shear mode. The voltage pulse effects on the piezo-ceramic causes first the upper part of the channel to deform, followed by the lower part. Then, a chevron shape is formed in the channel to eject a droplet from the nozzle.

CIJ printing has advantages in its printing frequency and lack of nozzle clogging, but its recycling system for unwanted droplets introduces a risk of contamination. Therefore, this technique is not widely used in the printing of functional materials. As for DOD printing, thermal DOD printing shows advantages in printhead cost but has a limited available ink range due to its high-temperature process during printing. However, piezoelectric DOD printing shows more advantages compared to the other two techniques. Its printheads have a longer lifetime, and it is not limited by temperature. Thus, combining the above advantages with digital controllability makes piezoelectric DOD printing a promising technique for the printing of functional materials.

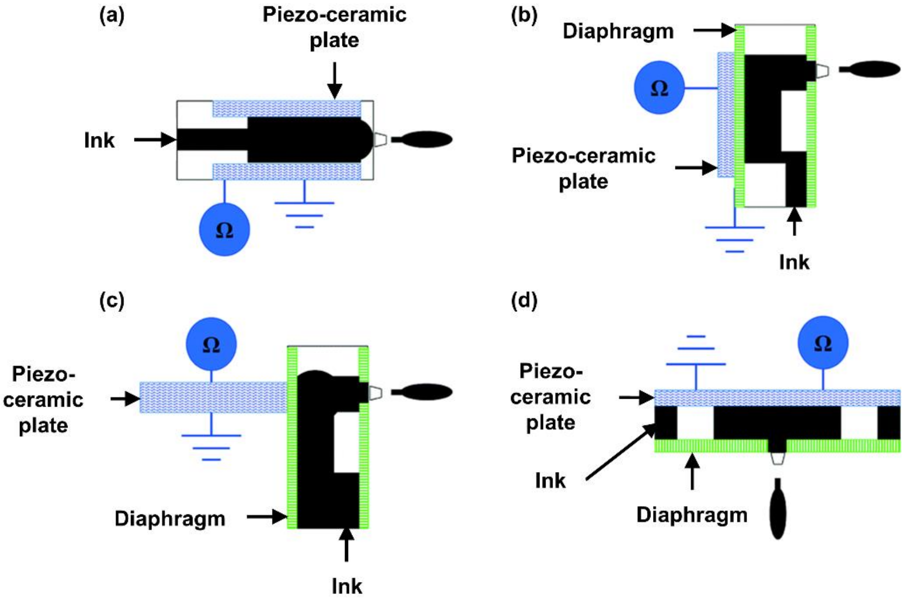

Figure 17 Working modes of a piezoelectric DOD printer head in (a) squeeze mode; (b) bend mode; (c) push mode; and (d) shear mode[117]. The droplets are jetted out from the chamber by the deformation of the piezoelectric elements, and the DMP-2831 printer uses shear mode in its printhead.

2.5.2 Formulation criteria for inkjet printable inks

The droplet formation sequence on a DOD printer is pictured in figure 18[118]. Ink is firstly ejected from the nozzle in the form of a liquid column. Then, it deforms into a leading drop attached to a long tail. Finally, the tail either retracts into a leading drop or breaks into satellites during flight. The formulation of printable ink is complex, especially for inks loaded with functional materials that require specific properties due to their applications. Although all components have an effect on the final ink, several key factors impacting formulation are primarily considered. First is the ink stability, which is the lifetime of ink against the sedimentation. Second is inks' rheological properties, which include surface tension, viscosity, and density[119]. Third is the optimisation between ink's printability and its performance. This section focuses on inks' rheology properties.

In the DOD printing system, both surface tension and viscosity determine the formation of droplets and their spreading on the substrate. Generally, DOD printing prefers Newtonian ink with low viscosity and high surface tension[120]. The low viscosity ensures enough time for ink to refill the chamber, and high surface tension is used to hold ink in the nozzle and prevent dripping. However, surface tension cannot be too high, as it would prevent droplet break-off from the nozzle[121].

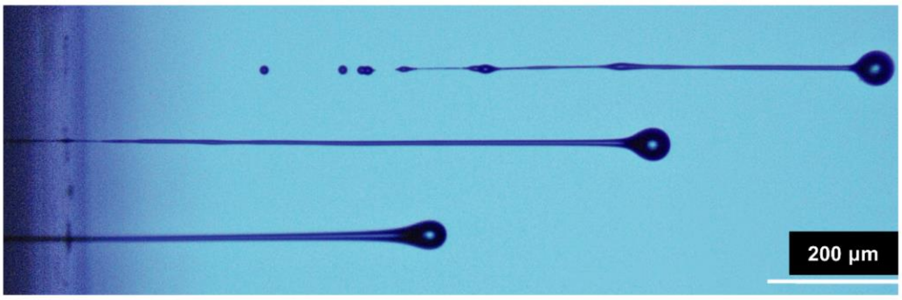

Figure 18 The stages of droplet formation in DOD printing, observed via high-speed photograph. From bottom to top is the formation of the liquid column, formation of the leading drop attached to a long tail, and formation of the droplet with retracted tail or satellites, respectively[118].

Several dimensionless parameters can be used to describe the jetting behaviour of droplets and define the printable regime of the formulated ink, including Reynolds number (Re), Weber number (We), and Ohnesorge (Oh) number/Z number (Z)[114]. The equations (2 – 4) define the above numbers.

Equation 2

$$Re = \frac{\nu\rho a}{\eta}$$

where ν, ρ, and α are droplet velocity, ink density, and nozzle diameter, and η is dynamic viscosity. The Re number indicates the ratio of the inertial forces to the viscous force of a flow moving in a pipeline at a certain velocity. The flow is given a velocity at the beginning, and the inertial force of the flow originates from this momentum. The viscous force originates from the frictional shear force between fluid layers of the flow and is the force that resists the moving flow[93]. Thus, higher viscosity could result in a laminar flow. This is because the strong frictional shear force dampens the turbulence and random motions of the flow caused by the inertial force. Thus, turbulence occurs when the viscosity of the flow is too small; turbulence is believed to develop when Re > 2000[93].

Equation 3

$$\mathrm{We} = \frac{\nu^2 \rho \mathrm{a}}{\gamma}$$

where γ is the ink surface tension, and the We number is the ratio of the inertial force and the surface tension force of a droplet moving in a medium at a certain velocity. The droplet becomes spherical due to its own surface tension. Higher surface tension gives a stronger resistance to the inertial force. Thus, the droplet could keep its spherical shape and not break up into satellites. In general, the droplet maintains its shape when the We number is smaller than 10[122].

Equation 4

$$\mathrm{Z} = \frac{1}{\mathrm{Oh}} = \frac{\mathrm{Re}}{\sqrt{\mathrm{We}}} = \frac{(\gamma\rho \mathrm{a})^{1/2}}{\eta}$$

where Z is the inverse of the Oh number. The Oh number was first proposed by Wolfgang von Ohnesorge[123] and was developed to guide the boundaries of a printable regime of inkjet printable inks, as the Re and We numbers are not accurate enough. Ohnesorge investigated the relationship between the viscosity, inertia, and surface tension of different inks and explored the jetting behaviours of inks at different Re, We, and other dimensionless numbers[123]. He proposed a new dimensionless number and defined it as the ratio of the square root of the We number to the Re number. This number is denoted as the Ohnesorge number. It is the simplest dimensionless number he found to describe the boundaries of a printable regime of inkjet printable inks. It describes the importance of the viscous force as to the inertia force and surface tension of the ink. Thus, a larger Oh number means the viscous force dominates, so higher energy is needed to jet the ink from the nozzle. On the other hand, smaller Oh numbers mean a longer ink column will be jetted out from the nozzle with the same amount of energy. In this case, the satellites may become an issue for the ink[123]. However, its inverse, the Z number, is more commonly used in practice. A widely accepted range of Z number ($1 < Z < 10$) was proposed by Derby and his co-authors[124]. Ink with a Z number out of this ideal range may be too viscous to jet or could confront the satellites issue during printing.

However, numerous different ranges have been reported on different types of printheads[119,125,91]. Thus, it indicates that the Z number range for printable ink is not only decided by the ink's rheological properties but also relies on the printhead used in the project.

Apart from the Z number, there are two more factors that must be considered for stable droplet ejection. One is the minimum energy for overcoming the ink/air surface tension barrier, which can be indicated by droplet velocity (v). Equation 5 shows the minimum velocity required for droplet ejection[126]:

Equation 5

$$\mathrm{v_{min}} = \sqrt{\frac{4\gamma}{\rho a}}$$

where γ is ink surface tension, ρ and α are ink density and nozzle diameter, respectively. Furthermore, a minimum We number for droplet ejection can be predicted by the following equation[114]:

Equation 6

$$\mathrm{We} = \mathrm{v_{min}}^2 \frac{\rho a}{\gamma} > 4$$

where γ is ink surface tension, ρ and α are ink density and nozzle diameter, respectively. The other factor is related to the impact of the droplet on the substrate. In order to avoid droplet splashing, equation 7 predicts the maximum velocity:

Equation 7

$$We^{1/2}Re^{1/4} > f(R)$$

where f(R) is a function of surface roughness; further research reported that the f(R) for flat and smooth substrates is about 50.

Combining the proposed Z number range by Reis and Derby and these two factors together, a map indicating suitable fluid properties for DOD printable inks is determined in figure 19[114].

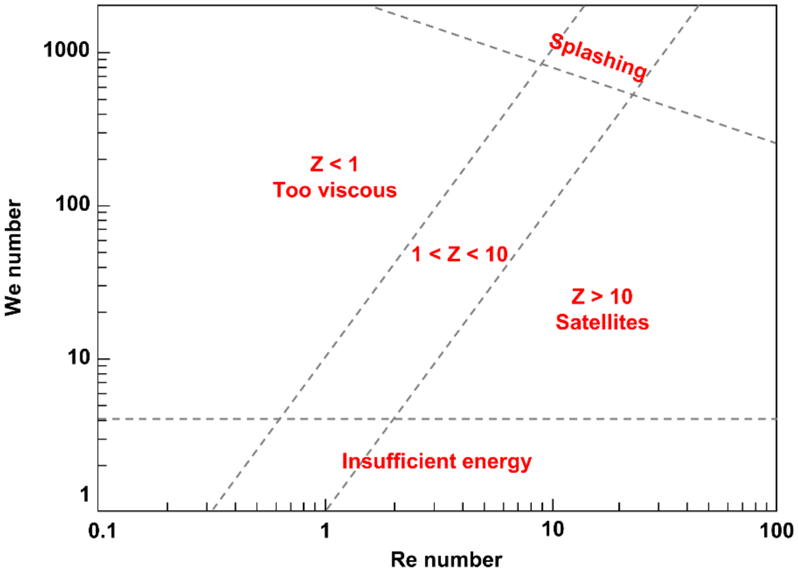

Figure 19 A map for predicting suitable fluid properties for the formulation of DOD printable inks. The droplets are too viscous to print when the Z number is smaller than 1, and satellites form when the Z number is larger than 10[114].

2.5.3 Droplet impact, spreading, coalescence, and solidification on substrates

After the ejection of droplets from the nozzle, the droplets impact and spread on the substrate. Then, they interact with other droplets and form a designed pattern after solidification.

The energy for droplet impact and dispersal on the substrate originates from kinetic and gravitational energy after ejection. Since droplets in DOD printing generally have a small volume (1 – 100 pl) and low density, the effect of gravitational energy is negligible[114]. Therefore, the inertial and capillary forces dominate the impact and dispersal process. Figure 20 illustrates the droplet interaction process with substrate[114]. The droplet first contacts the substrate with a duration < 1 μs and starts an inertial force and viscous force dominated impact-driven spreading process. Then, the remaining energy keeps the droplet spreading on the substrate for a relatively long time (0.1 – 1 ms); capillary force is the dominating force at this point[127]. The droplet either reaches an equilibrium (single droplet) or starts interacting with other droplets (droplets coalescence) after the impact and spreading process.

For single droplet spreading equilibrium, equation 8 defines the droplet spreading degree on the substrate; the droplet volume is considered constant before impact, and the final equilibrium spread drop is assumed to leave a footprint on the substrate[128]:

Equation 8

$$\beta_{eqm} = \frac{d_{eqm}}{d_0} = \sqrt[3]{\frac{8}{\tan\frac{\theta}{2}\left(3 + \tan^2\frac{\theta}{2}\right)}}$$

where β_{eqm} is the ratio between equilibrium spread droplet diameter (d_{eqm}) and droplet diameter during flight (d_0). θ denotes the contact angle of the equilibrium spread droplet. Thus, the size of a printed droplet can be manipulated by altering the equilibrium spread droplet diameter and contact angle.

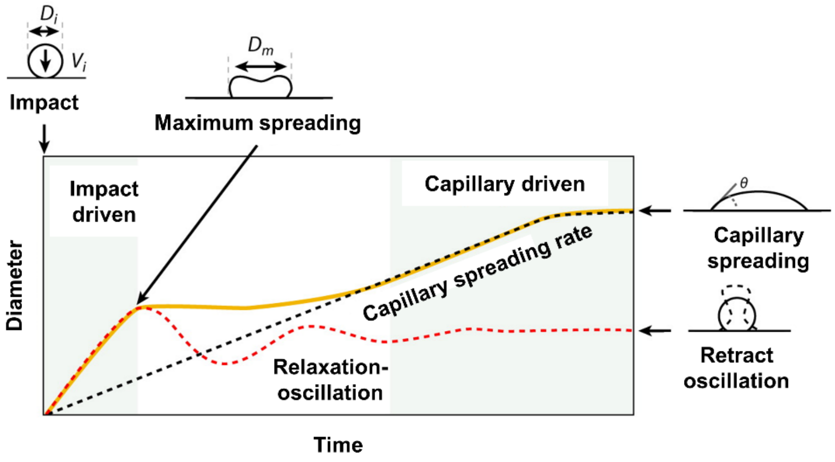

Figure 20 Schematic illustration of the droplet interaction process with the substrate, from impacting to equilibrium; the diameter and time are used as axis[114]. The droplet first experiences an inertial force and viscous force dominated impact-driven spreading process, and the capillary force dominates for the rest of the droplet spreading on the substarte[127].

In the case of functional ink printing, the droplets need to form continuous lines. Therefore, adequate control of coalescence between overlapped droplets is important. The droplets coalescence can be controlled by manipulating the drop spacing. Figure 21 shows different behaviours of droplets coalescence from (a) individual droplets to (c) smooth lines and (d) bulging by decreasing the drop spacing[129]. Figure 21 (e) shows a ‘stacked coins’ phenomenon due to the fast evaporation of ink between two adjacently printed droplets.

The solidification of droplets is an important process in obtaining uniform patterns. The wetting status of a droplet on the substrate need to be addressed before progressing to the pattern drying process. The wetting status of a droplet changes from spreading to non-wetting with increasing contact angle on the substrate, which is shown in figure 22[130]. The solidification process consists of two simultaneous steps, which are solvent evaporation and solute transporting in the droplet.

In terms of solvent evaporation, three modes have been determined, which are the constant contact diameter (CCD) mode, the constant contact angle (CCA) mode, and a mix of the two[131]. In the CCD mode, the droplet diameter remains consistent while the droplet volume and contact angle decrease during evaporation. The CCA mode is one where the droplet has no pinned contact line, and both the volume and diameter of the droplet decrease during evaporation, while the contact angle is consistent during the whole process. The mixed mode means both the contact angle and diameter decrease during droplet drying.

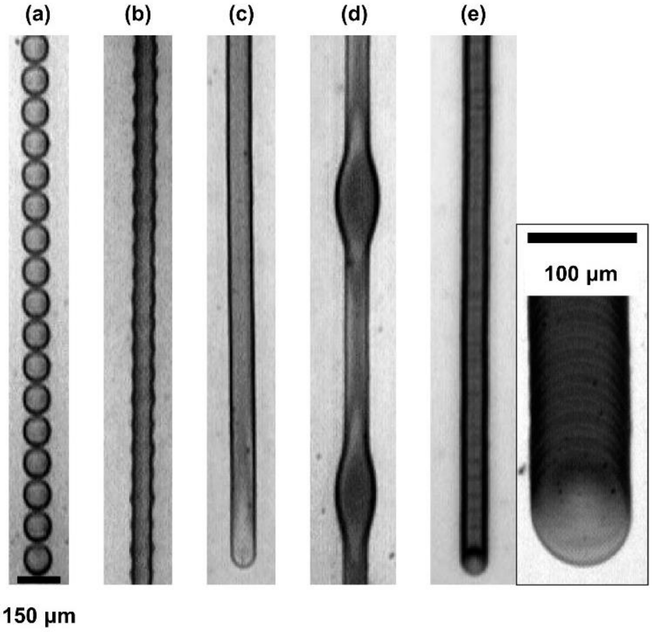

Figure 21 Droplet's coalescence behaviours with decreases in drop spacing. The printed patterns change from (a) individual drops to (c) smooth lines and further become (d) lines with bulges. A special case, (e) 'stacked coins' (with a magnified image next to it), occurs when the fast evaporation of ink between two adjacently printed droplets happened[129].

As for the solute transportation of droplets, a schematic of different solute transport mechanisms during the drying of a sessile droplet is shown in figure 23[131]. The droplet evaporation, evaporation flux, and capillary flow are the outward flows. The previous two create an inward solute diffusion, while the latter one is the main reason for the coffee-ring effect. Deegan found that the solvent dries faster in the contact line area due to the formation of a thin layer of liquid/vapour interface, and the evaporation rate from this contact line area to the apex of the droplet continuously decreases. Thus, these factors lead to a radial capillary flow, which brings the solvent from the centre to the contact line area to compensate for the loss of solvent in the contact line area. Thus, the solutes have been transported from the centre to the contact line area by this flow and form a ring-like stain after the drying of the droplet[132].

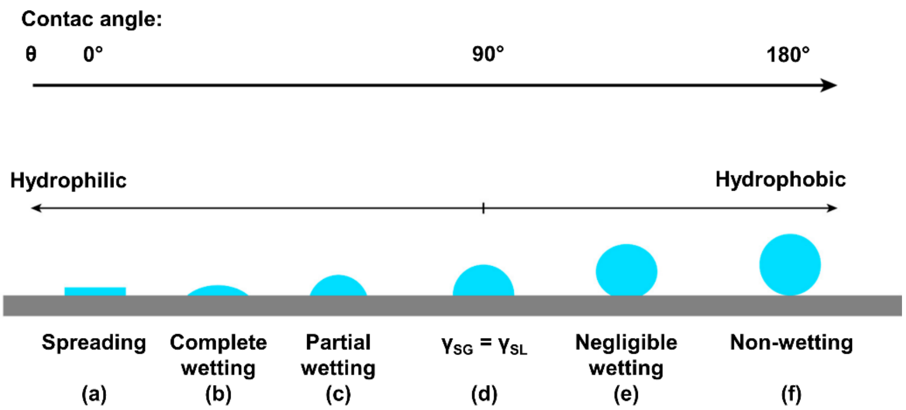

Figure 22 Various droplet drying statuses on a solid substrate, from (a) spreading to (f) non-wetting. The contact angle is smaller than 90° when droplets land on a hydrophilic substrate, and it is larger than 90° when the substrate is hydrophobic[130].

Hence, two criteria must be fulfilled to form a coffee-ring stain; one is a pinned contact line, and the other is edge-dominated evaporation[133]. In order to supress this drying issue, another internal flow named the Marangoni flow is induced during droplet drying[131]. This is an internal flow along the liquid/vapour interface, which travels along the surface tension gradient from the contact line area to the apex of the droplet. The flow is directed from the low surface tension area to the high surface tension area. It can be induced by adding surfactants or co-solvents to the droplet or applying a high temperature on the substrate[134]. The surface tension gradient can be created from the accumulation of surfactants, different evaporation rates of used solvents, or surface tension reduction due to the applied heat. Thus, the Marangoni flow is formed in this case, and the particles in the ring stain are transported back to the droplet centre. As figure 23 shows, a convection flow, which moves the solutes from the edge to the centre, represents the Marangoni flow.

Gravity only needs to be considered when the droplet size is larger than 1 mm. Hence, its effect on DOD-printed droplets is neglectable. Brownian movement only affects solute transportation when the drying time is long enough; otherwise, its effect can be neglected compared to other mechanisms[135].

The suppression of CRE is the key step for obtaining uniform patterns. The ideal methods for suppression are either reducing outward flow or introducing convection flow into the droplet. The reduction of outward flow can be achieved by using solvents with a low evaporation rate[136] or manipulating the environmental humidity[137]. As for convection flow, Marangoni flow can be induced via the control of substrate temperature[138], the formulation of a co-solvents system, or the addition of surfactants[139]. The final step for inkjet printing is annealing of printed patterns. This step is used to improve the properties of printed patterns, especially the electrical properties of printed pattern. The conductivity can be improved by removing solvents and unwanted residuals through annealing. Additionally, the decomposition of polymer-based stabilisers due to high temperatures could further improve conductivity[80]. Finally, the optimised temperature for annealing is strongly dependent on the thermal stability of the substrates and the nature of functional materials.

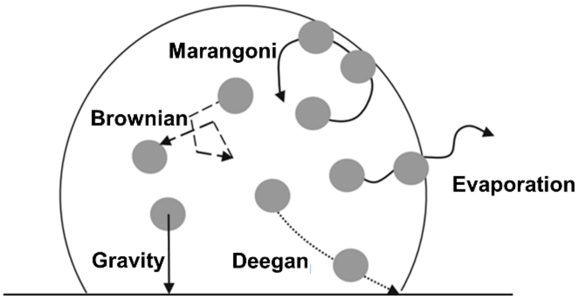

Figure 23 Different solute transportation mechanisms during the evaporation of a sessile droplet; the Deegan flow/capillary flow is the main cause of CRE, and the Marangoni flow is a convective flow which is commonly used as a tool to supress the CRE, as it can transport particles from the contact line back to the droplet centre[131].

Chapter 3. Experimental materials and methods

3.1 Preparation of GO and its dispersion

GO dispersions were prepared via a modified Hummers' method[16]. 1.5 grams of graphite powder (Grade 9842, Graphexel Ltd.) was mixed with 200 ml of concentrated sulfuric acid (95–98%, Sigma-Aldrich) via mechanical stirring, and the ice bath was used to cool the temperature down. Then, a slow process (typically around 30 minutes) of adding 1.5 g of $KMnO_4$ (≥ 99.0%, Sigma-Aldrich) into the above mixture was executed. The addition of $KMnO_4$ was repeated once a day for four days. The mixture was continuously cooled via an ice bath during the addition of $KMnO_4$, and the system was maintained at room temperature during the stirring. After the last addition of $KMnO_4$, the mixture was stirred for an additional 24 hours to obtain a highly viscous graphite oxide. Then, the graphite oxide was gradually dispersed into an ice/water mixture (600 ml), followed by the addition of H_2O_2 (35%, ~6 ml) until the absence of effervescence. After that, the graphite oxide mixture was turned into a light-yellow suspension and stirred for another 2 hours.

The separation of graphite oxide and acid was achieved via centrifuge (Sorvall Legend XTR Centrifuge, Thermo Fisher Scientific) at 8 krpm for 30 mins. Then, graphite oxide precipitate was collected and redispersed into (600 ml) HCl solution (5%). Subsequently, a continuous centrifuge washing process was performed on the above suspension. The suspension was centrifuged at 8 krpm for 30 mins; the precipitation was kept, and DI water was used to replace the supernatant. The process was repeated until the PH of the supernatant became 6. The final graphite oxide precipitate was then dispersed into DI water and centrifuged for another 10 mins at 3 krpm to remove unexfoliated graphite oxide before any further application. The concentration of the initial GO suspension was measured by vacuum drying the initial suspension, and the concentration was ~10 mg/ml.

Regarding the preparation and size control of GO dispersion, the prepared GO suspension was diluted to 3 mg/ml in DI water. Then, the GO dispersions with different average flake sizes were prepared by bath sonication (Elmasonic P 70 H Sonicator) with 100% power at 37 kHz for 12, 18, and 24 hours, respectively. The ice bath was also used to maintain the temperature at 30 °C during the sonication process. Thus, GO was exfoliated into a monolayer, and the average size of flakes could also be controlled.

3.2 Preparation and printing of rGO-based inks

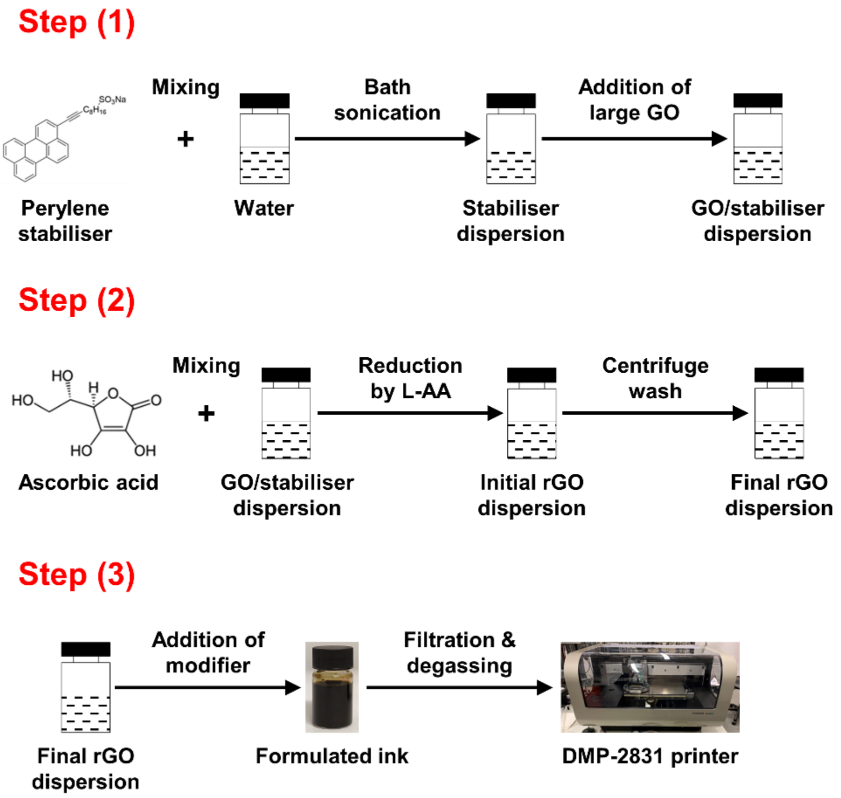

Figure 24 Standard ink formulation process from the initial rGO dispersion to printable graphene ink. Step (1) preparation of ‘initial rGO dispersion’; step (2) preparation of inkjet printable ink; and step (3) inkjet printing of the formulated rGO ink.

Figure 24 shows the standard preparation and printing process of rGO-based inks in this project. The whole process can be divided into three steps, which are the preparation of rGO dispersion, the formulation of the ink, and inkjet printing of the ink.

In step (1), 9 mg of perylene stabiliser (team-made perylene derivative, not commercially available, GO to stabiliser mass ratio of 1/1.5) was first dispersed into 4 ml DI water via bath sonication with ice (Elmasonic P 70 H Sonicator, with 100% power at 37 kHz for 48 hours). Then, 2 ml of GO (3 mg/ml) was mixed with the perylene suspension by vortex mixing (LP Vortex Mixer, Thermo Fisher Scientific) at a speed of 500 rpm for 3 minutes.

In step (2), the above suspension was mixed with ascorbic acid (≥ 99.0%, Sigma-Aldrich) in a GO/L-AA mass ratio of 1/7 via a vortex mixer for another 3 minutes at a speed of 500 rpm. The formed mixture was placed in the oven (Model ED 115, BINDER GmbH) for a 72-hour thermal reduction at 80 °C. Then, a continuous centrifuge washing process was performed to remove the excessive perylene stabiliser in the mixture after the reduction process. During each washing process, 2 ml of rGO dispersion was centrifuged at 6 krpm for 45 minutes, and 1.5 ml of the supernatant was discarded and replaced by DI water. The final rGO sample was collected after the seventh round of washing, and the 1.5 ml supernatant was discarded; the rest of the mixture was labelled ‘final rGO dispersion’ and was ready for the formulation of the rGO-based ink.

In step (3), the ‘final rGO dispersion’ was mixed with 1.5 ml of modifier to form the rGO-based inks. The modifiers were prepared by mixing different loadings of EG (anhydrous, 99.8%, Sigma-Aldrich) and Triton X-100 (laboratory grade, Sigma-Aldrich) with 1.5 ml DI water. The loadings of EG and Triton X-100 were set based on existing literature[18,74] at the beginning and altered based on the results from later explorations. Then, the formulated ink was filtered with glass wool (Fisher Scientific) and degassed via a bath sonicator before loading into the cartridge. The material printer used in the project was Dimatix 2831 (Dimatix-Fujifilm Inc.), and the cartridge used was DMC-11610 (10 pL). The waveform needed to be modified before the formal printing. The modification focuses on adjusting the durations of each segment in the standard waveform (designed by Fujifilm Inc.) based on the jetting performance of loaded inks. The aim of this modification is to print the formulated ink without jetting issues, and it could be further improved if a newly loaded ink has jetting issues.

It is worth noting how the ink formulated in this project was named. For example, the full name of Ink 1 in the project is ‘0.25 mg/ml rGO, 0.1/1 (by volume) EG/DI, 0.1 mg/ml Triton X-100’, in short ‘0.25rGO, 0.1/1EG, 0.1Tri’. The average flake size is also added to the end, so the formal short name of Ink 1 is expressed as ‘Ink 1-(0.25rGO, 0.1/1EG, 0.1Tri)-1.5μm’. The same nomenclature is used for all the inks formulated in this project.

3.3 Characterisations of GO, rGO, and formulated inks

As for the characterisations of flake sizes, the samples were all spin coated (WS-650-23 Spin Coater, Laurell Technologies) on a cleaned Si wafer at 1000 rpm for 30 s. A standard cleaning process was applied to wash all the substrates before the spin coating process. The substrate should be first sonicated in an acetone bath for 3 mins and then cleaned in an IPA sonibath for another 2 mins. Then, the cleaned substrate was dried with a nitrogen gun.

SEM (Zeiss EVO60) was used to characterise the average flake size of rGO from different initial rGO dispersions. The reason for using flakes from initial rGO dispersion rather than printed dots is due to the folding issue of large flakes during the inkjet printing process[18]. ImageJ software was used to analyse the average flake size. Horizontal pixels of 10 μm scale in the collected SEM images were processed so that each pixel corresponded to a certain physical length. During the measurement, the maximum length of each rGO flake measured in the horizontal direction is referred to as its lateral size. Thus, the pixels of these lengths can be converted to actual lengths by ImageJ. For each type of rGO, a minimum of 600 individual flakes were measured so that the average flake size could be calculated.

AFM (Dimension FastScan, Bruker) was used to characterise flake size with a tapping mode. The thicknesses of GO and rGO/stabiliser were measured. The rGO/stabiliser flakes were spin coated from the initial rGO dispersion to check the thicknesses of flakes in the formulated ink. The GO flakes were spin coated on a Si wafer to check the thicknesses and layers of used GO. GO originates from the prepared, diluted, and sonicated GO dispersions.

The Kratos Axis Ultra DLD XPS spectrometer was used to conduct X-ray photoelectron spectroscopy (XPS) of washed GO/stabiliser and washed rGO/stabiliser samples. Accordingly, the reduction of GO could be verified. The samples for the XPS test were prepared by drop casting the samples onto cleaned Si wafers. Vacuum drying was also used to avoid contamination of the samples from the atmosphere.

As for the measurement of the rheological properties of the formulated inks, a Discovery HR-2 rheometer from TA Instruments was used to conduct the viscosity measurement. The geometry used was a 2° cone plate with a 60 mm diameter and 54 µm truncation gap. The measurement process required a 20 mins equilibration for each ink (usually ~2 ml) at 25 °C before running. The shear rate ranged from 0 – 1000 s^{-1}, and the test mode was set as both flow ramp and flow sweep.

In terms of the surface tension measurement, a drop shape analyser (KRÜSS DSA100, GmbH) was used to measure the surface tension of the formulated ink. The characterisation was carried out via a syringe with a 1.8 mm needle at 25 °C. The pendant drop method was used to calculate the surface tension of the formulated inks.

Regarding ink density, all ink densities were assumed as 1 mg/µl for the Z number calculation.

3.4 Exploration on the suppression of drying issues by printer settings and substrate modifications

There were several drying issues (CRE, first dot issue, missing front issue and waviness) found during the printing of Ink 1-(0.25rGO, 0.1/1EG, 0.1Tri)-1.5µm. This section explores the effects of printer settings and substrate modifications on these drying issues. A modified waveform and a cleaned Si wafer were used for the printing of Ink 1-(0.25rGO, 0.1/1EG, 0.1Tri)-1.5µm. A Nikon Eclipse LV100ND optical microscope (standard mode, no polarised light) captured images of the printed patterns on cleaned Si wafers.

The initial combination of printer settings and substrate modifications used to print Ink 1-(0.25rGO, 0.1/1EG, 0.1Tri)-1.5µm were as follows:

1. Drop spacing: 200 µm for individual dots, 25 µm for lines and films;
2. Maximum printing frequency (MPF): 1 kHz;
3. Cartridge temperature: room temperature;
4. Platen temperature: 60 ℃;
5. UV time: 20 mins.

The UV Ozone cleaner used in this project was ProCleaner™ Plus from BioForce Inc. The first three factors were the adjustable printer settings, and the latter two factors were major substrate modifications used in the project. The drying issues found during the printing of Ink 1-(0.25rGO, 0.1/1EG, 0.1Tri)-1.5µm were observed under the above settings and modifications. Table 4 presents different printer settings and substrate modifications used for the suppression of drying issues found in the printed patterns from Ink 1-(0.25rGO, 0.1/1EG, 0.1Tri)-1.5µm.

Printer settings	**Drop spacing (µm)**	20	25	30	35	40	50	60	70	80
	MPF (kHz)	1	5	10	15					
	Cartridge temperature (℃)	RT*	60							
Substrate modifications	**Platen temperature (℃)**	RT*	60							
	UV time (mins)	0	20							

RT stands for room temperature.

Table 4 Printer settings and substrate modifications used to supress the drying issues found in Ink 1-(0.25rGO, 0.1/1EG, 0.1Tri)-1.5µm. The drop spacing and MPF are used to explore the relationship between the drying issues and droplet coalescence; the cartridge and platen temperature are used to explore the relationship between the drying issues and droplet evaporation rate. Then, the UV time investigates the surface wettability effect on ink drying issues.

3.5 Exploration on the suppression of drying issues via ink formulations and substrate modifications

Various ink formulations have been prepared by mixing initial rGO dispersion with corresponding modifiers to explore the suppression of drying issues. Since the cost of the printhead used in this project is high, it was not cost-effective to load and print every formulated ink. Thus, drying uniformity was investigated by placing sessile droplets on controlled substrate in this section. 1 µl of droplet from the formulated ink was manually placed on a cleaned and modified Si wafer. The ink formulation '0.1 mg/ml rGO, 0.01/1 (by volume) EG/DI, 0.2 mg/ml Triton X-100' (short for 0.1rGO, 0.01/1EG, 0.2Tri; the same nomenclature is used for all the formulations in this section) was used as the initial sample. rGO flakes with an average size of 1.5 µm were used for all the inks formulated in this section. 20 mins of UV and a platen temperature at room temperature were used as a starting point and changed accordingly based on the findings of later exploration. Then, two major steps were taken to achieve the full investigation:

(1) exploration of the individual formulation and substrate modification factors on drying issues;
(2) exploration of the effect of modifiers on drying issues and the effects of rGO loading, platen temperature, and UV time on this modifier's effect.

Ink formulation	**rGO loading (mg/ml)**	0.1	0.5			
	EG/DI water (By volume)	0.01/1	0.05/1	0.1/1	0.5/1	1/1
	Triton X-100 loading (mg/ml)	0.2	0.1	0.06		
Substrate modifications	**Platen temperature (°C)**	RT*	60			
	UV time (mins)	0	20			

RT stands for room temperature.

Table 5 The loadings of EG, Triton, and rGO used for the ink preparation and applied modifications on the substrate (UV time and platen temperature) for droplet drying.

In terms of step (1), table 5 shows a summary of loadings of EG, Triton, and rGO for the ink preparation and the applied modifications on the substrate (UV time and platen temperature) for the droplet drying.

Ink ‘0.1rGO, 0.01/1EG, 0.2Tri’ with substrate modifications (0 min UV at room temperature) was used as the formulation and settings for the start point in this section.

Inks with different Triton loadings (0.1, 0.06 mg/ml) were formulated, and the droplets were placed on substrates with the same modifications as a starting point. After that, the formulation with the best drying uniformity was used for exploration of the effect of EG, which was ink ‘0.1rGO, 0.01/1EG, 0.06Tri’. Then, four more inks with different EG/DI ratios (0.05/1 – 1/1) were prepared. The UV time was still 0 min for the substrate, and the platen temperature remained at room temperature. Thus, the formulation with the best drying uniformity was found in this case, which was ‘0.1rGO, 0.5/1EG, 0.06Tri’.

In the final phase of step (1), inks with different rGO loading (0.5 mg/ml) from ink ‘0.1rGO, 0.5/1EG, 0.06Tri’ were prepared and dried under the same substrate modifications again to explore the effect of rGO loading. Then, ink ‘0.1rGO, 0.5/1EG, 0.06Tri’ were dried on the substrates treated with different UV time (20 minutes) and platen temperatures (60 °C) so the effects of UV time and platen temperature could be explored.

Triton loading (mg/ml) / **EG/DI ratio**	**0.2**	**0.1**	**0.06**
0.01/1	0.1rGO, 0.01/1EG, 0.2Tri	0.1rGO, 0.01/1EG, 0.1Tri	0.1rGO, 0.01/1EG, 0.06Tri
0.05/1	0.1rGO, 0.05/1EG, 0.2Tri	0.1rGO, 0.05/1EG, 0.1Tri	0.1rGO, 0.05/1EG, 0.06Tri
0.1/1	0.1rGO, 0.1/1EG, 0.2Tri	0.1rGO, 0.1/1EG, 0.1Tri	0.1rGO, 0.1/1EG, 0.06Tri
0.5/1	0.1rGO, 0.5/1EG, 0.2Tri	0.1rGO, 0.5/1EG, 0.1Tri	0.1rGO, 0.5/1EG, 0.06Tri
1/1	0.1rGO, 1/1EG, 0.2Tri	0.1rGO, 1/1EG, 0.1Tri	0.1rGO, 1/1EG, 0.06Tri

UV time and platen temperature maintained at 0 min and room temperature, rGO loadings were 0.1 mg/ml for all inks .

Table 6 Formulations for exploring the collective effects of EG and Triton on droplet drying uniformity. Only the loadings of EG and Triton were changed; other factors were kept the same as the base conditions of this section.

In step (2), the same base conditions from above were used. Since the addition of the modifier aims to modulate the rheological properties of formulated ink into a suitable range for inkjet printing, both loadings of EG and Triton could be changed at the same time. To investigate the collective effect of EG and Triton on droplet drying, 15 formulations were prepared based on the starting point and are shown in table 6. It is worth noting that only the loadings of EG and Triton were changed; the other factors (rGO loading, UV time, and platen temperature) were kept constant.

Afterwards, table 7 shows another 15 inks with the same EG and Triton loadings as table 6, but the rGO loading was increased from 0.1 to 0.5 mg/ml to study the effect of rGO loading on the collective effect of EG and Triton on droplet drying. To investigate the effects of UV time and platen temperature on droplet drying, 15 inks with the same formulations as table 6 were prepared, but the UV time was changed from 0 to 20 minutes. Additionally, 15 inks with the same formulations as table 6 were prepared, but the platen temperature was changed from room temperature to 60 °C. The details of these 30 formulations are summarised in tables 8 and 9, respectively. In addition, rGO flake size was maintained at ~1.5 µm for all formulations to exclude the effect of flake size on droplet drying. Optical images were collected to observe the different effects of the above factors on the drying uniformity.

Triton loading (mg/ml) / **EG/DI ratio**	**0.2**	**0.1**	**0.06**
0.01/1	0.5rGO, 0.01/1EG, 0.2Tri	0.5rGO, 0.01/1EG, 0.1Tri	0.5rGO, 0.01/1EG, 0.06Tri
0.05/1	0.5rGO, 0.05/1EG, 0.2Tri	0.5rGO, 0.05/1EG, 0.1Tri	0.5rGO, 0.05/1EG, 0.06Tri
0.1/1	0.5rGO, 0.1/1EG, 0.2Tri	0.5rGO, 0.1/1EG, 0.1Tri	0.5rGO, 0.1/1EG, 0.06Tri
0.5/1	0.5rGO, 0.5/1EG, 0.2Tri	0.5rGO, 0.5/1EG, 0.1Tri	0.5rGO, 0.5/1EG, 0.06Tri
1/1	0.5rGO, 1/1EG, 0.2Tri	0.5rGO, 1/1EG, 0.1Tri	0.5rGO, 1/1EG, 0.06Tri

UV time and platen temperature maintained at 0 min and room temperature, rGO loadings were 0.5 mg/ml for all inks .

Table 7 Formulations for exploring the effect of rGO loading on the collective effects of EG and Triton on droplet drying uniformity. These 15 inks have the same EG and Triton loadings, UV time, and platen temperature as the inks prepared in table 6, but the rGO loading was increased from 0.1 to 0.5 mg/ml.

Triton loading (mg/ml) EG/DI ratio	0.2	0.1	0.06
0.01/1	0.1rGO, 0.01/1EG, 0.2Tri	0.1rGO, 0.01/1EG, 0.1Tri	0.1rGO, 0.01/1EG, 0.06Tri
0.05/1	0.1rGO, 0.05/1EG, 0.2Tri	0.1rGO, 0.05/1EG, 0.1Tri	0.1rGO, 0.05/1EG, 0.06Tri
0.1/1	0.1rGO, 0.1/1EG, 0.2Tri	0.1rGO, 0.1/1EG, 0.1Tri	0.1rGO, 0.1/1EG, 0.06Tri
0.5/1	0.1rGO, 0.5/1EG, 0.2Tri	0.1rGO, 0.5/1EG, 0.1Tri	0.1rGO, 0.5/1EG, 0.06Tri
1/1	0.1rGO, 1/1EG, 0.2Tri	0.1rGO, 1/1EG, 0.1Tri	0.1rGO, 1/1EG, 0.06Tri

UV time and platen temperature maintained at 20 mins and room temperature, rGO loadings were 0.1 mg/ml for all inks .

Table 8 Formulations for exploring the effect of UV time on the collective effects of EG and Triton on droplet drying uniformity. These 15 inks have the same rGO, EG, and Triton loadings and platen temperature as the inks prepared in table 6, but the UV time was increased from 0 to 20 mins.

Triton loading (mg/ml) EG/DI ratio	0.2	0.1	0.06
0.01/1	0.1rGO, 0.01/1EG, 0.2Tri	0.1rGO, 0.01/1EG, 0.1Tri	0.1rGO, 0.01/1EG, 0.06Tri
0.05/1	0.1rGO, 0.05/1EG, 0.2Tri	0.1rGO, 0.05/1EG, 0.1Tri	0.1rGO, 0.05/1EG, 0.06Tri
0.1/1	0.1rGO, 0.1/1EG, 0.2Tri	0.1rGO, 0.1/1EG, 0.1Tri	0.1rGO, 0.1/1EG, 0.06Tri
0.5/1	0.1rGO, 0.5/1EG, 0.2Tri	0.1rGO, 0.5/1EG, 0.1Tri	0.1rGO, 0.5/1EG, 0.06Tri
1/1	0.1rGO, 1/1EG, 0.2Tri	0.1rGO, 1/1EG, 0.1Tri	0.1rGO, 1/1EG, 0.06Tri

UV time and platen temperature maintained at 0 min and 60 °C, rGO loadings were 0.1 mg/ml for all inks .

Table 9 Formulations for exploring the effect of platen temperature on the collective effects of EG and Triton on droplet drying uniformity. These 15 inks have the same rGO, EG, and Triton loadings and UV time as inks prepared in table 6, but the platen temperature was increased from room temperature to 60 °C.

3.6 Inkjet printing of large rGO flakes

Seven inks were formulated based on the preparation process mentioned in section 3.2 with corresponding modifiers. The rheological properties of these inks were measured by the methods mentioned in section 3.3. Then, an evaluation of the Z numbers of these inks was conducted based on the collected rheological properties. The modified waveform was used to print inks with Z numbers out the range between 1 and 10 to ensure that the droplets could be jetted stably.

As for the formal printing of these inks, the first step was to clean all the substrates (Si wafer, PEN, and PI) with a standard cleaning process. All the substrates were cleaned with a 3-minute acetone sonibath with another 2-minute IPA sonibath, followed by a nitrogen gun blow to dry. Then, a 20-minute UV Ozone treatment was applied on each substrate before the formal printing of ink on it. All seven inks were used to print dots, lines, and squares to check pattern drying uniformities under controlled printer settings and substrate modifications. These modified printer settings and substrate modifications were determined from the previous exploration sections. 200 µm was used as the drop spacing for printed dots, and X µm (X = radius of the dried droplet) was used for printed lines and squares. The MPF was maintained at 1 kHz for the printing of all inks, while the cartridge and platen temperatures were kept at room temperature and 60 °C, respectively.

After the printing of these inks, the annealing of the printed patterns was conducted. 80 °C and 120 °C were used based on the glass transition temperature of the used substrate. For the samples printed on PET, 80 °C for 1 hour in the oven (Model ED 115, BINDER GmbH) was applied for the annealing process. Regarding the samples printed on Si wafer and PI, an addition of 120 °C for 1 hour was further applied. Then, a four-point-probe station from Jandel Engineering combined with a Model 2182A Nanovoltmeter and a Series 2400 Source Measure Unit (Keithley) were used to measure the sheet resistances of these annealed patterns.

In the end, the exploration of further reduction of sheet resistance and other relevant properties could not be done due to the COVID-19 pandemic; the project stopped at this step.

Chapter 4. Results and discussions

4.1 Characterisation of GO and rGO

Figure 25 (a) – (c) show the SEM images of different types of rGO/stabiliser flakes on Si wafer and their corresponding average flake sizes. As mentioned in the experimental section, the final formulated inks were prepared by mixing the ‘initial rGO dispersions’ with the corresponding modifiers (mixture of DI water, Triton, and EG), so the average flake size of initial rGO corresponds to the average flake size of the formulated ink. The reason for using the average flake size of the initial rGO dispersion is due to the inevitable folding issue of large flakes during inkjet printing[18], so the accuracy of the average flake size of printed ink is not reliable.

(a)

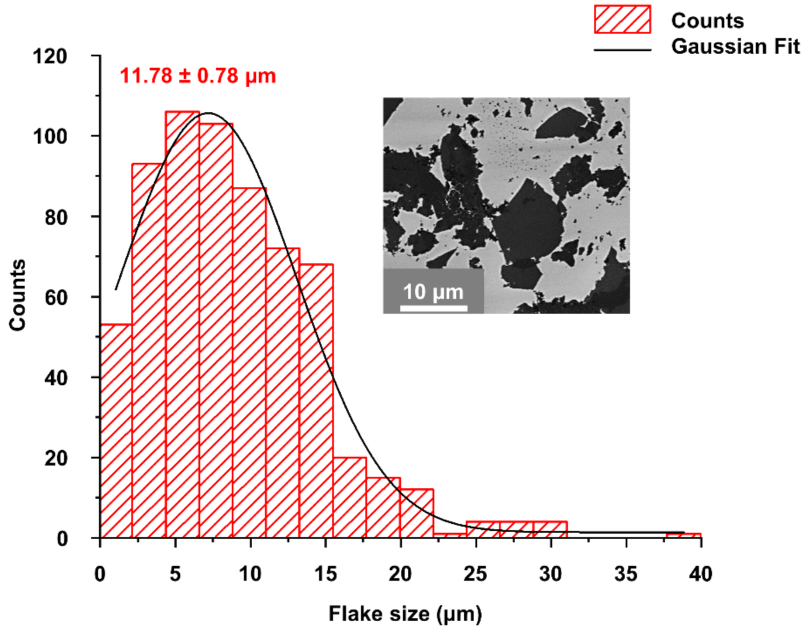
Counts
Gaussian Fit
11.78 ± 0.78 µm
10 µm
120
100
80
60
40
20
0
Counts
0
5
10
15
20
25
30
35
40
Flake size (µm)

(b)

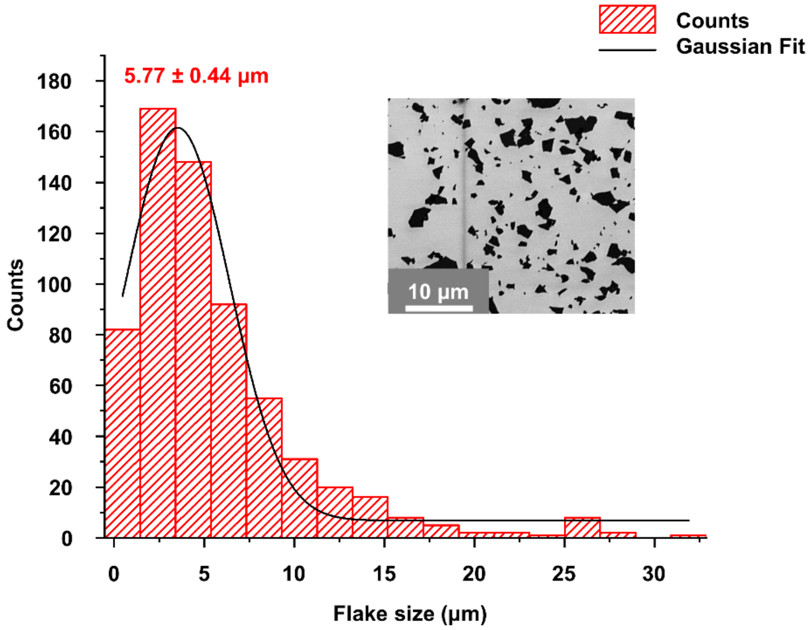
Counts
Gaussian Fit
5.77 ± 0.44 µm
10 µm
180
160
140
120
100
80
60
40
20
0
Counts
0
5
10
15
20
25
30
Flake size (µm)

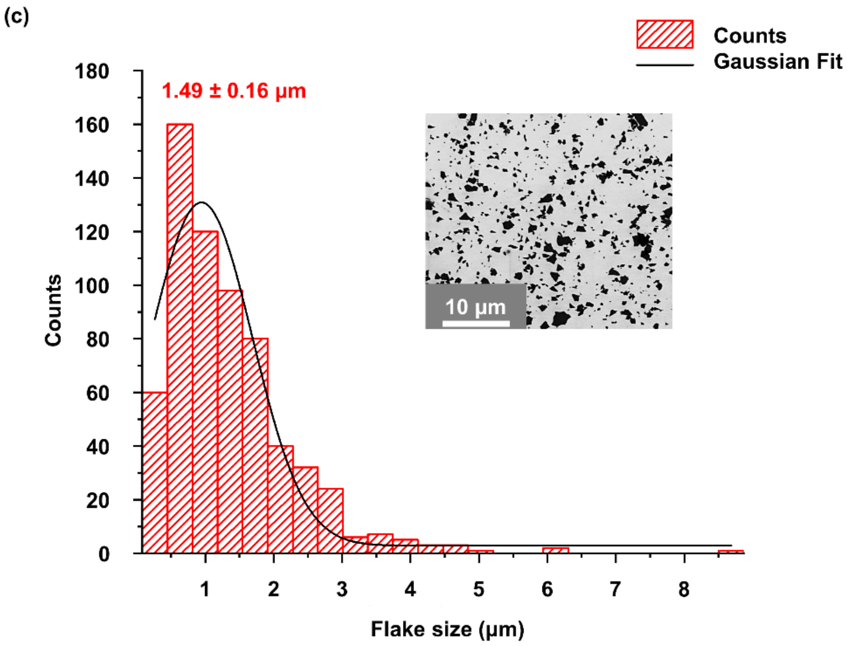

Figure 25 (a) – (c) SEM images and corresponding histograms of the three types of GO prepared in the project. The aim of reducing the flake size is to check the maximum printable flake size in this project. The graphene with a flake size of ~1.5 μm was first used to prepare the printable ink, and then the larger flakes were used to replace this type of graphene in the same formulation to check the upper limit of the printable flake size in this project.

Since the 'formulated ink' was prepared by final rGO dispersion mixed with stabiliser, the size of used GO is the key to controlling the ink's average flake size. Therefore, the initial GO dispersion prepared by the modified Hummer's method was diluted into a GO dispersion with a concentration of 3 mg/ml. Then, different sonication times (12, 18, and 24 hours) with the same frequency (37 kHz) were applied to this GO dispersion to reduce the flake size of GO at first. The ice bath was used to maintain the temperature near room temperature. Thus, GO dispersions with different average flake sizes could be prepared. Then, these GO dispersions were used to prepare the 'final rGO dispersions' through the method mentioned in the experimental section. Finally, these dispersions were spin coated on a cleaned Si wafer for the flake size characterisation. The average flake size corresponding to different sonication times were (a) 11.78 ± 0.78 μm (12 hours), (b) 5.77 ± 0.44 μm (18 hours), and (c) 1.49 ± 0.16 μm (24 hours). The aim of preparing the initial rGO dispersions with different average flake sizes is to check the upper limit of the printable flake size on the printhead (DMC-11610) used in this project. As the results reveal, the smallest average flake size is ~1.5 μm. Since the aim of this project is to print large graphene flakes, it is important to define ‘large’ as it relates to this project. It is commonly accepted that the particle size for inkjet printing should not exceed 1/50 of the nozzle diameter to avoid issues with clogging[36]. Thus, the maximum material size for the printhead (DMC-11610, nozzle diameter of about 21.5 µm) used in this project is 0.43 µm. Thus, any average flake size greater than this value is denoted as ‘large’. Accordingly, all three types of rGO/stabiliser flakes prepared in the project are considered ‘large’ graphene flakes.

Consequently, an average flake size of ~1.5 µm was used to prepare inks in this project. Since the challenges of this project were not only the printability of large flakes but also the dying uniformity of prepped inks, this average flake size was used as the standard size to prepare all types of inks at first. Once the balance between the printability of large flakes and ink drying uniformity was achieved, an even larger average flake size was used in inks with the same formulations to check the upper limit of the printable flake size in this case.

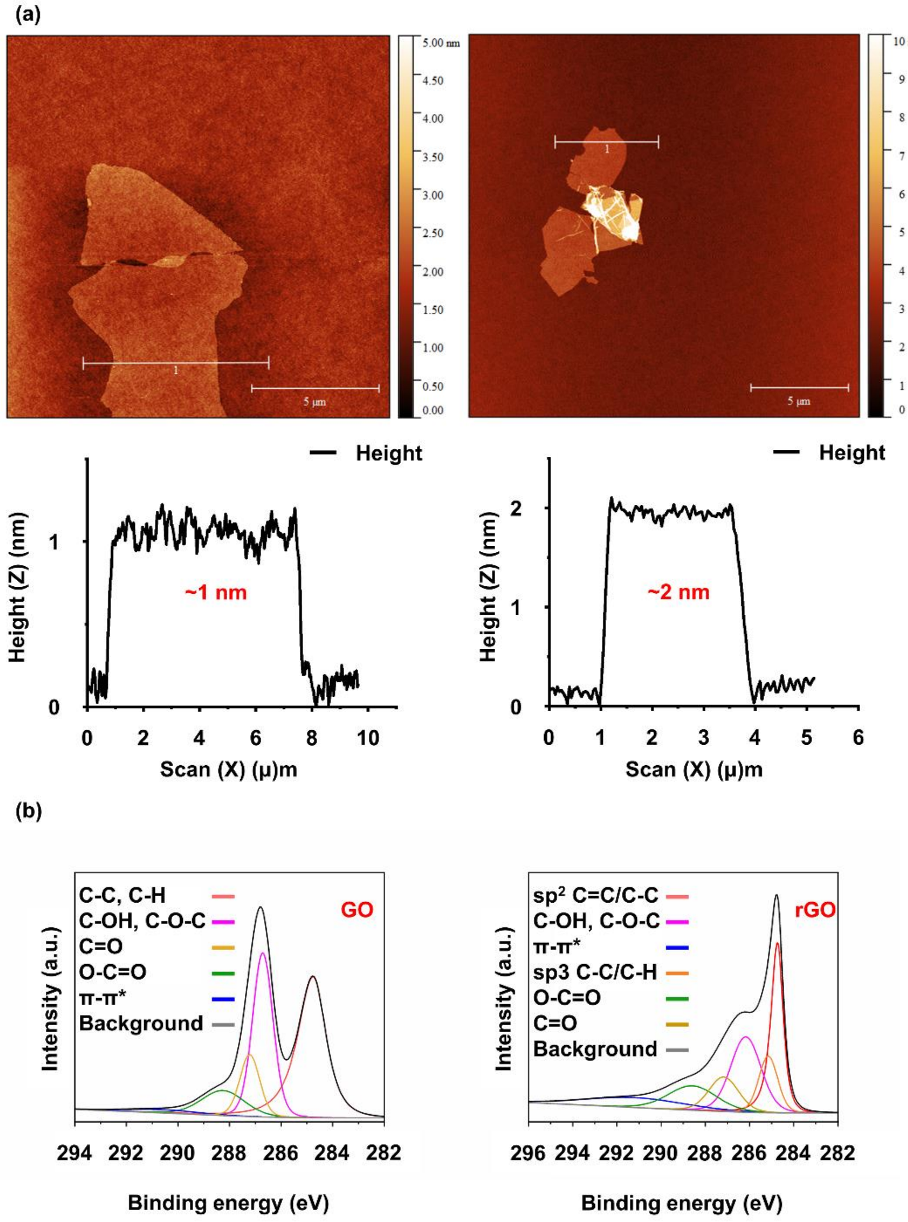

Figure 26 (a) AFM thickness check of GO (~1 nm) and rGO/stabiliser flakes (~2 nm); (b) XPS of GO/stabiliser (left) and rGO/stabiliser (right), the C/O ratio changed from 2.50 to 3.07 after the reduction. The AFM measurements have two aims; one is to confirm the layer and thickness of the GO used in this project, and the other is to check the attachment of the stabiliser on rGO after the reduction and washing processes via the thickness change. The XPS is used to check the reduction degree of the rGO flakes used. Thus, the preparation of dispersions loaded with large monolayer rGO flakes could be confirmed.

Figure 26 (a) shows the AFM results of measured GO and rGO/stabiliser flakes from sonicated GO dispersions (12 hours) and the corresponding initial rGO dispersion. The thickness of GO is ~1 nm, which is close to the reported thickness of a monolayer of GO[140]. Accordingly, the flakes in these sonicated dispersions are confirmed as a monolayer of GO flakes. Thus, the monolayer rGO dispersions could be prepared by using these GO dispersions. However, the thickness of rGO/stabiliser flakes is ~2 nm, which is even larger than the thickness of the used GO flake. This could be explained by the attachment of stabiliser molecules on both sides of the rGO flakes during the preparation of the initial rGO dispersion process.

XPS has been used to characterise the reduction degree of rGO/stabiliser, and the results are shown in figure 26 (b). Only one reduction method and corresponding conditions were used to reduce GO in this project (GO/L-AA mass ratio of 1/7 at 80 °C for 72 hours). This is because the priority of the project is to print large rGO ink without drying issues, and further improvement on reduction was not conducted due to COVID-19. The same GO/stabiliser dispersion has been divided into two portions. One is reduced through the steps mentioned in the experimental section, and the other is maintained as a GO/stabiliser dispersion. As the XPS results show, the peaks of C–O and C=O components like hydroxyl (284.5 eV), epoxide (286.6 eV), and carboxyl (288 – 299 eV) functionalities could be observed in the C1s spectra of both GO and rGO. This is because they are the chemicals with similar structures but different degrees of reduction. The C/O ratio changed from 2.50 to 3.07 before and after the reduction process, which indicates the removal of oxygen groups in rGO. In addition, some extra Raman characterisations of GO and rGO reduced without the stabiliser under the same reduction method and conditions used in the project have also been presented as supplemental information and shows in the Appendix (figure S1).

In all, the initial rGO dispersions with different average flake sizes have been prepared for the preparation of large rGO water-based inks. The thickness and reduction degree of loaded rGO flakes have been characterised to give a better understanding of the used materials in the formulated inks.

4.2 Formulation and inkjet printing of the initial inks

4.2.1 Preparation of the initial inks

Using inkjet printable large rGO water-based ink to print FTEs is a novelty of this project. This is the first time that such large rGO flakes are stably printed from a DMP-2831 printer and that the effect of large rGO flakes on printed FTEs is studied. As mentioned in the review section, the rGO-based FTEs could avoid harsh post-treatment, which is beneficial to the selection of flexible and transparent substrates. However, the majority of rGO-based FTEs suffer from low electrical conductivity due to the use of stabiliser and the reduction degree of GO[111,112,113]. So, the use of large rGO flakes could provide a new solution to the above challenge, as the large flake size could provide improved interconnections among the flakes in printed FTEs and deliver better electrical conductivity.

Since this project uses large rGO with perylene stabiliser to prepare the inkjet printable ink, two initial inks were designed based on the reported inkjet printable water-based GNP ink[74] and the inkjet printable ultra-large GO ink[18]. The former is a typical example of using PAHs as the stabiliser for water-based graphene ink to obtain a high stabiliser to graphene ratio; the latter is the first example to prove the inkjet printability of large graphene flakes. These two examples are also the origins of this project. In this project, Triton and EG are selected as the surfactant and thickener, respectively. The Triton is used to avoid the interruption of electrostatic stabilisation formed by the pyrene stabiliser, which is also suitable for this project. The EG is selected as a common thickener for water-based ink, and it is easy to remove with thermal annealing.

The full names of the two initial inks are ‘Ink 1-0.25 mg/ml rGO, 0.1/1 (by volume) EG/DI, 0.1 mg/ml Triton X-100-1.5μm’ and ‘Ink 1-0.25 mg/ml rGO, 0.1/1 (by volume) EG/DI, 0.1 mg/ml Triton X-100-5.8μm’. The 1.5 and 5.8 μm denotations are the average flake sizes of used rGO. Furthermore, these two names are shorted and expressed as Ink 1-(0.25rGO, 0.1/1EG, 0.1Tri)-1.5μm and Ink 1-(0.25rGO, 0.1/1EG, 0.1Tri)-5.8μm, respectively. The same nomenclature is used for the inks formulated in section 4.5 as well.

Since the initial inks have been formulated, table 10 shows the factors that are significant for the printability and drying uniformity of prepared inks in this project. The loadings of rGO, Triton, and EG are the factors that impact the formulation and printability of these inks. The drop spacing and MPF control the coalescence of jetted droplets. In general, the bulge issue forms when inappropriate droplet spacing or MPF have been applied[129]. Then, the UV time, cartridge, and platen temperatures are the factors which potentially affect the drying of the droplets deposited on the substrate[13]. The first three factors are more related to the ink itself, while the latter factors are more related to the printer settings and substrate modifications.

Formulation-related factors	**rGO loading (mg/ml)**	0.1	0.5							
	EG/DI water ratio (by volume)	0.01/1	0.05/1	0.1/1	0.5/1	1/1				
	Triton loading (mg/ml)	0.2	0.1	0.06						
Printer settings	**Drop spacing (µm)**	20	25	30	35	40	50	60	70	80
	MPF (kHz)	1	5	10	15					
	Cartridge temperature (℃)	RT*	60							
Substrate modifications	**Platen temperature (℃)**	RT*	60							
	UV time (mins)	0	20							

RT stands for room temperature.

Table 10 The three types of factors concerned in this project for the formulation, printing, and drying of inkjet printable large rGO water-based inks; one is formulation-related factors, which are rGO loading, Triton loading, and the EG/DI ratio, the second is printer settings, which are drop spacing, MPF, and cartridge *temperature*, the last one is *substrate modifications*, which are UV time and platen temperature. The first type of factors determines the formulation of the ink, the second type affects the droplet coalescence on substrates, and the third type promotes the droplet evaporation rate of deposited droplets[13]. All these factors together have a collective effect on the drying uniformity of the final printed patterns.

Table 11 presents the rheological properties of Ink 1-(0.25rGO, 0.1/1EG, 0.1Tri)-1.5µm and Ink 1-(0.25rGO, 0.1/1EG, 0.1Tri)-5.8µm. Both inks have the same formulation; the main difference between these two inks is the average flake size of rGO. As table 11 shows, the surface tensions of the two inks are quite similar to each other. However, the viscosity of Ink 1-(0.25rGO, 0.1/1EG, 0.1Tri)-5.8µm is ~11.7% higher compared to that of Ink 1-(0.25rGO, 0.1/1EG, 0.1Tri)-1.5µm. Since the major difference between these two inks is the average flake size, the increase in the viscosity can be explained by the use of larger flakes. The larger flakes likely result in an increase in the interactions between the graphene layers and a higher shear resistance to the change of flow between adjacent fluid layers[141]. Thus, the viscosity of the ink could be increased in this case.

	Ink 1-(0.25rGO, 0.1/1EG, 0.1Tri)-1.5µm	Ink 1-(0.25rGO, 0.1/1EG, 0.1Tri)-5.8µm
Surface tension (mN/)	45.15 ± 0.17	45.48 ± 0.38
Viscosity at 1000 S^{-1} (mPa.s)	1.57 ± 0.01	1.75 ± 0.25
Density (mg/µl)	0.99 ± 0.01 (set as 1)	0.99 ± 0.01 (set as 1)
Droplet velocity (m/s)	6	6
Re number	82.17	73.44
We number	17.14	16.97
Z number	19.84	17.83

Table 11 Rheological properties and of Ink 1-(0.25rGO, 0.1/1EG, 0.1Tri)-1.5µm and Ink 1-(0.25rGO, 0.1/1EG, 0.1Tri)-5.8µm. The ink with larger average flakes has a higher viscosity than the ink with smaller average flakes. Both inks have Z numbers larger than 10, which is in the range of printing satellites[114].

Additionally, the graphs of the surface tension and viscosity of these two inks have been added to the Appendix and are shown in figures S2.

In terms of the calculation of the dimensionless numbers for inkjet printing, the droplet velocity has been set as 6 m/s, which is the preferred velocity for inkjet printing[92]. Plus, the densities of both inks are assumed to be 1 mg/µl (the same as water density). Then, the Z numbers of both inks were calculated based on equation 4, which are 19.84 and 17.83, respectively. Since the recommended Z number range for inkjet printing is $1 < Z < 10$[114] , and the Z numbers of these two inks are larger than 10, the viscosity is not high enough to supress the satellites. Thus, the suppression of this jetting issue is the focus of the next section. In the meantime, since the aim of this project is to formulate large rGO water-based inks for printing FTEs, the major solvent for the ink is water, which has a low viscosity (~1 mPa.s at 25°C) and a high surface tension (~72 mN/m at 25°C)[142]. In addition, in order to have better electrical conductivity, a thickener like EG, which has relatively lower viscosity compared to other polymer thickeners, is preferred, as it can easily be removed after annealing[18,74]. Therefore, the nature of water and the pursuit of high electrical conductivity makes the prepared inks have Z numbers outside of the ideal range ($1 < Z < 10$).

4.2.2 Optimisation of jetting behaviours via the modification of waveform

As mentioned in the previous section, both inks have Z numbers larger than 10, so they are in the range of printing satellites[114], as shown in figure 27. The Z number is the inverse of the Oh number, so a large Z number indicates a small Oh number[114]. A small Oh number means that the viscous force of the fluid is not dominating the movement of the flow, so a long column of ink is easily jetted out from the nozzle and forms satellites[123]. There are two major routes to supressing satellites; one is optimising the ink formulation into the ideal range[92], and the other is modifying the waveform[91].

First, for the modification of ink's rheological properties, the viscosity of the ink plays a vital role in the issue. The low viscosity could result in the formation of satellites due to the decreased viscous dissipation during the jetting process. No dampening effect can be formed to supress the Rayleigh instability of printed ligament, which results in the formation of satellites[118,143]. Regarding the surface tension, it also has been reported as a useful tool to supress satellite issues[144].

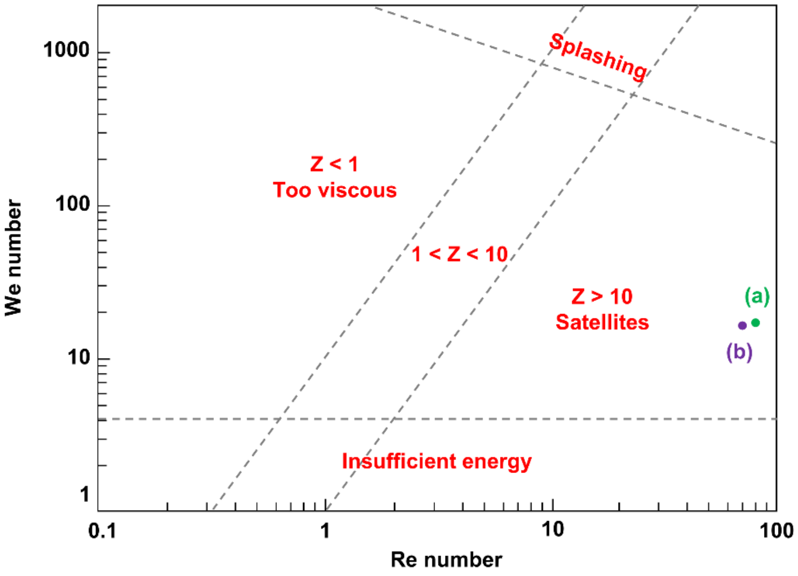

Figure 27 The relative positions of the Z numbers of (a) Ink 1-(0.25rGO, 0.1/1EG, 0.1Tri)-1.5µm and (b) Ink 1-(0.25rGO, 0.1/1EG, 0.1Tri)-5.8µm compared to the suggested range of Z numbers for inkjet printable inks. The larger Z numbers indicate that both inks are not viscous enough to dampen the Rayleigh instability and likely result in the formation of satellites[114].

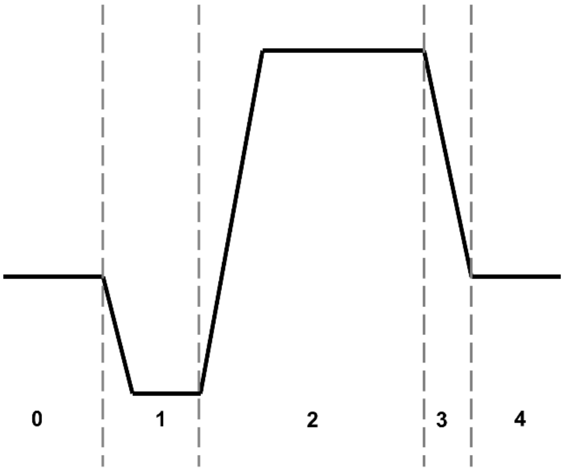

Figure 28 Schematic of a standard waveform of the DMP-2831 printer; there are five phases in this standard waveform, which are (0) the standby phase, (1) the suction phase, (2) the ejection phase, (3) the break-off phase, and (4) the recovery phase. The most important sections are phases (1) and (2), which are in charge of the suction and ejection of the ink in the printhead chamber[145].

A higher surface tension results in a larger surface energy of the droplet, which tends to minimise the surface area of the jetted droplet[146]. Thus, the droplet tail is decreased in this case, and the suppression of satellites could be achieved. However, the inks with extremely high surface tension or viscosity could still fail at jetting as a result of the limitations of the printer itself. Hence, a balance is needed between the ink formulation and printability; otherwise, the printhead is easily blocked[36]. Then, the optimising of ink formulation faces a practical challenge, which is the high cost of the printhead. Therefore, this method is not used at this stage.

Second, the effect of the waveform during inkjet printing is a determining factor of droplet ejection when the ink and printhead have already been selected. There are three main parameters in waveform design, which are amplitude, printing frequency, and waveform shape[92]. With the optimisation of these parameters, the droplet size can be manipulated without changing the ink formulation while still preventing satellites and nozzle clogging[121,147]. Generally, droplet velocity can be increased with an increase in amplitude, while the other parameters need to be adjusted based on the ink's fluid properties.

Figure 28 shows the standard waveform of a DMP printer, which can be divided into the following five phases[145]:

(1) Phase 0: In the standby phase, there is a small voltage applied on the piezo-transducer to slightly compress the chamber;
(2) Phase 1: The voltage applied in this phase is zero; the transducer is in a neutral status and has not been pressed. Hence, the ink is pulled into the chamber from the cartridge. The meniscus of the nozzle has been pulled inwards as well;
(3) Phase 2: The full voltage is applied to the transducer in this phase, and the volume of the ink in the chamber reaches its minimum. Hence, a droplet is ejected from the nozzle;
(4) Phase 3: In the recovery phase, the voltage is partially decreased, and the transducer relaxes. The droplet breaks off and forms a tail at this phase;
(5) Phase 4: In the recovery phase, the voltage keeps decreasing to the value set at phase 0. Another refilling process of the ink starts, and the whole system is ready for the next print.

The steepness of the slope is indicative of the energy that the printer applied upon ejection, and the section with zero gradient represents the holding time of each phase. The manipulation of the slope rate and phase time opens the opportunity to print inks with extreme properties, such as high surface tension or viscosity. Several inks reported with Z numbers between 2 and 24 had been printed out successfully without any jetting issues through the same printer used in this project[125,91], likely through the use of a modified waveform. Thus, this method has been selected at this stage to supress the satellites issue.

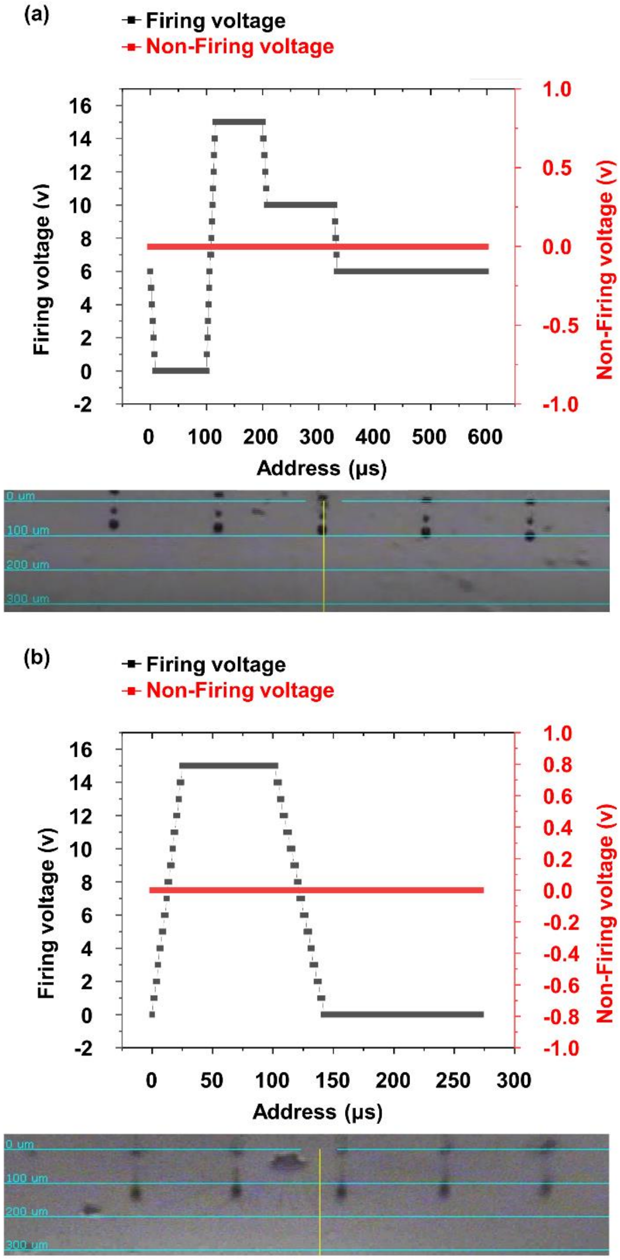

Figure 29 (a) Standard waveform and the screenshot of jetted droplets from Ink 1-(0.25rGO, 0.1/1EG, 0.1Tri)-1.5µm with satellites issue; (b) modified waveform and the screenshot of jetted droplets from Ink 1-(0.25rGO, 0.1/1EG, 0.1Tri)-1.5µm without satellites issue. These two waveforms are used to prove that waveform modification is an effective way to supress satellite issues without changing ink formulation. The modified waveform uses the optimised dwelling time to create a strong negative pressure at the ejection phase of the waveform[148]. Thus, the tail of the jetted droplet could be controlled, and the suppression of satellite issues could be achieved.

Figure 29 shows screenshots of jetted droplets from Ink 1-(0.25rGO, 0.1/1EG, 0.1Tri)-1.5µm under (a) standard and (b) modified waveforms. The satellites issue is observed when a standard waveform is used, but normal droplets are jetted out under a modified waveform.

The unipolar trapezoidal waveform is generally recommended because of its simplicity[149]. There are two major methods to supress the satellites via the modification of the waveform. One is simply applying a longer falling session to suppress the satellite issue[150]. It has been proved that a longer falling time creates a stronger negative pressure to the point that a droplet is pinched off from the nozzle. This stronger negative pressure reduces the length of the tail and results in a suppression of satellites issues.

The other method is finding the optimised dwelling time, which is usually denoted as dwelling efficient[148]. This method has been used to supress the satellite issue in a different type of printhead (Microfab, MJ-ATP-01-60-8MX). The main differences between this printhead and the one used in this project are the states of the piezoelectric elements during printing. In the above paper, the rising session of the printhead draws ink from the cartridge chamber, and the falling session ejects the droplet. This is reversed in the printhead used in this project. In that paper, the rising session first creates a negative pressure wave in the chamber. This wave gradually propagates to the nozzle, and the strength of this wave is weakened during the propagation due to the viscous damping effect of the ink. Then, a smaller and slower droplet is formed following the arrival of this weakened positive wave. After that, a larger and faster droplet is ejected, as the arrival of the positive pressure in the falling session. The dwelling efficient means the dwelling time that allows these two positive waves to meet in the nozzle at the same time. Hence, the maximum volume and the highest velocity of the droplet could be achieved.

Once the dwelling time is shorter than the efficient time, a larger and faster droplet is ejected first, and the smaller and slower droplet follows. However, the second droplet cannot catch up to the first droplet, and satellites are formed. On the other hand, if the dwelling time is longer than the efficient time, the faster droplet has the chance to catch up with the slower droplet and supresses the satellites. However, the satellites could also be formed when the dwelling time is too long, and the second droplet cannot catch up with the first droplet before it lands.

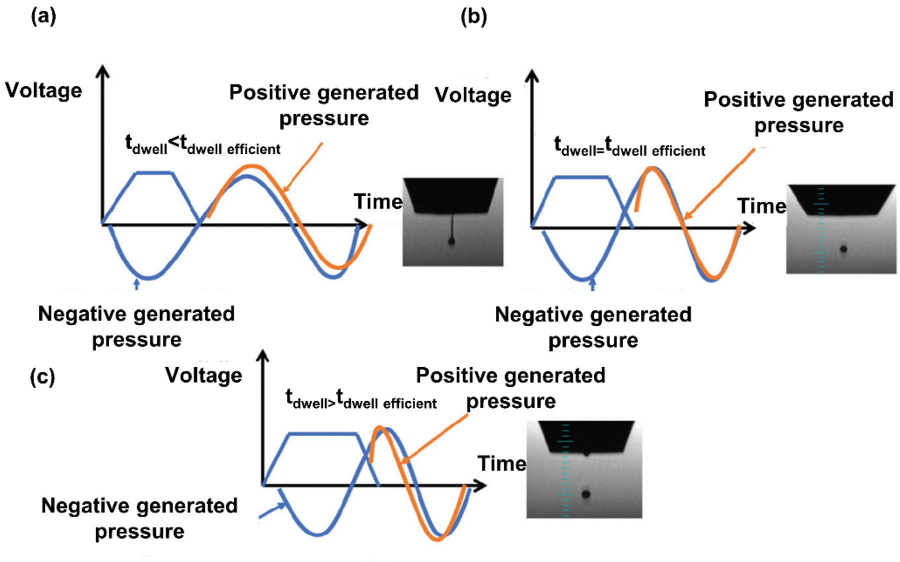

Figure 30 Dwelling time effect on the suppression of satellites issues on the Microfab printhead; (a) the dwelling time is shorter than the dwelling efficient, which promotes the formation of satellites; (b) the dwelling time equals the dwell efficient, wherein droplets with the maximum volume and the highest velocity are jetted out; and (c) the dwelling time is longer than the dwell efficient, which helps the suppression of satellite issues[148]. Since the same type of unipolar trapezoidal waveform has also been used in this project, a similar effect of dwelling efficient could be found on the Dimatix printhead as well. However, the dwelling efficient in Dimatix printhead is to strengthen the negative pressure and reduce the droplet tail to supress the satellite issue.

Figure 30 demonstrates the situations mentioned above[148]:

(a) Dwelling time shorter than the dwelling efficient;
(b) Dwelling time equal to the dwelling efficient;
(c) Dwelling time larger than the dwelling efficient.

So, a similar mechanism could be used to explain the effect of the waveform in this project since the state of the piezoelectric element in DMP-2831 is reversed in the rising and falling sessions. The rising session directly ejects the droplet at the beginning.

Hence, the first droplet is always large and fast. Even though the falling session could create a positive wave and eject a droplet, which is small, slow, and delayed, it is not likely to catch up with the previous droplet.

Nonetheless, it is interesting to highlight that if the negative pressure wave from the rising session meets the negative wave created at the start of the falling session at the same time, a strengthened negative pressure would be created. Then, an effect similar to a longer falling session could be formed[150]. Thus, the droplet tail could be reduced, and the satellite issue may be supressed.

As figure 29 (b) shows, the modified waveform has been simplified into three sections, which are rising, dwelling, and falling. The states of each section could be described based on the reported standard mechanisms as follows[92]:

(1) The piezoelectric element relaxes at the beginning with zero voltage applied and is ready to move into the rising section;
(2) The ink in the chamber is jetted out as the sudden rise of the applied voltage starts the rising section. The steepness of this slope determines the energy exerted on the initial ejection;
(3) In the dwelling section, the applied voltage has reached its maximum and holds for a certain time. No further deflection of the piezoelectrical element occurs in this section;
(4) The applied voltage starts to decrease at the start of the falling section, and the droplet tail pinches off from the nozzle. This section applies the negative pressure to eject the droplet. Finally, the ink refills the cartridge after the ejection of a droplet, and another jetting process starts.

The modified waveform was obtained by trial and error. Briefly, the rising section was set to 25 µs, with the firing voltage increased from 0 to 15 V. The dwelling section time was 77 µs, and the falling section time was 38 µs. The firing voltage was maintained at 15 V during the dwelling section and reduced to 0 V at the falling section. In addition, a 169 µs idle section of 0 voltage was applied to supress any unnecessary effects from pressure waves. The dwelling efficient was found to be 77 µs by the trial-and-error method. Both Ink 1-(0.25rGO, 0.1/1EG, 0.1Tri)-1.5µm and Ink 1-(0.25rGO, 0.1/1EG, 0.1Tri)-5.8µm could be jetted out successfully without any satellites issue via this modified waveform.

In all, a formulation has been designed based on previous work. The inks have satellites under the standard waveform due to their theological properties. The satellites issue has been supressed using a modified waveform. The mechanism of modification is to optimise dwelling and falling time in the waveform. Then, a strong negative pressure is created to suppress satellites issue during printing. Thus, the formulated inks could be jetted without changing their formulations.

4.3 Suppression of drying issues via printer settings and substrate modifications

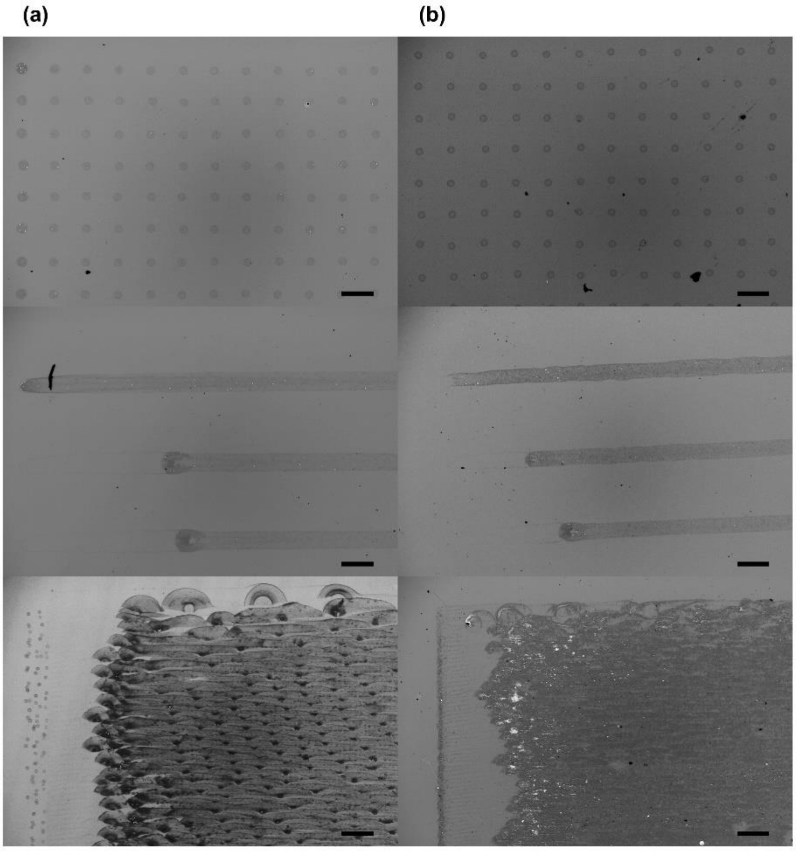

Figure 31 Optical microscope images of printed dots, lines, and squares on Si wafer from (a) Ink 1-(0.25rGO, 0.1/1EG, 0.1Tri)-1.5 µm and (b) Ink 1-(0.25rGO, 0.1/1EG, 0.1Tri)-5.8 µm. The patterns from the above inks were printed using 200 µm as the drop spacing for dots and 25 µm as the drop spacing for lines and squares. The MPF was 1 kHz, and the cartridge and platen temperatures were room temperature and 60 °C, respectively. The UV time for the Si wafer was maintained at 20 minutes for both inks as well. Four major drying issues could be found from the above-printed patterns, which are CRE, first dot issue, missing front issue, and waviness. No further application of these functional inks could be achieved until the suppression of these drying issues. Black scale bar represents 200 µm.

Since the ink jetting behaviours have been optimised, the drying uniformity of the printed patterns from both Ink 1-(0.25rGO, 0.1/1EG, 0.1Tri)-1.5 µm and Ink 1-(0.25rGO, 0.1/1EG, 0.1Tri)-5.8 µm become the focus of this section. Figure 31 shows the optical microscope images of printed dots, lines, and squares of these two inks on Si wafers. The printer settings and substrate modifications are as follows:

(1) drop spacing = 200 µm for dots and X µm (X equal to the average radius of printed dots) for lines and squares;

(2) maximum printing frequency (MPF) = 1 kHz;
(3) cartridge temperature = room temperature (RT);
(4) platen temperature = 60 °C;
(5) UV Ozone time = 20 mins.

The above settings and modifications are adopted from Pei's and Daryl's works as they originally formulated Ink 1, and both studies use the same type of printer as is used in this project[18,74]. These settings will be termed the 'initial settings' for the convenience of the coming discussion.

As figure 31 shows, individual dots could be observed when the drop spacing was set to 200 µm for both inks, and the average diameters of the printed dots from Ink 1-(0.25rGO, 0.1/1EG, 0.1Tri)-1.5µm and Ink 1-(0.25rGO, 0.1/1EG, 0.1Tri)-5.8µm were 52.0 ± 2.1 µm and 42.6 ± 1.5 µm, respectively. So, dots from Ink 1-(0.25rGO, 0.1/1EG, 0.1Tri)-5.8µm have a smaller average diameter compared to those of Ink 1-(0.25rGO, 0.1/1EG, 0.1Tri)-1.5µm. This could be explained by the higher viscosity of Ink 1-(0.25rGO, 0.1/1EG, 0.1Tri)-5.8µm since more energy is consumed by the higher viscous force during droplet spreading[151].

As mentioned before, the average radius of printed dots usually suggested determines the drop spacing for printing continuous patterns like lines and squares at start[92]. Thus, 25 µm and 20 µm have been set as the drop spacing for printing the lines and squares of these two inks. The corresponding average line widths of these two inks are about 122.5 ± 1.6 µm and 105.2 ± 1.1 µm, respectively. However, no uniform lines or squares could be observed in figure 31 for either ink. In addition, it is worth noting that the droplet diameters of both inks are smaller than the widths of their corresponding lines, which could be explained by the coalescence of printed droplets. The liquid volume in the printed line is far more than the liquid in a single droplet and results in further spreading of the ink on the substrate[114]. There are four major drying issues in the printed dots, lines, and squares in figure 31, which are:

(1) the coffee-ring effect (CRE);
(2) the first dot issue;
(3) the missing front issue;
(4) the waviness issue.

The first two are typical drying issues in inkjet printing[152], while the missing front and waviness issues are novel challenges found in this project. As mentioned in the literature review, the CRE is a phenomenon caused by capillary flow created due to the different evaporation rates between the contact line and the apex of the droplet[132]. The evaporation rate in the three-phase contact line region is higher than that of the apex region in a sessile droplet. Thus, more solvents are consumed in the contact line region, so the solvents in other regions are moved by capillary flow to replenish this loss. Thus, the transportation of solutes happens simultaneously in this process, and a non-uniform ring-structure deposition of the solutes is formed after drying. Therefore, as long as the pinned contact line and the edge dominated evaporation occur during the evaporation of the droplet, the CRE is inevitable[133].

The first dot issue could be observed in all printed patterns from both inks. The graphene loadings of the first dots or beginning parts of printed lines and squares are clearly higher than that of the rest of the printed dots, lines, and squares in the same printing sequence. It is believed that the drying of ink around the nozzle leads to this issue[36,92]. The continuous evaporation of ink during the idle period leads to a loss of solvent in the ink in and around the nozzle. This can either clog the nozzle or make the material loading of the first several droplets vary from the rest of the printed droplets in the same printing sequence[153]. Thus, either the nozzle clogs or the first dot issue occurs in this case. The common method to fix this issue is to set a frequent washing cycle during the idle session[92].

In terms of the missing front issue, empty sections could be observed at the front part of printed lines and squares. This is a new phenomenon first found in this project.

As for the waviness issue, the printed lines in a square have been transformed from straight lines into lines with wavy edges, which is similar to the bulge issue. However, as figure 31 shows, the individual lines printed with the same drop spacing do not have such wavy edges. This phenomenon is unique to this project as well. The mechanisms behind these two issues are explored in the following sections.

These four drying issues are the most critical challenges at this stage. These novel large rGO inks cannot be further applied until the drying uniformity issues have been supressed.

In general, there are two routes to supress drying issues during inkjet printing; one is changing the ink formulation, and the other is modulating the printer settings and substrate modifications[13]. Both routes can supress the drying issues effectively. However, the change of formulation could alter the rheological properties of the formulated inks and potentially cause printability issues in the new ink, especially when large flakes are used, like in this project[36]. Thus, ink reformulation is, again, not a cost-effective route. Thus, the modulation of printer settings and substrate modifications is first explored in this section.

In order to supress the drying issues, four printer settings and two substrate modifications have been explored. The settings and modifications can be divided into three groups:

(1) drop spacing and maximum printing frequency (MPF);
(2) cartridge and platen temperatures;
(3) UV Ozone time.

As mentioned before, inappropriate drop spacing and MPF result in other drying issues like a bulge and discrete depositions of ink, etc[114]. Thus, suitable drop spacing and MPF must be established first; the relationship between drying issues and these two settings can also be explored.

Regarding the cartridge temperature, it is a factor strongly related to the first dot issue. The first dot issue implies a dissimilarity of material loadings in the very first or the first several dots compared to the rest of the printed dots in the same printing sequence, which is caused by unpreventable ink wetting and drying around the nozzle during printing[153]. Therefore, printer settings like cartridge temperature play an important role in this issue, as it strongly influences the evaporation rate of ink around nozzle[92].

In terms of platen temperature, it is often used to supress the CRE. It has been reported that high platen temperature could either induce the thermal Marangoni effect or employ the surface capture effect to supress the CRE[154,155]. During droplet evaporation, high platen temperature leads to a decreasing gradient temperature from the contact line to the apex of the droplet. Thus, a surface tension difference could be formed in this case: if the surface tension in the apex is higher than at the contact line, then a thermally induced Marangoni flow could be formed[154]. Thus, the solute in the contact line area is transported back to the droplet centre and supresses the CRE. Moreover, it has been reported that high platen temperatures can result in the fast evaporation of a droplet, so the solutes in the droplet would be captured by the droplet surface due to this fast evaporation and results in a uniformly dried droplet[155]. So, the effect of platen temperature is also important in fixing drying issues.

Altering the UV time, in theory, changes the hydrophobicity of the substrate. On the one hand, the higher substrate hydrophobicity could result in a lower contact angle hysteresis. This weakened hysteresis could lead to the smoother receding of the contact line, preventing the accumulation of the solutes in the fixed contact that form the ring stain[156]. On the other hand, the spreading of solvent can also happen when the substrate is extremely hydrophilic, so the CRE could also be supressed due to an absence of the contact line[157]. Thus, a change in the UV time may also supress the drying issues.

Finally, the effects of the above settings and modifications on drying issues are discussed in the following sections. Importantly, since Ink 1-(0.25rGO, 0.1/1EG, 0.1Tri)-1.5µm and Ink 1-(0.25rGO, 0.1/1EG, 0.1Tri)-5.8µm have similar drying issues, Ink 1-(0.25rGO, 0.1/1EG, 0.1Tri)-5.8µm was excluded in following sections because of its low storage stability. The ink routinely suffers from nozzle clogging after 3 – 5 days of storage, which might be caused by the relatively larger rGO flakes.

4.3.1 Effects of drop spacing and MPF on suppressions of drying issues

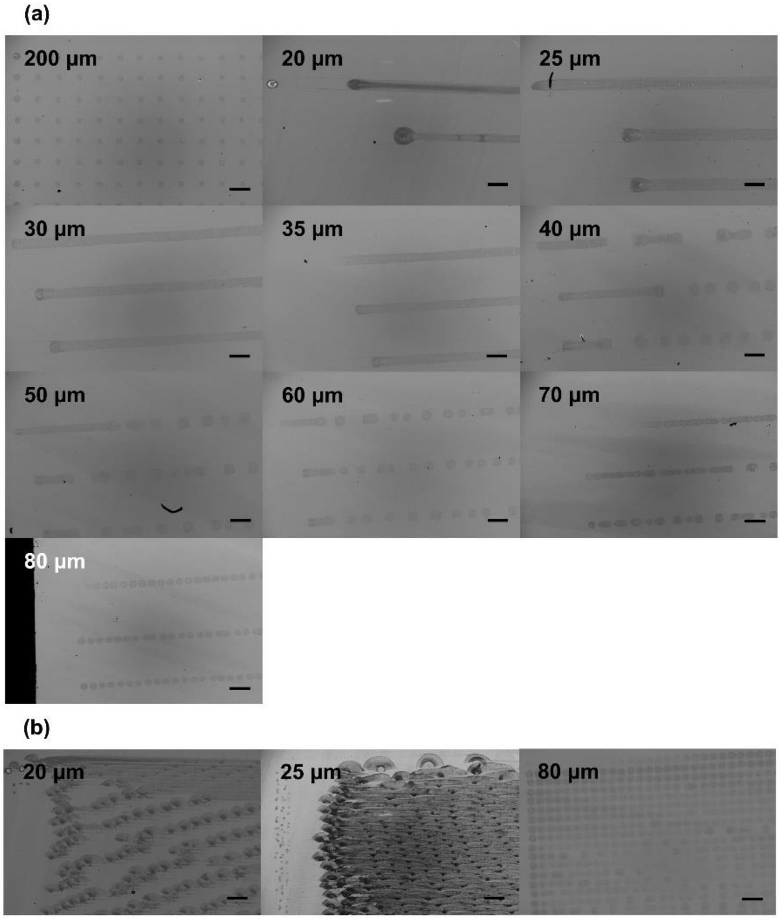

Figure 32 Optical microscope images of (a) printed dots and lines and (b) printed squares on Si wafer from Ink 1-(0.25rGO, 0.1/1EG, 0.1Tri)-1.5µm. 200 µm was used as drop spacing for dots, and different spacing from 20 to 80 µm (9 data points) was used as the drop spacing for lines. Then, 20, 25, and 80 µm were used as representative drop spacings for printed squares. The MPF was 1 kHz, and the cartridge and platen temperatures were room temperature and 60 ℃, respectively. The UV time for the Si wafer was maintained at 20 minutes. The major concern at this stage is to first find a suitable drop spacing for avoiding issues like bulges and discrete depositions. Then, the effect of drop spacing on the major drying issues was explored, especially for issues like the missing front and waviness, as their shapes changed dramatically when various drop spacings were applied. Black scale bar represents 200 µm.

The first aim of this section is to find suitable settings for avoiding issues like bulges and discrete depositions of ink, among others. Additionally, the relationship between drying issues and these two settings is discussed.

Figure 32 (a) and (b) show the printed individual dots, lines, and squares with various drop spacings on a Si wafer using Ink 1-(0.25rGO, 0.1/1EG, 0.1Tri)-1.5µm. The printer settings and substrate modifications are as follows:

(1) drop spacings are 200 µm for dots and 20 to 80 µm for lines;
(2) drop spacings for squares are 20, 25, and 80 µm, respectively;
(3) maximum printing frequency is 1 kHz;
(4) cartridge temperature is room temperature;
(5) platen temperature is 60 °C;
(6) UV Ozone time is 20 minutes.

Different drop spacings were used for printing patterns, and other settings were held constant from the initial settings.

As for printed lines in figure 32 (a), three major types of lines could be observed when the drop spacing was changed from 20 to 80 µm. When the drop spacing was between 20 and 25 µm, continuous lines with the missing front issue could be observed. The bulge issue could be found in the lines with 20 µm drop spacing. Then, when the drop spacing was between 25 and 35 µm, uniform continuous lines with the missing front issue could be seen. No bulge issue was found in these lines, and the line width decreased from 122.5 ± 1.6 µm to 103.8 ± 1.8 µm as the drop spacing increased from 25 to 35 µm. Then, when the drop spacing was between 40 and 80 µm, the lines were transformed into discrete depositions, and the missing front issue could still be observed until the drop spacing was 60 µm.

In terms of printed squares in figure 32 (b), 20, 25, and 80 µm were used as the representative drop spacings, respectively. The clear missing front, bulge, and waviness issues could be observed in squares when drop spacings were 20 and 25 µm, but they were supressed when drop spacing was 80 µm. However, no continuous square could be formed when 80 µm was used as the drop spacing.

In addition, the individual dots printed with a drop spacing of 200 µm from figure 32 (a) show that no misfiring of droplets could be observed from the printed pattern, which indicates that the missing front issue is not caused by the droplet misfiring during the printing process.

Furthermore, the size of the dots in the printed lines and squares with a drop spacing of 80 µm is much larger than that of printed dots with a drop spacing of 200 µm. In theory, the individual dots should be observed when drop spacing is larger than the dot diameter, as they are not connected[114]. So, the dot diameter with a drop spacing of 80 µm should be similar to the dot diameter with a drop spacing of 200 µm as both these drop spacings are larger than the average dot diameter, which is about 52.0 ± 2.1 µm. This indicates that the actual dot diameter might vary from the final calculated one.

Based on the above results, we found that although manipulating the drop spacing could avoid bulge and discrete deposition issues, the major drying issues still were observed in the printed patterns. However, the above results still provide some insight into the mechanisms behind these drying issues, especially the missing front and waviness issues.

As figure 32 (a) reveals, the printed lines changed from lines with bulges to continuous lines to discrete depositions when drop spacing increased from 20 to 80 µm. This trend matches the model proposed by Yang, which is the model used for predicting bulge behaviours of inkjet-printed lines with different drop spacings when no contact receding happens[158]. Bulges are the result of competition between capillary flows which spreads the droplet and the axial flow along the printing direction due to the pressure difference between the newly deposited droplet and an existing bead. Duineveld found that as the drop spacing decreases, more liquid is deposited in unit distance. Then, the volume increase created by these new droplets, in turn, increases the contact angle and causes the regional area to have a contact angle larger than the ink's advancing contact angle. Thus, the contact line moves, and a strengthened capillary flow is formed to absorb the solvent from the adjacent droplets to form a bulge[159]. So, when the drop spacing is increased, this issue can be supressed. However, when the drop spacing is continuously increased, the disconnections of droplets happen irregularly, which starts to form discrete depositions of ink. When drop spacing is larger than the dot diameter, individual dots are seen.

Regarding the issue that the sizes of dots in printed lines with a drop spacing of 80 µm are much larger than those of dots with a drop spacing of 200 µm (Figure 32 (a)). In theory, the dots with a drop spacing of 80 µm should have a similar size to the dots with a drop spacing of 200 µm, as the average dot diameter is about 52 µm. Thus, the dots with a drop spacing of 80 µm should be individual dots as well. However, the discrete deposition of ink indicates that they are connected together rather than individual dots, even at such large drop spacing. So, the actual size of the dots is larger than the size observed from the dots printed with a drop spacing of 200 µm. Derby et al. found that the droplet can be turned into an elliptical shape when the droplet has a low contact angle with the substrate, enabling the dot to spread and connect with another droplet even when the drop spacing is larger than its diameter[128]. He believes this change of shape is due to changes in the local surface energy caused by changes in vapour transport in the region. Although this phenomenon could explain why the dots connect despite a relatively large drop spacing, this change of shape still could not explain why the waviness happened in the printed squares (drop spacing = 25 µm), while the lines printed with the same drop spacing are straight. Instead, literature report by Tao, Z., et al. provides another view on the waviness issue[160]. The ink used in their project is a silver-based ink with PVP polymer as the stabiliser, which is different from the ink used in our project. The separation phase of the solvent took place during the droplet drying. The typical structure of their dried dots consisted of a polymer-rich outer region and a particle-rich inner zone. In other words, a dual-ring structure of the dried droplets was formed in this case. In order to produce continuous lines for the silver region, a small drop spacing was always used to print the patterns. Additionally, the squares printed in Tao's project exhibit the waviness issue, and the individual lines printed in his project also show no wavy edge when the same drop spacing has been applied to squares. For Ink 1-(0.25rGO, 0.1/1EG, 0.1Tri)-1.5µm, which contains modifiers like Triton and EG, the Marangoni effect would be formed during the drying process. Thus, the formation of a dual-ring structure could also lead to a concentrated dot/disk in the centre. Therefore, the actual dot diameter could be larger than the diameter of the centre dot/disk. This could explain why the droplets are still connected despite a drop spacing of 80 µm. At the same time, this could also explain why the uniform line could be printed using a drop spacing of 25 µm, while the square printed with the same drop spacing exhibits the waviness issue. Since the drop spacing set in the project is based on the final dried dot, which is supposed to be smaller than the outer ring's diameter, the bulge issue of the outer ring may be formed in the printed lines and squares. Then, the bulge issue will affect the shape of the line printed next to it. Thus, the waviness issue could be observed in the square, while the straight individual line could be printed with the same drop spacing. Thus, the origin of the waviness issue could be explained.

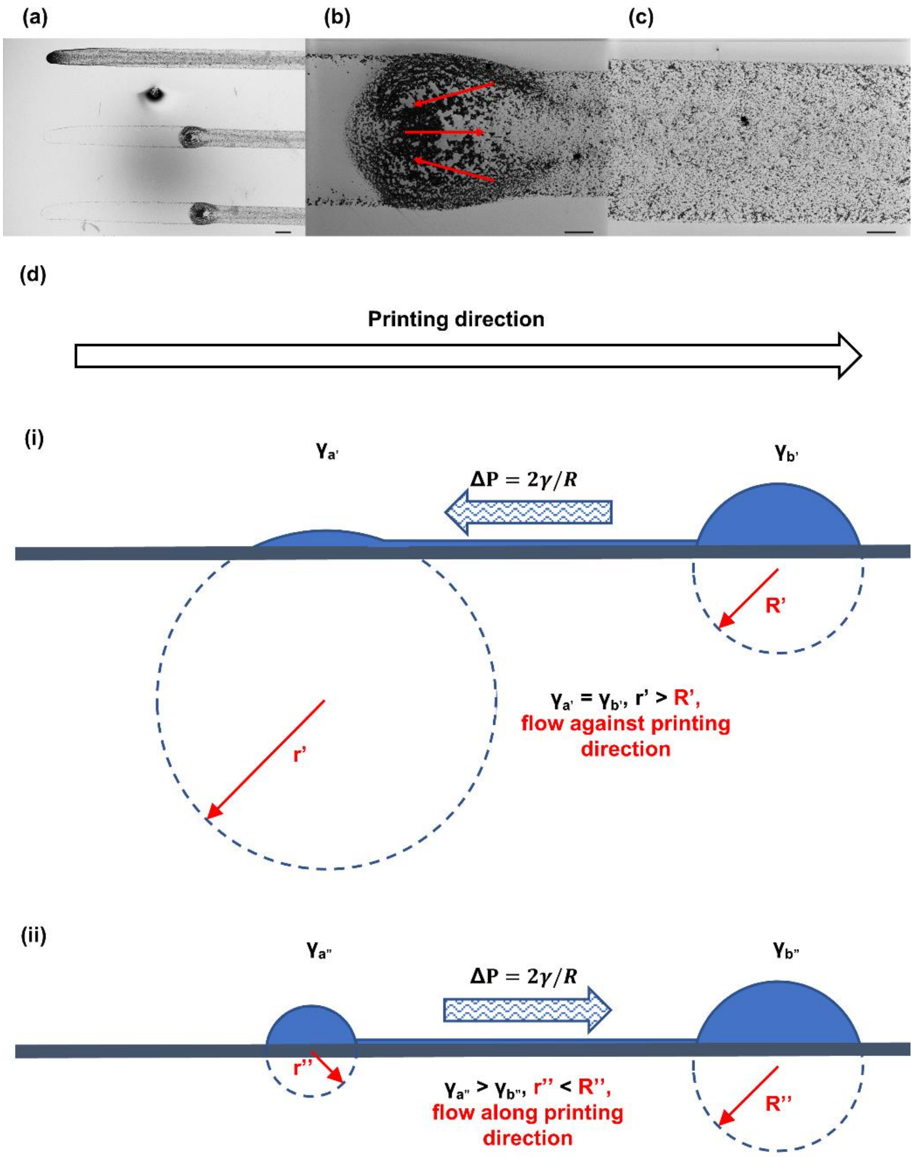

Figure 33 SEM images of the printed lines from Ink 1-(0.25rGO, 0.1/1EG, 0.1Tri)-1.5µm with a drop spacing of 25 µm. The cartridge and platen temperatures are room temperature and 60 ºC, respectively. The MPF is 1 kHz; the UV time is 20 minutes. (a) and (b) are the magnified missing front zone and concentrated dot area in the printed line; (c) is the magnified main body of the printed line after the concentrated dot area; and (d-i), (d-ii) illustrate the mechanisms of formed internal flows with different directions due to the Laplace pressure. The area with a higher Laplace pressure could form a flow to the area with a lower Laplace pressure[161]. In general, if the curvature radius of a newly landed droplet is smaller than that of the liquid bead, then the droplet could have a higher Laplace pressure and could form an internal flow against the printing direction[162] (d-i). However, the first dot issue could lead to an increase in droplet surface tension or a decrease in droplet diameter, which also increases the Laplace pressure[163]. Thus, an internal flow along with the printing direction could be formed (d-ii), and it is responsible for the formation of missing front issues in the printed lines and squares. Black scale bar represents 100 µm for (a) and 20 µm for (b) and (c).

Regarding the missing front issue that appears in printed lines and squares in figure 32, no similar issue has yet been reported. The issue could be observed in both printed lines and squares until the drop spacing is larger than 60 µm. However, no continuous pattern could be obtained after such large drop spacing. The missing front issue could be slightly suppressed when the drop spacing was increased from 20 to 35 µm. The suppression effect of drop spacing on this issue is not obvious after 35 µm, however.

Figure 33 shows the SEM image of the printed lines from Ink 1-(0.25rGO, 0.1/1EG, 0.1Tri)-1.5µm with a drop spacing of 25 µm, which illustrates (a) the missing front zone, (b) the concentrated spot, (c) the main body of the printed line, and (d-i), (d-ii) the mechanisms of formed internal flows with different directions due to the Laplace pressure in the printed line. As figure 33 (b) shows, an internal flow along with the printing direction should form, and it encounters another internal flow going against the printing direction, forming a concentrated spot at the intersection.

The flow against the printing direction is a common phenomenon in inkjet printing; it is generated due to the Laplace pressure difference between a newly landed droplet and existing liquid beads[161]. Since the curvature radius of the newly landed droplet is smaller than that of the liquid bead, the droplet could have a higher Laplace pressure. An internal flow against the printing direction could be formed[162], which is depicted in figure 33 (d–i). This flow is also the main reason for the formation of a bulge in the head of a printed line. As the same issue has not yet been reported, two possible mechanisms are proposed here. One is the misfiring of jetted droplets during the printing, and the other involves the Laplace pressure induced flow along the printing direction.

The printed dots shown in figure 32 (a) reveal that there is no misfiring of the droplets when drop spacing equals 200 µm, as all the droplets were printed in position. Hence, the misfiring of droplets could be excluded.

Regarding the flow driven by the Laplace pressure, the printed liquid bead usually has the smallest pressure compared to other sections of the line that are flatter[161]. Therefore, the internal flow along the printing direction could only be formed when the Laplace pressure in the first several droplets is higher than that of a newly landed droplet. The equation for calculating the Laplace pressure is $\Delta P = 2\gamma/r$, where P is the Laplace pressure, γ is the surface tension of the droplet, and r is the curvature radius of the droplet[163]. When the surface tension has been increased, or the curvature radius has been decreased, then the Laplace pressure increases and results in a flow from the high-pressure region to the lower one. Thus, the first dot issue could be an important contributor to the missing front issue. The increased rGO loading resulted in the rise of the ink's surface tension. This is because higher graphene loading absorbs more Triton molecules in the droplet, as Trion is not only the surfactant of ink but also a stabiliser to the graphene[111]. Thus, more Triton molecules could be absorbed into graphene, and less Triton would appear in the liquid-vapour interface, so the surface tension would increase in this case. This higher surface tension could lead to a larger Laplace pressure based on the above equation. Thus, the Laplace pressure in the first dot region may increase, causing an internal flow along the printing direction to be formed, as illustrated in figure 33 (d–ii).

Figure 32 (a) shows that the missing front issue could be strengthened when drop spacing is decreased from 25 to 20 µm since the decrease of drop spacing could strengthen the bulge issue[159]. The stronger capillary flow from the bulge could absorb the ink at the front section, causing the missing front issue to become even worse in this case. Thus, both the missing front and bulge issues would become more serious in the case of smaller drop spacing.

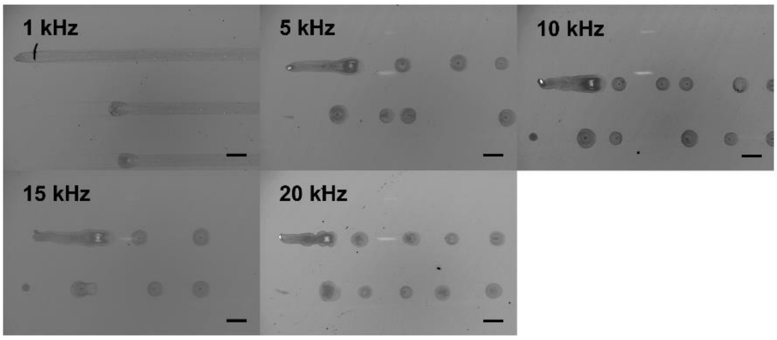

Figure 34 Optical microscope images of printed lines on Si wafer from Ink 1-(0.25rGO, 0.1/1EG, 0.1Tri)-1.5µm with different MPF. 25 µm was used as the drop spacing for all printed lines. Then, the MPF were set to 1, 5, 10, 15, and 20 kHz. The cartridge and platen temperatures were room temperature and 60 °C, respectively. The UV time for the Si wafer was maintained at 20 minutes. The major concern at this stage is to find the effect of MPF on the drying issues. As a result, the dried discrete larger spots also confirm the formation of a dual-ring structure in the final dried dots, which is a critical factor causing the waviness issue. In addition, dried discrete larger spots also prove that the ink is absorbed into bulges when the bulge issue is too strong. Black scale bar represents 200 µm.

As for the effect of maximum printing frequency, it is important to know that the printhead used in this project can only provide a range from 1 to 20 kHz[92]. Figure 34 shows the lines printed on a Si wafer from Ink 1-(0.25rGO, 0.1/1EG, 0.1Tri)-1.5μm with various maximum printing frequencies. The printer settings and substrate treatments are as follows:

(1) drop spacing: 25 μm;
(2) maximum printing frequency: 1 – 20 kHz;
(3) cartridge temperature: room temperature;
(4) platen temperature: 60 °C;
(5) UV Ozone: 20 minutes.

Five different MPF have been used, while other settings remained the same from the initial conditions.

As figure 34 shows, the continuous lines could only be observed when MPF was 1 kHz with a drop spacing of 25 μm. The lines with higher printing frequencies have been transformed into a series of discrete larger spots. As Duineveld proposed, the increase in MPF could increase the amount of ink deposited in the unit time, so the volume of printed dots could be suddenly expanded, resulting in an increase in the contact angle, which is similar to the effect of using small drop spacing[159]. When the contact angle is larger than the advancing contact angle of the ink, the contact line moves, and a strengthened capillary flow absorbs the ink from adjacent droplets to form bulges. This result proves that 1 kHz is the most suitable option for Ink 1-(0.25rGO, 0.1/1EG, 0.1Tri)-1.5μm. In addition, there are clearly multi-ring structures and concentrated centre dots in these discrete large spots. Thus, these structures could also prove the assumption presented in the previous section that the dual-ring structure due to the Marangoni effect transpired during the ink drying.

Overall, this section reviewed the effect that specifically drop spacing and MPF have on common and unique drying issues that are important to resolve. The bulge and discrete deposition of ink could be avoided by using suitable drop spacing and MPF. However, these adjustments could not effectively suppress all drying issues. The reasons for missing front and waviness issues have also been explained in this section. The waviness issue could be mainly caused by the dual-ring structure of the dried dot caused by the Marangoni effect. Since the drop spacing is usually set as the radius of the dried dot – which is smaller than that of outer ring – to form a continuous line, the bulge issue happens in the outer ring. The printed lines in the square are affected by the structure of the outer ring, and the waviness issue is formed. In addition, the larger drop spacing could not suppress this issue, as forming a continuous rGO line is also necessary for printing, and no continuous line could be formed when the drop spacing is too large. The missing front issue could be mainly caused by the Laplace pressure difference between different sections in the printed line. As the first dot issue is inevitable, the increased rGO loading in the first several droplets results in an increase in the surface tension of the region. Therefore, a higher Laplace pressure would create an internal flow along with the printing direction and cause the missing front issue.

Finally, the suggested drop spacing and MPF for further exploration are 25 µm and 1 kHz, respectively.

4.3.2 Effect of cartridge and platen temperatures on suppression of drying issues

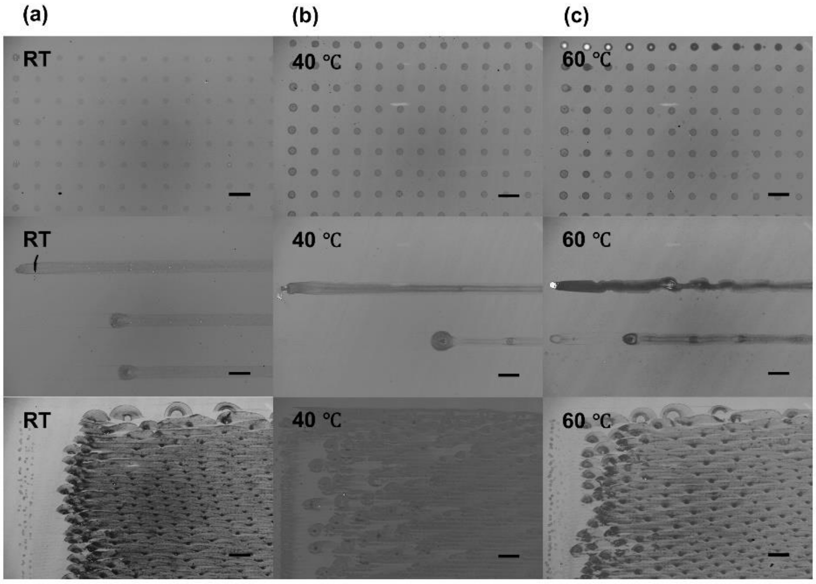

Figure 35 Optical microscope images of printed dots, lines, and squares on a Si wafer from Ink 1-(0.25rGO, 0.1/1EG, 0.1Tri)-1.5µm under different cartridge temperatures, including (a) printed patterns under room temperature; (b) printed patterns under 40 ℃; and (c) printed patterns under 60 ℃. 200 µm was used for the drop spacing for printing individual dots, while 25 µm was used for the drop spacing of lines and squares. The MPF was 1 kHz, and the platen temperature was 60 ℃. The UV time for the Si wafer was maintained at 20 minutes. The major concern at this stage is to find the effect of cartridge temperature on the drying issues. The increase in cartridge temperature leads to a more serious first dot issue due to the quickened evaporation rate around the nozzle. Similarly, the missing front issue became worse when the cartridge temperature increased from room temperature to 40 ℃, but the trend stopped when the cartridge temperature further increased to 60 ℃ due to the shortened droplet drying time on the substrate at such high cartridge temperatures. Finally, although the evaporation rate of the droplet could be strengthened by this increased cartridge temperature, the CRE and waviness issues were not obviously affected. This indicates that the Marangoni effect still dominates droplet drying. Black scale bar represents 200 µm.

Figure 35 shows the patterns printed on Si wafer from Ink 1-(0.25rGO, 0.1/1EG, 0.1Tri)-1.5µm with various cartridge temperatures. The printer settings and substrate treatments are as follows:

(1) drop spacing: 200 µm for dots and 25 µm for lines and squares;
(2) maximum printing frequency: 1 kHz;
(3) cartridge temperature: room temperature to 60 °C;
(4) platen temperature: 60 °C;
(5) UV Ozone: 20 minutes.

Varying cartridge temperatures (room temperature, 40, and 60 ℃) were used for printing patterns, and other settings were kept the same as the initial conditions so that the effect of cartridge temperature on pattern drying could be explored. The maximum cartridge temperature in the Dimatix-2831 printer is 60 °C[92].

As the cartridge temperature increased, the average dot diameter too increased from 52.0 ± 2.1 µm to 65.9 ± 1.4 µm. Consequently, the first dot loading issue became more serious in the printed dots and lines when the cartridge temperature was raised from room temperature to 60 °C. However, the same trend for the first dot issue could not be found in printed squares due to the missing front issue.

The missing front issue became more serious in all printed patterns when the cartridge temperature increased from room temperature to 40 °C, but the situation did not worsen when the temperature was further increased to 60 °C.

Regarding the CRE and waviness issue, no obvious effect of cartridge temperature was found based on the printed patterns.

The increase in cartridge temperature could lead to a decrease in droplet viscosity and an acceleration of ink drying around the nozzle[36]. The reason for the increased dot diameter could be explained by the decreased viscosity of the droplet. Therefore, smaller viscous dispassion is obtained during the spreading of the droplet. Then, an increase in the cartridge temperature has a similar effect to decreasing drop spacing, as the drop spacing was fixed at 25 µm at this stage.

As mentioned before, the first dot issue is the main source of the missing front issue, as more dried rGO flakes are added in the first several droplets and result in an increase of surface tension of these droplets. The higher cartridge temperature results in a faster evaporation of ink around the nozzle[36], so the first dot issue can become more serious in this case. The printed individual dots from figure 35 prove this trend. The missing front issue was theoretically to become more serious as the cartridge temperature raised. However, that trend was only observed when temperature increased from room temperature to 40 ℃ and did not worsen when cartridge temperature reached 60 ℃. This could be explained by the shortened lifetime of a droplet due to the higher applied temperature. Since the platen temperature was set at 60 ℃, the droplets jetted with the cartridge temperature below this point underwent a heating process to reach the maximum evaporation rate, while the droplets at 60 ℃ did not need such a process. Thus, the lifetime of this type of droplet would be shorter than the others. So, although the missing front issue should theoretically be more serious when the cartridge temperature is

60 °C, this shortened droplet lifetime potentially supresses this issue as the flow may not have time to push rGO flakes any further before the droplet dries. Notably, the CRE and waviness issues have not been affected by the increased cartridge temperature. The first dot issue and the shortened lifetime of the droplets proved that the evaporation rate of the droplets was increased. However, no clear coffee-ring structure could be seen in the printed dots, and the waviness issue was not influenced either. Thus, the possible explanation is that the Marangoni effect still dominated the drying process for the current ink formulation. The Marangoni effect is a major method to supress the CRE in this project. It can be induced by heating substrate, adding surfactant, or using co-solvents[131]. The origin of this flow is the surface tension gradient formed from the contact line to the apex of the droplet. However, the impact of the thermally induced Marangoni effect is usually neglected when the surfactant or co-solvents induced Marangoni effect are present in the same droplet, as the latter two are much stronger than the former one[134]. Since Triton and Ethylene glycol (EG) are used in this project, the effect of the thermal Marangoni effect induced by substrate heating is neglected. Thus, the main competition is between CRE, and surfactant and co-solvents induced Marangoni effects. Plus, the addition of modifiers is an effective way to modulate the drying uniformity and printability of the ink at the same time[13]. In terms of the surfactant and co-solvents induced Marangoni effects, they are strongly related to the evaporation rate in the contact line area. The surfactant induced Marangoni effect is caused by the accumulation of surfactants in the contact line area due to the capillary flow from CRE[134]. So, more surfactants are transported into the contact line area, which results in reduced surface tension at that region. Then, a decreasing surface tension gradient is formed from the apex to the contact line, and the corresponding Marangoni flow is produced. The mechanism for co-solvents induced Marangoni effect is slightly different from the above. The evaporation rate in the contact line area is the highest among the other regions in the droplet, so when two solvents have different vapour pressures and surface tensions, a surface tension gradient is formed when the volatile solvent has a higher surface tension[134]. The local surface tension drops when a more volatile solvent has evaporated. Thus, the evaporation rate at the contact line affects both the strengths of surfactant-induced and co-solvents-induced Marangoni effects. So, when the cartridge temperature increased, the evaporation rate increased, and

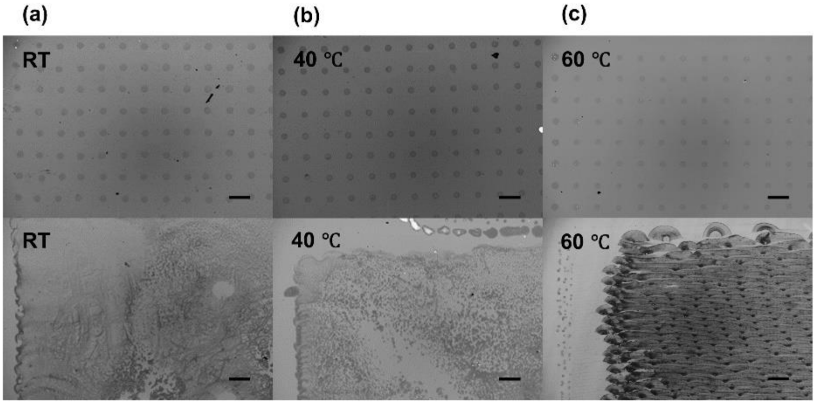

Figure 36 Optical microscope images of printed dots and squares on a Si wafer from Ink 1-(0.25rGO, 0.1/1EG, 0.1Tri)-1.5μm under different platen temperatures, including (a) printed patterns under room temperature; (b) printed patterns under 40 °C; and (c) printed patterns under 60 °C. 200 μm was used for the drop spacing for printing the individual dots, while 25 μm was used for the drop spacing of squares. The MPF was 1 kHz, and the cartridge temperature was room temperature. The UV time for the Si wafer was maintained at 20 minutes. The major concern at this stage is finding the effect of platen temperature on drying issues. The decrease in platen temperature raised another unexpected drying issue in the printed square, wherein the flakes were transported to the bottom and formed a concentrated bottom due to the Marangoni flow. This flow is caused by the low vapour pressure nature of EG: the DI water in the printed square evaporates faster than the EG, and as the drying continues, more DI is left in the bottom area, resulting in a high surface tension area that leads to the formation of a Marangoni flow in the square. Black scale bar represents 200 μm.

CRE should also be strengthened. Simultaneously, more surfactants accumulate in the contact line area, and more DI water is consumed in this area as well due to the strengthened CRE. Thus, both surfactant-induced and co-solvents-induced Marangoni effects would become stronger as well. So, the Marangoni effect could still dominate the droplet drying and form dual-ring structures.

In all, increasing cartridge temperature mainly causes more serious first front issues and increases the dot diameter. Although it could accelerate the evaporation rate, the Marangoni effects change with this increased cartridge temperature simultaneously. Thus, its effects on CRE and waviness issues are not obvious.

Figure 36 shows the patterns printed on a Si wafer from Ink 1-(0.25rGO, 0.1/1EG, 0.1Tri)-1.5μm with various platen temperatures. The printer settings and substrate treatments are as follows:

(1) drop spacing: 200 μm for dots and 25 μm for lines and squares;
(2) maximum printing frequency: 1 kHz;
(3) cartridge temperature: room temperature;
(4) platen temperature: room temperature to 60 °C;

(5) UV Ozone: 20 minutes.

Different platen temperatures (room temperature, 40, and 60℃) were used for printing patterns, while the other settings were kept the same as the initial conditions so that the effect of platen temperature on pattern drying could be explored. The maximum platen temperature in the Dimatix-2831 printer is 60 °C, as well[92].

The average dot diameter was decreased from 67.3 ± 1.4 μm to 52.0 ± 2.1 μm as the platen temperature raised from room temperature to 60 °C. The typical waviness issue in the square could only be observed when the temperature was 60 °C; squares printed below this temperature did not form uniform squares. These squares have large empty areas, and the flakes in these areas have been transported to the base, which results in a concentrated bottom in the printed squares.

The decreased dot diameter could be explained by the accelerated evaporation rate due to the higher platen temperature. Lim et al. found that a large volume loss of volatile solvent with a smaller viscosity in a binary system results in a sudden increase in droplet viscosity[164]. This project uses an EG/DI system, in which DI water has a higher vapour pressure and lower viscosity compared to that of EG[142]. Although the ink formulation did not change as to the samples in figure 36, the increased platen temperature increased the evaporation rate of the ink. With the sudden increase of droplet viscosity that occurred when the platen temperature reached 60 ℃, a smaller dot diameter could be observed.

As for the drying issue in the printed square, a lower platen temperature would result in a slower evaporation of both EG and DI water, leaving more DI solvent in the printed squares. As the drying continues, the top part of the thin film quickly dries, and the amount of solvents in this part become less compared to that of the newly printed part. Thus, a typical premise of co-solvents induced Marangoni effect has been formed in this case[134]. Assuming the thin film as a whole, there is less DI water in the top region due to the longer evaporation time, which results in a smaller surface tension compared to that of the bottom region. Hence, a Marangoni flow is created from the contact line to the apex due to the surface tension gradient. rGO flakes would be transported to the bottom by the flow, resulting in a concentrated bottom. It is necessary to clarify that the missing front issue could still happen. However, since most of the flakes have been transported to the bottom of the printed square due to the Marangoni effect, it is difficult to tell whether the Marangoni or Laplace pressure-driven flow dominates the transport of the flakes, especially at the front sections of the printed squares. In all, 60 °C for platen temperatures is necessary for printing squares. The drying issues, however, have not been suppressed via the temperature settings yet.

4.3.3 Effects of UV time on suppression of drying issues

Figure 37 shows the patterns printed on a Si wafer from Ink 1-(0.25rGO, 0.1/1EG, 0.1Tri)-1.5µm with various UV Ozone times. The printer settings and substrate treatments are as follows:

(1) drop spacing: 200 µm for dots and 25 µm for lines and squares;
(2) maximum printing frequency: 1 kHz;
(3) cartridge temperature: room temperature;
(4) platen temperature: 60 °C;
(5) UV Ozone: 0 to 90 minutes.

Four different UV times (0, 5, 20, and 90 minutes, respectively) were used for printing patterns, and other settings were held constant so that the effect of UV time on the drying of Ink 1-(0.25rGO, 0.1/1EG, 0.1Tri)-1.5µm could be studied.

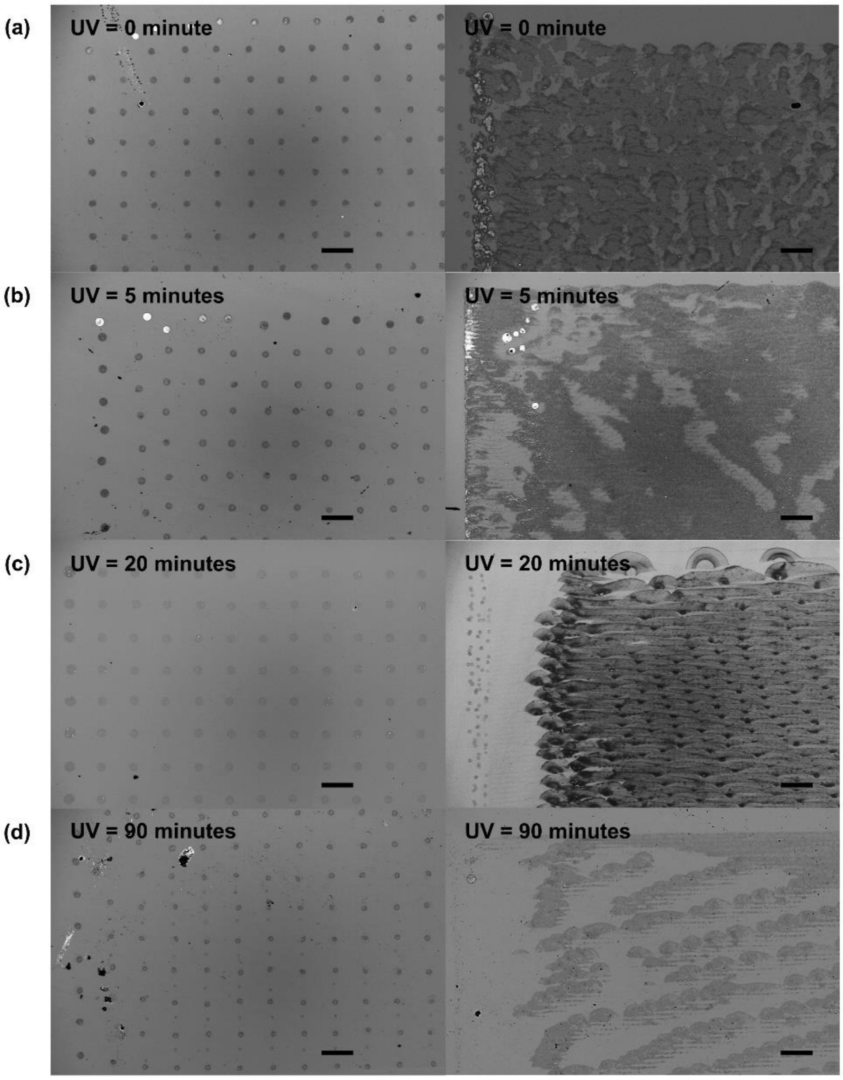

Figure 37 Optical microscope images of printed dots and squares on a Si wafer from Ink 1-(0.25rGO, 0.1/1EG, 0.1Tri)-1.5µm under different UV times, including (a) printed patterns with 0-min UV; (b) printed patterns with 5-mins UV; (c) printed patterns with 20-mins UV; and (d) printed patterns with 90-mins UV. 200 µm was used for the drop spacing for printing the individual dots, while 25 µm was used for drop spacing of squares. The MPF was 1 kHz, and the cartridge and platen temperatures were room temperature and 60℃, respectively. The major concern at this stage is finding the effect of UV time on the drying issues. The increase in UV time made the substrate more hydrophilic, so the droplet diameter was increased. 25 µm was set as the drop spacing for all printed squares, which is a relatively larger drop spacing for samples using 0- and 5-minutes UV and a smaller drop spacing for samples using 90-minutes UV. The bulge and missing front issues became more serious in the printed square using 90-minutes UV but became supressed in the cases of 0- and 5-minutes UV. In addition, the evaporation rate at the contact line area could be manipulated by applying different UV times, as it changes the contact angle of the droplet as well as the heat conduction from the substrate to the apex of the droplet[165,166]. Black scale bar represents 200 µm.

The average dot diameters for samples using 0- and 5-minutes UV are 42.5 ± 1.9 µm and 45.4 ± 1.3 µm, respectively. By contrast, the dot diameter for samples from 20- and 90-minutes UV are 52.0 ± 2.1 µm and 50.4 ± 2.6 µm, respectively. The dots from 0-, 5-, and 90-minutes show clear dual structures, while the dots from 20 minutes exhibit the best uniformity with no obvious dual-ring structure. As previously mentioned, the measured dot diameter is smaller than the actual dot diameter, so the decrease of dot diameter in samples from 20-minutes UV to 90-minutes UV could be explained by a strengthened Marangoni flow, which transported more flakes back to the droplet centre. In addition, the positions of these centre dots are randomly distributed within the dual-ring structure in the samples using 0-, 5-, and 90-minutes UV, which is a common phenomenon produced by the Marangoni effect[134].

As for the printed squares, the drop spacing was set as 25 µm for consistency. This was a relatively large drop spacing for printed squares using 0- and 5-minutes UV and a relatively small drop spacing for printed squares using 90-minutes UV.

The first dot issue could be observed in all printed squares, though it was slightly supressed in the 90-minutes UV sample. Clear examples of the missing front issue could be found for samples using 20- and 90-minutes UV, and a clear bulge issue could be seen in the case of 90-minutes UV.

In all, the change in UV time does not obviously affect the suppression of drying issues. However, the above results still provide valuable insights into improving the drying uniformity of printed patterns.

First, the difference among the printed squares under different UV times must be explained. The printed squares from 0- and 5-minutes UV have further confirmed the effect of large drop spacing. Based on the discussion on the effect of drop spacing, the missing front issue could be caused by an imbalanced Laplace pressure between the first several droplets and the main liquid bead. When drop spacing is small, the bulge issue worsens the missing front issue, as ink in the front section is absorbed by the capillary flow from the bulge[159].

In this section, the printed squares undergoing 0- and 5-minutes UV have smaller average dot diameters compared to those of printed squares from 20- and 90-minutes UV despite the drop spacing being held constant for all printed squares. Thus, the increased drop spacing was applied for the printed squares from 0- and 5-minutes UV. The contribution of the bulge issue to the missing front is weakened, and this could explain why the missing front issue can be supressed in these two cases.

In addition, the waviness issue could also be suppressed when the drop spacing was increased, as the bulge issue usually happens in small drop spacing[114]. This explains why the missing front and waviness issues have been supressed in the cases of 0- and 5-minutes UV. However, the cost of these suppressions is the discrete depositions of ink due to the large drop spacing. For a similar reason, the suppression of the first dot issue in the case of 90-minutes UV could be explained as the effect of small drop spacing. The small drop spacing could lead to a strengthened bulge issue[114], wherein the flakes in the first dot could be transported into the bulge due to the increased capillary flow there. However, the bulge issue is a serious one for the drying uniformity of printed patterns and definitely needs to be avoided.

The main effect of UV time is to change the hydrophobicity of the substrate so that the contact angle of the deposited droplet is modulated[36]. As the UV time increases, the substrate becomes more hydrophilic, and the contact angle decreases continuously[130]. Assume that the volume conservation of droplets before and after the deposition is such that the dot diameter continuously increases as the contact angle decreases. Then, the heat conduction from the substrate to the apex of a droplet would be accelerated, which results in an increase in the evaporation rate of the droplet[165,166]. Thus, the drying uniformity of droplets could be manipulated by changing the UV time since it affects the evaporation rate at the contact line area as well. When the UV time is less, the contact angle is high, and the thermal conduction is limited, so the evaporation rate at the contact line area is supressed. Thus, both the accumulation of surfactant and the evaporation of co-solvents are not accelerated. The CRE, surfactant-induced, and co-solvents induced Marangoni effects are all supressed. A similar mechanism could be applied to the case with longer UV time treatment. The contact angle could be reduced due to the longer UV time, which results in increased heat conduction from the substrate. Thus, the evaporation rate is increased, and both the accumulation of surfactant and the evaporation of co-solvents are accelerated. So, the CRE, surfactant-induced, and co-solvents induced Marangoni effects could all be strengthened.

Although the change of UV time could affect the evaporation rate in the contact line area, its effect on the competition between CRE and surfactant-induced and co-solvents induced Marangoni effects is hard to distinguish as they could all be changed simultaneously. However, based on the dried dots, the Marangoni effect still dominates the drying process in all different UV times, as the dual-ring structure happened to all samples.

As for the printed dots, the random distribution of centre dots is a minor issue compared to the formation of the dual-ring structure. Although much literature mentioned this random distribution, they did not do further exploration on it, as they consider the formation of a dual-ring structure a successful suppression of CRE[134]. However, the dual-ring structure is hypothesised as the critical reason behind the waviness issue in printing squares for this project. Thus, a balanced competition needs to be found between the CRE and Marangoni effect to form a single uniform dot. Then, the ideal lines and squares can be printed.

In conclusion, the reasons causing the missing front and waviness issues are explained in this section. The first dot issues and the formation of a dual-ring structure are believed to play vital roles in these two unique issues.

Drop spacing and MPF can be used to avoid issues like bulges and discrete depositions of ink. Notably, a smaller drop spacing may worsen the missing front issue.

The cartridge and platen temperatures are effective tools in modulating the evaporation rate of deposited droplets. As for the cartridge temperature, the first dot issue worsens when the cartridge temperature increases, but the trend stops when the cartridge temperature is further increased, as the lifetime of deposited ink is shortened. Relatedly, the increase in cartridge temperature can continuously increase the dot diameter due to the reduced ink viscosity. In addition, the exploration of the cartridge temperature also found that the CRE and Marangoni effects can be tuned simultaneously. Thus, issues like a dual-ring structure could not be modulated by this method. Regarding the platen temperature, lower platen temperature produces very serious drying issues, as the printed squares were drying as a thin film as a whole rather than in individual lines. A Marangoni effect likely brings the flakes transported to the bottom part of the square, and no uniform pattern could be obtained.

Then, the exploration of UV time confirmed that the CRE and Marangoni effects could be modulated simultaneously. The modulation of the evaporation rate via a change in the contact angle could not suppress the formation of the dual-ring structure either. Therefore, a balance between the CRE and Marangoni effect still must be found, and further exploration of the ideal ink formulation is needed. However, a suggested series of printer settings and modifications are still concluded and can be used as a reference point for future modified ink printing. The details of the suggested printer settings and substrate treatments are as follows:

1. drop spacing = 200 μm for dots and 25 μm for lines and squares on Si wafer;
2. maximum printing frequency = 1 kHz;
3. cartridge and platen temperatures = room temperature and 60 °C, respectively;
4. UV time = 20 minutes.

4.4 Exploration on droplet drying uniformity via ink formulation, printer setting, and substrate modification

Two critical issues have been found in the previous section. One is the serious first dot issue; the other is the ME dominated drying process. The former causes the missing front issue, and the latter leads to the waviness issue due to the dual-ring structure of printed droplets. The first dot issue can be controlled by using regular cleaning cycles and setting an extra filtration process[92]. As for the waviness issue, the previous exploration found that printer settings and substrate modifications have limited effects on its suppression. Thus, further exploration of finding the balance between CRE and ME via ink formulation is the focus of this section.

This exploration concentrates on the drying of sessile droplets rather than the printing of formulated inks. The printability challenges of formulated inks and the high cost of the printhead are the main reasons for investigating in this way. There are numerous factors affecting the drying of a sessile droplet, such as droplet drying mode (constant contact angle mode, constant contact radius mode, or a mix of the two), solute concentration, shape, size, and material interactions with other interfaces (interactions from particles to particles, particles to substrates, and particles to liquid). Then, the atmospheric conditions like relative humidity and ambient temperature and pressure also show their effects on droplet drying[134]. Apart from those factors, the substrate effects (wettability and temperature) and fluid composition (surfactant and thickener) also play critical roles during droplet drying[167].

However, the effects of fluid composition, especially the loadings of used surfactant and thickener (co-solvents), are the major focus of this section, as they are the main components of modifiers used in this project. The inclusion of a modifier could not only adjust the rheological properties of ink but also induce the Marangoni flow at the same time. Thus, it is an effective way to modulate the printability and drying uniformity of prepared ink spontaneously. However, there is a huge volume difference between the droplet printed from the DMP-2831 printer (~10 pL) and the droplet used on this drying exploration (~1 µL). Nonetheless, it was reported that microliter droplets could have similar or even identical drying processes compared to picolitre droplets[160]. Additionally, instead of exploring the specific formulation that can balance the CRE and Marangoni effects, the trends in droplet drying in response to changes in the fluid composition are the focus of this exploration. Plus, phenomena like contact line receding can be directly observed from the drying of 1 µl droplet. Finally, this section concludes with a guide on formulating inks with ideal drying uniformity based on the previous printable inks.

In this section, the formulation of ‘0.1rGO, 0.01/1EG, 0.2Tri’ has been used as the starting point of the formulation. The reasons for selecting this base ink are as follows:

(1) 0.1 mg/ml rGO, easy to observe the dried patterns;
(2) 0.01/1 EG, the co-solvents induced Marangoni effect (C-ME) exists, but the strength is limited;
(3) 0.2 mg/ml Triton, the surfactant-induced Marangoni effect (S-ME) exists, but the strength is limited;
(4) 25 °C platen temperature, avoids the change in evaporation rate;
(5) 0-minute UV time, avoids the change in evaporation rate.

Since the use of modifiers in this project is to tune the printability of the ink and the droplet drying uniformity at the same time, both C-ME and S-ME have been kept in this baseline ink, as the majority of formulated inks in this project would have these two effects spontaneously. Then, two major steps were taken to satisfy this exploration based on this origin point. One explores the drying uniformity of sessile droplets by changing the individual factors, and the other investigates the effects of modifiers on the droplet drying uniformity. Additionally, the investigation of the effects of rGO loading, UV time, and platen temperature on the modifiers' effects has also been contacted.

4.4.1 Effects of individual factors on droplet drying uniformity

As mentioned before, factors like droplet drying mode, properties of solutes, atmospheric conditions, substrate effects, and fluid composition could all affect the drying of a sessile droplet[134,167]. However, the exploration of all these factors is not the focus of this step. The main concern of this step is to find the effects of different loadings of surfactant (Triton X-100) and thickener/co-solvent (Ethylene glycol) on droplet drying. Triton X-100 and ethylene glycol are the main components used for preparing the modifier for this project. Since the inks in this project were prepared by mixing 'final rGO dispersions' with corresponding modifiers, the rGO loading is the remaining factor that determines the ink composition. UV time and platen temperature are the tools used to modify the substrate. Thus, their effects on droplet drying are also important to know. In this section, the exploration is conducted by changing the individual factors. However, each new formulation and corresponding UV time and platen temperature in this section are designed based on the best result from the previous step; the base ink (0.1rGO, 0.01/1EG, 0.2Tri) is used as the starting point.

The droplet drying mode can be directly observed from the drying process of 1 µl of droplet. The CCD mode was the drying mode for all droplets deposited in this project. Then, the atmospheric conditions (ambient conditions) and solute shape (2D flakes) and size (~1.5 µm, average flake size) were all held constant to minimise their effects on the droplet drying. As for the interactions among particles to other interfaces, while the same type of rGO flakes has been used throughout the experiment, its interactions with the other interfaces could be affected by the used surfactant[168]. The corresponding details will be discussed in the surfactant section.

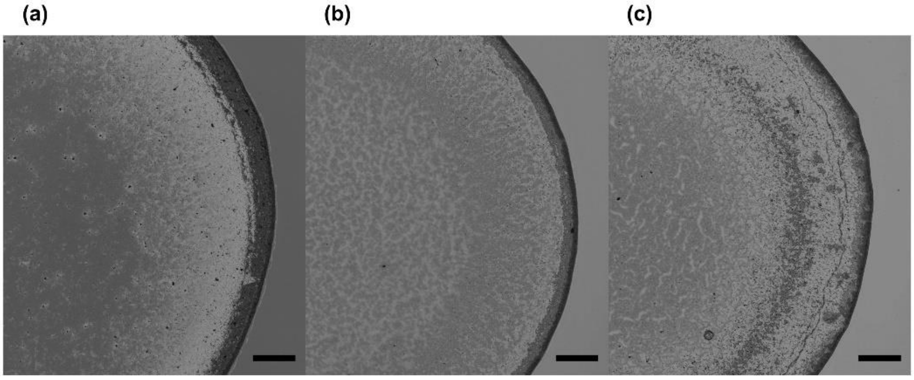

Figure 38 Optical microscope images of dried dots from ink ‘0.1rGO, 0.01/1EG, 0.2 – 0.06Tri’ with different Triton loadings ((a) for 0.2Tri; (b) for 0.1Tri; and (c) for 0.06Tri). The effects of Triton loading on droplet drying are the major concern at this stage. The UV time is 0 minutes, and the platen temperature is room temperature. The dot diameter continuously decreased when Triton loading dropped from 0.2 to 0.06 mg/ml. Simultaneously, the CRE was also supressed when less Triton was used. The decreased Triton loading results in a strengthened Marangoni effect to compete with CRE, as it would take a longer duration to reach the CMC during the drying. Black scale bar represents 200 µm.

In order to test the effect of Triton X-100 loading on the drying of sessile droplets, the experiment was conducted in the following way:

(1) a 1 µl droplet from ink ‘0.1rGO, 0.01/1EG, 0.2Tri’ was gently deposited on a Si wafer treated with 0-minute UV and dried at room temperature;
(2) the other two droplets from inks with different Triton X-100 loadings (0.1 and 0.06 mg/ml) have also been deposited on the Si wafer following the same process;
(3) the EG (0.01/1) and rGO (0.1 mg/ml) loadings were kept the same in all three droplets, and the UV time (0 minutes) and platen temperature (room temperature) were also not changed. The only difference among these three 1 µl droplets was the Triton loading.

The optical microscope images of the corresponding dried dots are shown in figure 38. The dried dots have been labelled as (a), (b), and (c), which come from inks of 0.1rGO, 0.01/1EG, ‘0.2 – 0.06’Tri, and dry on the Si wafer treated with 0-minute UV at room temperature. It is worth mentioning that the sizes of the dried dots are quite large, so the full dots could not be captured even with the minimum magnification of the microscope (similar occasions happened throughout this part of the investigation).

	0.2 mg/ml Triton	0.1 mg/ml Triton	0.06 mg/ml Triton
W (µm)	86.22 ± 3.72	54.08 ± 3.18	53.06 ± 4.32
R (µm)	1.78×10^{3} ± 12.54	1.35×10^{3} ± 18.79	1.34×10^{3} ± 18.89
W/R	0.05	0.04	0.04

Table 12 Values of W, R, and their ratio of dried dots from the formulations with different Triton loadings. The diameters and W/R ratios of these three dots were decreased when less Triton was used in the ink.

These three images were taken under the same magnification, and their sizes were supposed to be different as various loadings of Triton X-100 were used.

The average width of the ring stains and the average radius of the dots have been referred to as W and R, respectively. Since the dried dots are not perfect circles, at least 20 data points for each dot were collected for the calculation of W and R. The W/R ratio has been collected as a reference number to evaluate the drying uniformity of the dried dot. A larger W/R ratio indicates a wider ring width compared to the radius of the dried dot. The values of W, R, and their ratio of these three dots are presented in table 12.

As figure 38 shows, the dot radius decreases from ~1.78×10^{3} µm to ~1.35×10^{3} µm, and the W/R ratio changes from 0.05 to 0.04 when the Triton loading increases from 0.2 to 0.06 mg/ml. Although the dots with 0.1 and 0.06 mg/ml Triton have same W/R ratios, more rGO flakes could be observed in the interior area of the dot with 0.06 mg/ml Triton. Thus, the CRE was continuously supressed when Triton was changed from 0.2 to 0.06 mg/ml.

Triton is a non-ionic surfactant often used in the preparation of graphene-based functional ink[84]. The mechanism behind the increased dot diameter when more Triton has been used is due to the adsorption of surfactant at solid-vapour interface on a hydrophobic substrate (0-minute UV on Si wafer), so the wettability of the contact area beyond the contact line could be altered into a hydrophilic form, and the wetting area could become larger[168]. As for the hydrophilic substrate, since the main solvent of the ink in this project is water, the spreading of the droplet on the substrate would be further strengthened. However, an anti-surfactant behaviour needs to be addressed when using a hydrophilic substrate, as the addition of surfactant leads to poor wetting of the droplet on the hydrophilic substrate[169]. This usually happens in the case of oppositely charged surfactants and substrates. The surfactant would be directly absorbed onto the substrate, and the area beyond the contact line would be changed to be hydrophobic due to the exposure of the hydrophobic head to the air, which results in a poor wetting effect of the droplet. However, since the surfactant used in this project is Triton X-100, such an effect could be avoided. In addition, there is an upper limit for the effect of Triton loading on the droplet surface tension, which is called critical micelle concentration (CMC)[168]. This is the point where the surface tension of the ink stops changing with the increase of added surfactant. The surfactant starts to form micelles in this case rather than modulate the surface energy of the droplet.

As for the suppression of CRE, figure 38 shows that CRE has been supressed when the Triton loading decreases. There are two major effects of surfactant loading on the drying of a sessile droplet[168]. One is the surfactant-induced Marangoni flow; the other is its effect on particle interactions with other interfaces.

As mentioned before, using competition between convective Marangoni flow and radial capillary flow during droplet drying is a common method to acquire uniform patterns[134].

In this section, the strengthened Marangoni flow is due to a decrease in surfactant loading. During the droplet drying, the Triton molecules are transported and accumulate at the contact line area due to the capillary flow. Thus, the loading of Triton increased in this area and resulted in a decrease in the surface tension in the area as well. A surface tension gradient then forms between the apex and the contact line of the droplet, and a convective Marangoni flow is formed as well[134]. However, the effect of CMC must be mentioned as well. Since the surfactant-induced Marangoni flow originates from the surface tension gradient between the contact line and the apex of the droplet, this flow would be stopped when the surface tension gradient ceases to exist. This explains why the surfactant-induced Marangoni effect has been strengthened when Triton loading is low. As Triton loading decreased from 0.2 to 0.06 mg/ml, the duration for droplets to reach the CMC became longer. Therefore, a stronger surfactant-induced Marangoni effect could be obtained. Thus, the CRE can be further supressed when Triton loading is decreased. It is worth noting that the surfactant-induced Marangoni effect has also been reported to occur in loadings much greater than its CMC in the water (~0.2 mg/ml)[170]. Triton X-100 is not only a popular surfactant in the industry but also a common stabiliser used for graphene-based ink[111]. Therefore, the Triton molecules would also be absorbed on the graphene/liquid interface, so the actual CMC of Triton in the ink could be larger since not only the liquid/vapour but also the liquid/solid interfaces absorbed surfactants.

Regarding the effect of surfactant loading on particle interactions with other interfaces, there are three aspects that need to be mentioned, which are particle-to-particle interactions, particle-to-liquid/vapour interface interactions, and particle-to-substrate interactions, respectively.

The particle-to-particle interaction in the ink follows the DLVO theory[66]. In this, the electrostatic and van der Waals interactions are the repulsive and attractive forces among the particles. In this project, the rGO flakes are stabilised by the perylene stabiliser, which is negatively charged and provides a repulsive force. Triton X-100 is a non-ionic surfactant mainly used to modulate the droplet surface tension. It also attaches to rGO via the hydrophobic bonding and π–π interaction to stabilise the rGO[171]. It has been reported that when the surfactant concentration is close to its CMC, the distance between particles increases, so the van der Waals interactions are reduced. Thus, the sticking force between particles is reduced, which results in a small sticking probability. Thus, the particles tend to be transported to the contact line area and support the formation of ring stain[172]. Therefore, the higher Triton loading could strengthen the CRE, which also matches the results we observed in figure 38.

The particle-to-liquid/vapour interface interaction is controlled by two mechanisms; one is the possibility that particles are transported to the liquid/vapour interface, and the other is the ability of the liquid/vapour interface to capture these particles[168]. The strong particle-to-liquid/vapour interface interactions could suppress CRE as the particles are transported to the liquid/vapour interface and are captured by the interface. However, there is a prerequisite for this interaction to have an effect on droplet drying, which is the wettability of the particle surface. The surfactant type and concentration determine the wettability of the particle surface and also establish whether particles remain in the solvent or are transported to the liquid/vapour interface[168].

If the particles remain in the solvent, then the capture effect from the liquid/vapour interface does not supress the CRE. In this project, Triton X-100 molecules are absorbed onto rGO via the hydrophobic bonding and π–π interaction[171]. In this, the hydrophilic heads are exposed to the solvent bulk, which results in a hydrophilic surface of particles. Consequently, the rGO flakes prefer to stay in the solvent rather than the liquid/vapour interface. Thus, the particle interaction with the liquid/vapour interface would not affect the CRE in this case.

The particle-to-substrate interaction is similar to the particle-to-particle interaction, which can also be explained by DLVO theory[66]. In general, the oppositely charged particles and substrate could result in a uniformly dried pattern, as there is a low mobility of particles in the droplet due to the electrostatic attraction between particles and substrate. On the other hand, the like-charged particles and substrate would have an enhanced repulsion in between, which favours the formation of ring stains due to the improved mobility of the particles[168]. However, some special cases also should be mentioned. In terms of oppositely charged particles and substrate, there is a chance that either the substrate or particles are neutralised when the surfactant loading is at an intermediate concentration (in the case of electrostatically adsorbed surfactant). Then, the particles could be either transported to the liquid/vapour interface or stay in the solvent, depending on its surface wettability. When the surfactant loading is further increased to its CMC or above, either the particles or substrate reverses its charge due to the double-layer adsorption[173]. Thus, the attraction between particles and substrate could be tuned into repulsion, promoting the CRE. In terms of this project, perylene stabiliser is negatively charged, and the substrate is also slightly negative due to the cleaning process. The aim of washing the rGO/stabiliser dispersion seven times during its preparation is to remove the excess stabiliser from the prepared dispersion. So, the case that can reverse either charge of substrate or particle via formation of the double-layer adsorption is not considered either. Triton X-100 is a non-ionic surfactant that uses hydrophobic bonding and π-π interactions to attach to the rGO[171], so the particle surface can be turned into a hydrophilic form. Thus, repulsion is the interaction between particles and substrate in this project, which favours the formation of ring stains.

In all, on the one hand, the surfactant-induced Marangoni effect can be strengthened to compete with CRE when less Triton X-100 is used due to the longer duration to reach CMC. On the other hand, although the interactions between particles to particles, liquid/vapour interface, and substrate can be tuned by the loading of added surfactant, the surfactant used in this project is not ideal at manipulating these interactions except in tuning the particle surface into a hydrophilic form. Thus, the particle mobility in the droplet could be less affected by these particle interactions with other interfaces and give the internal flows more chance to manipulate their movements during the drying.

A lower Triton loading is preferred in this case as it can induce a stronger Marangoni effect to compete with the CRE during droplet drying. The 0.06 mg/ml Triton X-100 would be used as the surfactant loading in the next part of the exploration, as it has the best suppression on CRE. Thus, the base ink for the next part is ‘0.1rGO, 0.01/1EG, 0.06Tri with 0-minute UV at room temperature’.

In order to test the effect of the EG/DI ratio on the drying of sessile droplets, the experiment was conducted in the following way:

(1) a 1 µl droplet from ink ‘0.1rGO, 0.01/1EG, 0.06Tri’ was gently deposited on a Si wafer treated with 0-minute UV and dried at room temperature;

(2) the other four droplets from inks with different EG/DI ratios (0.05/1, 0.1/1, 0.5/1 and 1/1) were also deposited on the Si wafer following the same process;

(3) the Triton X-100 (0.06 mg/ml) and rGO (0.1 mg/ml) loadings were held constant in all five droplets, and the UV time (0 minutes) and platen temperature (room temperature) were also not changed. The only difference among these five droplets is the EG/DI ratio.

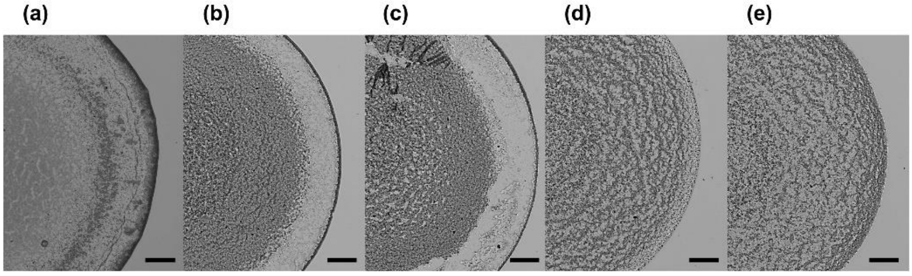

Figure 39 Optical microscope images of dried dots from ink ‘0.1 rGO, 0.01/1 – 1/1’ EG, 0.06 Tri’ with different EG/DI ratios ((a) – (e) correspond to EG ratios of 0.01/1, 0.05/1, 0.1/1, 0.5/1 and 1/1, respectively). The effects of the EG/DI ratio on droplet drying are the concerns at this stage. The UV time is 0 minutes, and the platen temperature is room temperature. The CRE effect was continuously supressed when EG loading increased from 0.01/1 to 0.5/1, and it was strengthened again when the EG/DI ratio was further increased to 1/1. The shapes of the final dried dots were changed from ring-dominated structures to dual-ring structures with a depletion zone when the EG/DI ratio was between 0.01/1 and 0.1/1; the dual-ring structure without a depletion zone could be observed in the dried dots when the EG/DI ratio was above 0.5/1. Such changes to the dried dots can be attributed to the change in the dominating solvent in the droplet when different EG loading has been used. Greater EG extended the duration of the CRE due to its low vapour pressure and increased loading, which makes the CRE regain control of the droplet drying. Black scale bar represents 200 µm.

The optical microscope images of the corresponding dried dots are pictured in figure 39. The dried dots have been labelled as (a), (b), (c), (d), and (e), which come from inks of 0.1 rGO, ‘0.01/1 – 1/1’ EG, 0.06 Tri, and dry on a Si wafer treated with 0-minute UV at room temperature. The values of W and R and their ratios of these five dots are summarised in table 13.

Since the loading of Triton X-100 was maintained at 0.06 mg/ml, the surfactant-induced Marangoni effect exists in all five droplets but ceases once its concentration in the droplet reaches the CMC. The effect of EG loading on the droplet drying uniformity is the focus of this section.

As figure 39 shows, the dot diameter has decreased continuously from ~1.34 × 10^3 µm to ~1.16 × 10^3 µm when the EG/DI ratio increased from 0.01/1 to 0.5/1, and it lightly increased when the EG/DI ratio reached 1/1. In theory, the dot diameter should become larger as more EG reduces the surface tension of the droplets and results in a smaller contact angle. Thus, the dot diameter should be larger based on the volume conservation. However, the findings go in the opposite direction. As mentioned before, when DI is the major solvent, the large volume loss of volatile solvent with smaller viscosity in a binary system results in a sudden increase in droplet viscosity[164]. Thus, the dot diameter could decrease with an increase in EG loading, as more energy could be consumed by the higher viscous dissipation. However, when EG is the major solvent, such a phenomenon is not happening, and the dot diameter increases again when more EG is used. This could be explained by the change of viscosity not being as obvious compared to the case where EG is the major solvent. So, a lower contact angle could result in a larger dot diameter again.

The W values have a different trend. They decreased from ~53.06 µm to ~13.27 µm when the EG/DI ratio increased from 0.01/1 to 0.5/1, and they increased to ~23.47 µm when the ratio further increased to 1/1. A similar trend has been found in the calculated W/R values, in which the minimum value was ~0.01 when EG/DI = 0.5/1. As for the shape of the dried dots, the coffee-ring effect with particles uniformly distributed in the interior area could be observed when EG/DI = 0.01/1. Then, the clear dual-ring structures with a depletion zone in between were observed from the dots with EG/DI = 0.05/1 and 0.1/1. After that, the dots with EG/DI = 0.5/1 and 1/1 have the dual-ring structure without a depletion zone in between, and the best drying uniformity was found when EG/DI = 0.5/1. The liquid composition, like the EG/DI binary system in this case, has a strong influence on the competition between internal flows and the drying dynamics of the droplet[134].

The continuous decrease in the dot diameter could be explained by the increased viscosity of the droplet due to the addition of EG.

	0.01/1 EG	**0.05/1 EG**	**0.1/1 EG**	**0.5/1 EG**	**1/1 EG**
W (µm)	53.06 ± 4.32	22.45 ± 3.91	22.45 ± 2.39	13.27 ± 3.77	23.47 ± 2.41
R (µm)	1.34×10^3 ± 18.89	1.22×10^3 ± 21.67	1.16×10^3 ± 22.78	1.16×10^3 ± 31.01	1.16×10^3 ± 23.76
W/R	0.04	0.02	0.02	0.01	0.02

Table 13 Values of W, R, and their ratios of dried dots from the formulations with different EG/DI ratios. The diameters of these dots continuously decreased with greater proportions of EG in the ink until EG/DI > 0.5/1. Additionally, the W/R ratios of these dots first increased with the increase in EG loading and reduced again when the EG ratio was larger than 0.5/1.

The ethylene glycol has a viscosity of ~16 mPa.s at 25 ℃, which is much higher than that of DI water (~1 mPa.s at 25 ℃)[142]. So, when the EG/DI ratio increased from 0.01/1 to 1/1, the increased droplet viscosity resulted in a higher viscous dispassion to the droplet spreading and left a smaller dot diameter. At the same time, the droplets become closer in composition to EG as its loading increases in the formulation. The initial contact angle of the droplet should decrease as EG (~47 mN/m at 25 ℃) has a smaller surface tension compared to that of DI water (~72 mN/m at 25 ℃)[142]. Then, it is important to note that this reduction of contact angle results in an increase in the evaporation rate as well[165,166]. Based on the formation mechanisms of surfactant-induced Marangoni effect and co-solvents induced Marangoni effect, the increased evaporation rate could make the accumulation of Triton in the contact line area faster and stimulate more evaporation of water in this area as well. So, both CRE and Marangoni effects could be strengthened at the same time, and the strengthened ring stain and centre disk should theoretically be observed when EG increases. However, this trend was not observed in figure 39. This could be explained by the change of EG loading in the EG/DI binary system. Although the evaporation rate could be increased as the contact angle decreased, there is a volume difference between the loaded EG and DI among these droplets. When the contact angle decreases with increased EG loadings, the evaporation rates of DI and EG should increase. However, the increased loading of EG would dominate the drying process, and the CRE would thus dominate again due to the low vapour pressure of EG[142], so such a trend could not be observed in figure 39.

As for the formation of dual-ring structures and a depletion zone, two possible mechanisms have been reported. One is the contact line receding due to the decrease in the contact angle as the evaporation continues. Then, the contact line can be fixed again during this process, and the depletion zone is created in this case[174]. Since there was no contact reeding observed throughout the experiment, this mechanism could be excluded.

The other mechanisms, such as dual-ring structure and depletion zone, are a result of competition between the CRE and the Marangoni effect[131,175,176]. The Marangoni effect is usually used to supress the CRE while the droplet dries, as it can transport the particles from the ring stain back to the droplet centre. The dual-ring structure is a common phenomenon when the Marangoni effect is applied to modulate droplet drying[134]. However, the dual-ring structure with a depletion zone in between is a special case, and it can induce drying issues like ‘waviness’ found in this project, as the drop spacing could not be set correctly in this case. Talbot et al. reported two binary systems (Ethanol (EtOH)/DI and EG/DI) to explore this special case[175,176]. They were mainly focused on the competition between co-solvents induced Marangoni effect and CRE. The relationship between the strength, duration, and direction of the Marangoni effect and the formation of dual-ring structures with a depletion zone has been studied based on these two binary systems. In order to observe the effect of the Marangoni effect, they used a hydrophobic polymer as a tracer. This increases the possibility for particles to be transported to the liquid/vapour interface, which might supress the CRE[168]. However, their results indicated that this suppression effect did not happen. The competition between the CRE and the Marangoni effect could be observed under a high-speed camera, so the mechanisms they found could be used as a reference point in this project. Firstly, they found that no matter the application of EtOH (higher vapour pressure than DI water) or EG (lower vapour pressure than DI water), the strength of the co-solvents induced Marangoni effect is always stronger when smaller loadings of EtOH or EG are used. This strength becomes smaller when the EtOH or EG loading is increased in the droplet. Secondly, they found that the formation of the dual-ring structure with a depletion zone in the EG/DI system is strongly related to the duration of CRE for the whole drying process. The shortened CRE supports the formation of a depletion zone in the dual-ring structure. Thirdly, the direction of co-solvents induced Marangoni effect determines the circulatory region in the droplet. When the Marangoni flow is from the apex to the contact line, it will directly compete with the capillary flow, pushing the circulatory region to the droplet centre. On the other hand, the circulatory region would be in between the two rings when the Marangoni flow travels from the contact line to the apex. This also helps the formation of the depletion zone.

Back to the shape of the dried dot, figure 39 shows the shape changed from ring-dominated to dual-ring with a depletion zone when EG loading increased, and it converted to a dual-ring structure without a depletion zone when the EG/DI ratio was further increased above 0.5/1. Since the Triton loading is held constant in all these fives dots, the main changes of these dots are caused by the increased EG loading in the droplets.

As discussed before, the movement of particles in this project is mainly influenced by the competition of internal flows within the droplet during drying. Combining the dried dots from figure 39 with what Talbot et al. reported[175,176], the effects of the EG/DI ratio on the droplet drying can be described. Figure 40 illustrates four major steps during the drying of droplets with different EG/DI ratios:

(1) the particles are uniformly distributed in the droplet;
(2) the formation of a circulatory region in the droplet;
(3) the stop of the Marangoni flow;
(4) capillary flow dominated droplet drying.

Since different EG/DI ratios have been used in these five dots, both the strength and duration of the Marangoni effect are changed, and the final step of the drying process could be divided into DI dominated drying, and EG dominated drying, depending on the EG/DI ratio[175,176]. The details of these four steps in these two cases are described as follows:

In step (1), the particles are uniformly distributed in the droplet at the beginning, and evaporation of the droplet starts.

In step (2), the capillary flow due to faster evaporation at the contact line area brings the particles to the edge. Then, the ring stain is formed in this area.

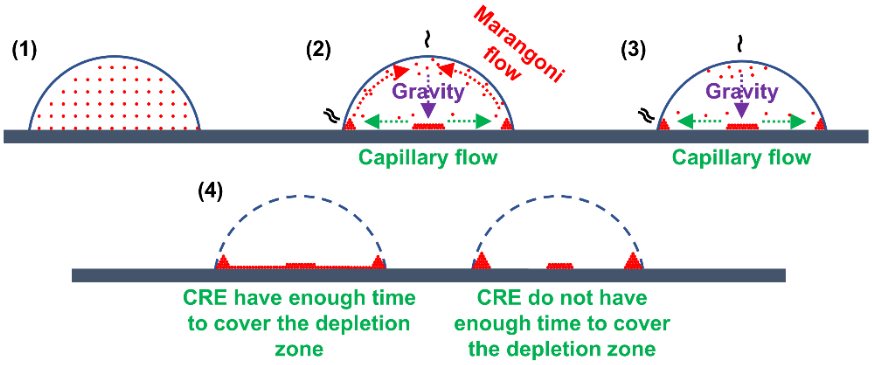

Figure 40 Major steps during the drying of droplets with different EG/DI ratios; (1) particles uniformly distributed in the droplet; (2) formation of the Marangoni and capillary flows; (3) the stop of the Marangoni flow; and (4) capillary flow dominated droplet drying. The formation of a depletion zone is dependent on whether the rest of the solvent can provide enough duration for CRE to transport the particles back to the contact line again.

At the same time, the accumulated surfactants and evaporated DI water make the surface tension in this area drop dramatically, so a surface tension gradient is formed[134]. Thus, the Marangoni flow from the contact line area to the apex of the droplet is formed. It is hypothesised that the circulatory region would be formed in the area between the outer ring and the centre disk of the droplet when the direction of the Marangoni flow is from the contact line to the apex[175]. So, the particles are continuously transported from the droplet centre to the edge via capillary flow, and the particles in the edge are transported back to the centre by the Marangoni flow at the same time. In addition, the strength of co-solvents induced Marangoni effect is strongly related to the EG/DI ratio[176]. It decreases when higher EG loading has been applied, so the strength of co-solvents induced Marangoni flow continuously decreases when the EG/DI ratio changes from 0.01/1 to 1/1. However, the duration change of this Marangoni effect with EG loading is slightly complex. There is a critical point in the EG volume ($V_{critical}$) which switches the drying from DI dominated to EG dominated. In the case of DI dominated drying, the more EG loaded, the strength of the Marangoni flow decreases, but the duration of the Marangoni effect becomes longer. In the case of EG dominated drying, the higher EG loading also reduces the strength of the Marangoni flow, but the duration of the Marangoni effect decreases as the EG further dominates the droplet drying. In the former case, it is difficult to distinguish the change of the Marangoni effect, as its strength and duration change in the opposite direction. As for the latter case, both the strength and duration of the Marangoni effect decrease. Thus, the relationship between $V_{critical}$ and the range of EG/DI ratio (0.01/1 to 1/1) is important in this step. If the $V_{critical}$ < (0.01/1 to 1/1), every ratio used in this project would be in the range of EG dominated drying. In that case, the increase of EG loading would result in a continuous decrease of both strength and duration of the Marangoni effect. Thus, the depletion zone would not be observed when EG loading was increased. However, if the $V_{critical}$ > (0.01/1 to 1/1), then the DI water would dominate the drying. This possibility should be excluded since Talbot et al. found that, in the case of EG/DI = 1/1, it only took ~2 s to evaporate all the DI water, while it took ~232 s to fully evaporate all the EG[176]. Thus, the $V_{critical}$ should be in between 0.01/1 and 1/1. In this range, the strength of the co-solvents induced Marangoni flow should decrease continuously as the EG loading increases. The duration of this Marangoni flow should increase at first and then decrease again when EG loading is over the $V_{critical}$.

In step (3), the Marangoni flow is stopped in two cases. One is that the co-solvent with higher evaporation rate (DI water in this project) has been fully evaporated (under the assumption that CMC has not yet been reached); the other is that the CMC of surfactant has been reached in the droplet due to the volume loss of solvent during the evaporation. Thus, there is no surface tension gradient in this case.

In step (4), there is only capillary flow left after the Marangoni flow ends. Then, the capillary flow starts to transport particles from the centre disk to the edge. In the case of DI dominated drying, when the remaining volume of DI water is large enough, the CRE in this step could bring most of the particles from the centre disk to the edge area; in this case, a depletion zone could be supressed. On the other hand, when the remaining volume of DI water is not large enough, the typical dual-ring structure with a depletion zone could be observed in the dried dot, as the CRE does not have time to move particles to cover this depletion zone. Regarding the case of EG dominated drying, both the strength of the Marangoni flow and its duration are supressed. Then, only a narrow depletion zone is formed, if one is formed at all since it might not be able to form a depletion zone due to the weakened Marangoni flow. Then, the long duration of EG dominated drying could easily supress this narrow depletion zone. Thus, the dried dot could be in the structure of a typical dual-ring without a depletion zone.

Thus, the shapes of the dried dots from figure 39 can be explained. When EG/DI = 0.01/1, although the strength of the co-solvents indued Marangoni flow should be strongest among the five dots, the major solvent is DI water. So, the CRE could still transport all the particles back to the contact line area, leaving a ring-dominated structure. When EG/DI further increased to 0.05/1 and 0.1/1, the dual-ring structure with depletion zone could be observed. As discussed above, this structure would happen as the duration of DI dominated CRE is not long enough. In that case, the CRE could not transport the particles to cover the depletion zone. Once the EG/DI ratio is larger than 0.5/1, the major solvent becomes EG, so the strengthened CRE could help the suppression of the depletion zone and leave the dual-ring structure without a depletion zone.

In all, the EG/DI ratio in the droplet could have significant influences on the droplet drying. In the EG/DI binary system, EG has smaller vapour pressure with lower surface tension, and the DI water has higher vapour pressure with higher surface tension. So, DI water theoretically evaporates at the contact line area first and forms a Marangoni flow from the contact line area to the apex of the droplet. Then, this direction of the Marangoni flow helps the formation of the circulatory region in between the outer ring and centre disk. When the EG/DI ratio changed from 0.01/1 to 1/1, the strength of the co-solvents induced Marangoni flow decreased continuously, but the duration of the Marangoni effect might increase at first when DI is the major solvent, though it could reduce again when EG is the major solvent. Then, after the stop of the Marangoni effect, the duration of the remaining CRE determines the shape of the final dried dot. When DI is the major solvent, the dual-ring structure with a depletion zone could be formed when CRE duration is not long enough. Then, the depletion zone could be supressed when EG is the major solvent, as it could extend the CRE duration for the droplet drying.

The droplet with an EG/DI ratio of 0.5/1 shows the best uniformity among these dried dots. So, this ratio is used as the EG loading in the next exploration; the starting point for the next step is ‘0.1rGO, 0.5/1EG, 0.06Tri with 0-minute UV at room temperature’.

The above explorations show the effects of Triton and EG loadings on droplet drying. A droplet with an acceptable drying uniformity has been found and is used as the starting point in the coming sections. Thus, a further exploration of the effects of rGO loading, UV time, and platen temperature is conducted to provide a guide on how to formulate the ink and modify the substrate for improving droplet drying uniformity.

In order to test the effect of rGO loading on the drying of sessile droplets, the experiment was conducted in the following way:

(1) a 1 μl droplet from ink ‘0.1rGO, 0.5/1EG, 0.06Tri’ was gently deposited on a Si wafer treated with 0-minute UV and dried at room temperature;
(2) another droplet from an ink with different rGO loading of 0.5 mg/ml was deposited on the Si wafer following the same process;
(3) the Triton X-100 (0.06 mg/ml) and EG/DI ratio (0.5/1) were held constant in these two droplets, and the UV time (0 minutes) and platen temperature

(room temperature) were also not changed. The only difference among these two 1 µl droplets is the rGO loading.

The optical microscope images of the corresponding dried dots are shown in figure 41. The dried dots have been labelled as (a) and (b) and come from inks of ‘0.1 & 0.5’rGO, 0.5/1EG, 0.06Tri, and dried on Si wafers treated with 0-minute UV at room temperature. The values of W and R and their ratios of these two dots are summarised in table 14.

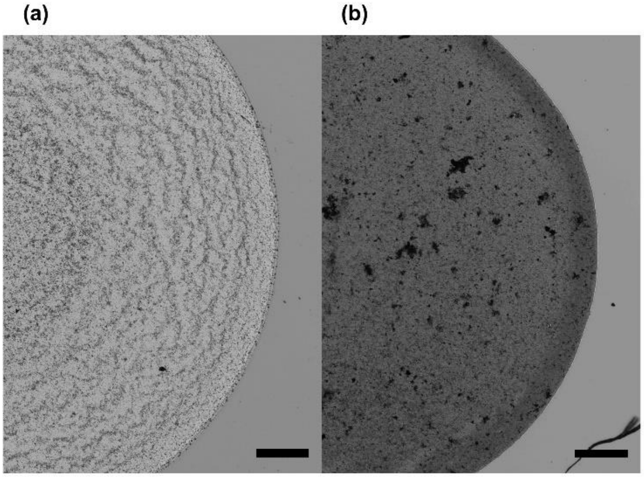

Figure 41 Optical microscope images of dried dots from ink ‘0.1 & 0.5’rGO, 0.5/1EG, 0.06Tri’ with different rGO loadings, including (a) 0.1 mg/ml rGO and (b) 0.5 mg/ml rGO. The effects of rGO loading on droplet drying are the concerns at this stage. The UV time is 0 minutes, and the platen temperature is room temperature. The increase of rGO loading results in the strengthening of both the CRE and Marangoni effect, as both wider ring stain and depletion zone could be observed in the final dried dot with higher rGO loading. Since the CRE regains control when the EG/DI ratio = 0.5/1, the increased rGO loading could strengthen this effect and leave a more obvious ring stain. In the meantime, the increased rGO loading would extend the duration of surfactant-induced Marangoni effect, as more Triton would be absorbed onto the rGO surface. So, the depletion zone could be observed again in this case. Black scale bar represents 200 µm.

	0.1 mg/ml rGO	**0.5 mg/ml rGO**
W (μm)	13.27 ± 3.77	91.84 ± 4.01
R (μm)	1.16×10^3 ± 31.01	0.99×10^3 ± 12.31
W/R	0.01	0.09

Table 14 Values of W, R, and their ratios of dried dots from the formulations with different rGO loadings. The dot diameter decreased when rGO loading increased from 0.1 to 0.5 mg/ml. Conversely, the increase in ring stain width results in an increase in the W/R ratio, which indicates a stronger CRE in the dried dot.

As figure 41 shows, the dot diameter has slightly decreased from ~1.16×10^3 μm to ~0.99×10^3 μm when the rGO loading increased from 0.1 to 0.5 mg/ml. However, the W values reveal an opposite trend: It increased from ~13.27 μm to ~91.84 μm when rGO loading increased from 0.1 to 0.5 mg/ml. Thus, the W/R ratios increased from 0.01 to 0.09 due to this rGO loading change. As for the shape of the dried dots, the clear ring stain could be observed in the dried dot with 0.5 mg/ml rGO.

The increased rGO loading results in an increase in the surface tension and viscosity of the droplet. The higher surface tension could be caused by the absorption of Triton onto the rGO surface, as it is also a common stabiliser to graphene[111]. So, when the rGO loading increased in the droplet, the Triton could be absorbed onto graphene surface as well. Then, the Triton on the liquid/vapour interface could be reduced, resulting in an increase in the surface tension. At the same time, the higher contact angle could result in a decreased evaporation rate at the contact line area[165,166]. Since both surfactant and co-solvents induced Marangoni effects originate from the higher evaporation rate at the contact line area, the reduced evaporation rate at the contact line area could reduce the strength of both the CRE and Marangoni effect at the same time. On the other hand, the drying mode of these two droplets is the CCD mode, so the contact angle continuously decreases during the evaporation process, and the strength of the CRE and Marangoni effect is continuously increasing and competing with each other during this process. So, both the CRE and Marangoni effect should be supressed at the start, and they would be accelerated as the evaporation continues.

Although the base ink used here is from the dot with the best drying uniformity from the previous exploration on the effect of EG, based on the discussion from the previous section, the CRE regains control of the drying process when the EG ratio is higher than 0.5/1. So, the CRE is stronger than the Marangoni effect in this case. Since more Triton molecules can be absorbed onto the rGO surface, the less amount of Triton in the solvent would also extend the duration of surfactant-induced Marangoni effect during droplet drying. So, this explains why two narrow depletion zone could be observed in the final dried dot. Furthermore, the effect of particle concentration in droplet drying is still controversial in the related literature. It could help the formation of uniform dried patterns by simply increasing particle concentration[177]. However, there are also some examples demonstrating that the high concentration of particles could degrade the pattern uniformity by introducing stick-slip behaviour in the dried dot[178]. Furthermore, there is also a report documenting that the increase in particle concentration leaves a mild or no effect on the formation of ring stains but increases its thickness[179]. Thus, the effect of particle concentration might change case by case. As discussed before, the particles have hydrophilic surfaces, and they are like charges with the substrate in this project. In other words, they prefer to stay in the solvent and do not tend to stick with the substrate either. Thus, the transportation of particles in this project is strongly influenced by the competition of internal flows in the droplet.

In order to test the effect of UV time on the drying of sessile droplets, the experiment was conducted in the following way:

(1) a 1 µl droplet from ink ‘0.1rGO, 0.5/1EG, 0.06Tri’ was gently deposited on a Si wafer treated with 0-minute UV and dried at room temperature;

(2) another droplet from the same ink was deposited on the same type of substrate treated with different UV times (20 minutes) at room temperature;

(3) the only difference between these two 1 µl droplets is the UV time for the substrate.

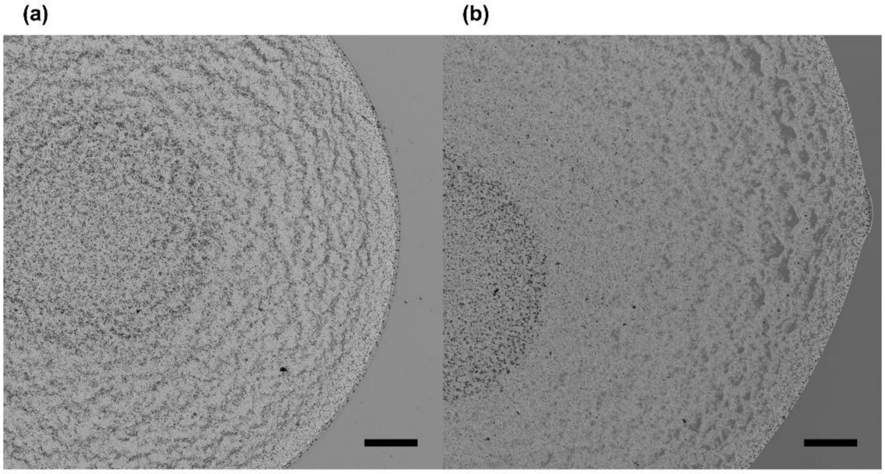

Figure 42 Optical microscope images of dried dots from ink ‘0.1rGO, 0.5/1EG, 0.06Tri’ with different UV times, including (a) 0-min UV and (b) 20-mins UV. The effects of UV time on droplet drying are the concerns at this stage. The platen temperature is 60℃. The increase in UV time improves the hydrophilicity of the substrate. Then, the reduced contact angle results in an increase in the evaporation rate of the contact line area. Thus, both the CRE and Marangoni effect could be strengthened in this case. Due to the different vapour pressures of DI and EG, the strengthening of the Marangoni effect is more obvious than the CRE and results in a shaper centre disk in the dot dried on the substrate treated with longer UV time. Black scale bar represents 200 µm.

The optical microscope images of the corresponding dried dots are presented in figure 42. The dried dots have been labelled as (a) and (b) and come from inks of 0.1rGO, 0.5/1EG, 0.06Tri, dry on a substrate with ‘0 & 20’ UV at room temperature, respectively. The values of W and R and their ratios of these two dots have been summarised in table 15.

	UV = 0 minutes	UV = 20 minutes
W (µm)	13.27 ± 3.77	16.33 ± 3.51
R (µm)	1.16×10^3 ± 31.01	1.41×10^3 ± 21.78
W/R	0.01	0.01

Table 15 Values of W, R, and their ratios of the dried dots from the formulations with different UV Ozone times. The dot diameter increased dramatically when UV time increased from 0 to 20 minutes. At the same time, the W/R ratios of both dots indicate that the CRE in their cases is supressed.

As figure 42 shows, the dot diameter increased from ~1.16×10^3 µm to ~1.41×10^3 µm when the UV time increased from 0 to 20 minutes. The W/R ratios of these two dots are both close to 0.01. As for the shape of dried dots, the centre disk of the dot with longer UV time is sharper, and it is further spread on the substrate as well. The main effect of the UV Ozone treatment on the substrate is to control its surface wettability. The longer UV time could make the substrate more hydrophilic. When the substrate is hydrophobic, the droplet recedes and dries as a small and concentrated dot due to the substrate's strong hydrophobicity[134]. On the other hand, a larger droplet could be obtained when a longer UV time was applied on the substrate. This explains why the dot diameter increased dramatically in the case of 20-minutes UV. Then, the droplet would have a smaller contact angle in this case as the droplet widely spreads on the substrate. Thus, the evaporation rate at the contact line area could be increased, and the capillary flow could be strengthened in this case[165,166]. At the same time, the strengthened capillary flow transports more Triton to the contact line area, and more DI water is evaporated in this area as well. Consequently, the surface tension in the contact line area drops significantly due to this increased evaporation rate, and the strength of the Marangoni flow is increased as well. As previously mentioned, the major solvent of the droplet turned into EG when the EG/DI ratio > 0.5/1. So, the CRE dominated the drying process in this case. However, based on the dried dot from figure 42 (b), the centre disk is much sharper and larger than the dot from figure 42 (a), which indicates that the Marangoni effect has been strengthened in this case. In the meantime, the CRE should also be strengthened in this case as well. However, the change in the W/R ratio and the dot from figure 42 (b) indicate that the strengthening of CRE is not obvious. This could be explained by the low vapour pressure nature of EG, so the capillary flow in EG might be strengthened to a limited extent compared to that of DI water. So, the CRE did not become more obvious while the strengthening of the Marangoni effect could be observed.

In order to test the effect of the platen temperature on the drying of sessile droplets, the experiment was conducted in the following way:

(1) a 1 µl droplet from ink ‘0.1rGO, 0.5/1EG, 0.06Tri’ was gently deposited on a Si wafer treated with 0-minute UV and dried at room temperature;
(2) another droplet from the same ink was deposited on the Si wafer treated with 0-minute UV at 60 ℃;
(3) the only difference between these two 1 µl droplets is the platen temperature for the substrate.

The optical microscope images of the corresponding dried dots are shown in figure 43. The dried dots have been labelled as (a) and (b) and come from inks of 0.1 rGO, 0.5/1 EG, 0.06 Tri, dried on the substrate with 0-min UV at ‘room temperature & 60 ℃’, respectively. The values of W and R and their ratios of these two dots have been shown in table 16.

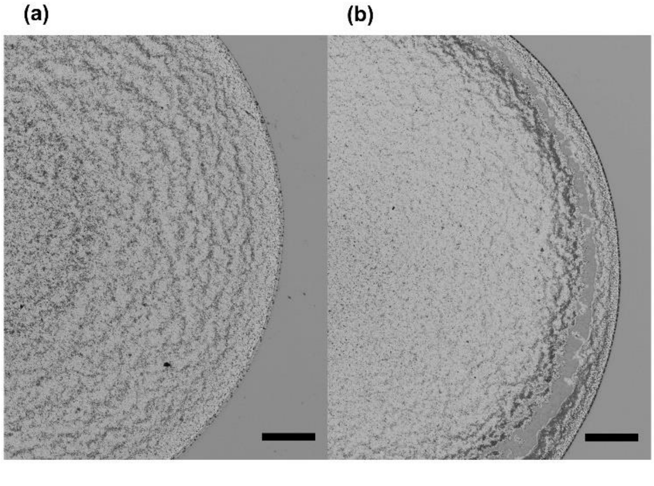

Figure 43 Optical microscope images of the dried dots from ink ‘0.1rGO, 0.5/1EG, 0.06Tri’ with different platen temperatures, including (a) room temperature and (b) 60 ℃. The UV time is 0 minutes. The effects of the platen temperature on droplet drying are the concerns at this stage. The increase in temperature results in the acceleration of droplet evaporation, which is similar to the effect of a longer UV time. Thus, both the CRE and Marangoni effect can be strengthened. However, the higher platen temperature increases the evaporation rate of EG as well. So, both a strengthened ring stain and a depletion zone could be observed at the same time. Black scale bar represents 200 µm.

	RT	60 °C
W (μm)	13.27 ± 3.77	81.63 ± 4.55
R (μm)	1.16×10^3 ± 31.01	1.15×10^3 ± 31.01
W/R	0.01	0.07

Table 16 Values of W, R, and their ratios of the dried dots from the formulations with different platen temperatures. The increased platen temperature results in a wider ring stain, while the change in dot diameter is not obvious. Thus, an increase of W/R ratio was observed.

As figure 43 shows, the dot diameter has slightly decreased from ~1.16×10^3 μm to ~1.15×10^3 μm when the platen temperature increased from room temperature to 60 °C. However, the ring width increased dramatically from ~13.27 μm to 81.63 μm. Similarly, the W/R ratios of these two dots increased from 0.01 to 0.07. As for the shape of the dried dots, the increased platen temperature results in the formation of a dual-ring structure again, and the ring stain has been strengthened in this case as well.

The increased platen temperature could accelerate droplet evaporation. Although the thermally induced Marangoni effect is generally mentioned when the substrate has been heated, its strength is not at the same magnitude as the surfactant-induced and co-solvents induced Marangoni effects[134]. So, the major effect of increased platen temperature is believed to be the increase in the droplet evaporation rate. Similar to the case of increasing UV time, an increased evaporation rate could strengthen both the CRE and Marangoni effect at the same time. But in this case, the evaporation rate of EG has been increased dramatically based on the final dried dot from figure 43 (b). On the one hand, more particles have been transported to the contact line area and formed a stronger ring stain. On the other hand, the strengthened Marangoni effect could bring more particles to the dot centre. The sample formed a depletion zone, which means the duration of CRE has been shortened in this case. The CRE and Marangoni effect can be strengthened spontaneously when a high platen temperature is applied. In the meantime, the increased evaporation rate shortens the duration of the CRE only section and results in a formation of another depletion zone.

In all, the results indicate that a higher platen temperature increases the evaporation rate dramatically compared to that of longer UV time. The increased evaporation rate could strengthen both the CRE and Marangoni effect at the same time. In addition, the duration of the CRE only section could also be shortened dramatically, which results in the formation of a depletion zone and proves the formation mechanism behind the depletion zone again.

In conclusion, the effects of individual factors on the droplet drying uniformity have been explored in this section. The series of Triton loadings, EG/DI ratios, rGO loading, UV time, and platen temperatures have been used to find an ink formulation with the best drying uniformity under a certain UV time and platen temperature. The effects of the above factors on the droplet drying could be concluded as follows:

(1) the decrease of Triton loading can help the suppression of CRE, as it takes a longer duration to reach CMC with less Triton;

(2) the reduction of Triton loading could increase the contact angle at the beginning, as it increases the surface tension of the droplet, so the whole drying process becomes longer due to the lower initial evaporation rate;

(3) the increase in the EG/DI ratio could divide the droplet drying into two categories: one is DI water dominated drying, which forms the ring-dominated structure or dual-ring structure with a depletion zone depending on the duration of DI dominated CRE; the other is EG dominated drying, wherein the CRE regains control of the droplet drying due to EG’s increased amount and low vapour pressure nature, which support the suppression of a depletion zone in the dual-ring structure;

(4) the increase of rGO loading results in a similar effect to using less Triton, which can reduce the dot diameter and extend the duration of the surfactant-induced Marangoni effect;

(5) the longer UV time and higher platen temperature both accelerate the evaporation rate of droplets to different extents. On the one hand, the strengthened Marangoni effect is more obvious than CRE in samples treated with longer UV times, as the low vapour pressure of EG limits the strengthening of CRE in this case. On the other hand, higher platen temperature could bring the dual-ring structure with a depletion zone back and strengthen the ring stain at the same time.

4.4.2 Effects of modifiers on droplet drying uniformity

The above exploration only focuses on the effects of individual factors, but the situation becomes much more complex in the preparation of functional inks. For this project, the final ink was prepared by mixing the initial rGO dispersion with a modifier. The modifier in this project is a mixture of DI water, Triton, and EG in a designed ratio. Since different loadings of Triton and EG are needed to modulate the rheological properties of the prepared ink and make the ink inkjet printable, exploration of the effects of modifiers on droplet drying uniformity is needed. Various Triton loadings (0.2 to 0.06 mg/ml) and EG loadings (0.01/1 to 1/1) were investigated. Then, the effects of rGO loading, UV time, and platen temperature on this system were also considered as well. Finally, a guideline was developed from above explorations for the preparation of inkjet printable large rGO water-based inks. 0.06 mg/ml Triton was chosen based on a reported similar water-based GNP ink[74], and 0.2 mg/ml Triton was selected, as this value is close to its CMC in water[170]. The range of EG loading was adopted from Talbot's project for comparison[175,176]. Additionally, figures 44 through 47 focus on the centre of the dry dot instead of the annular region for consistency, as many dots lack images of the annular region.

Figure 44 shows formulations starting from '0.1rGO, 0.01/1EG, 0.2Tri' (a-1). Then, the rGO loading was maintained at 0.1 mg/ml, the UV was kept at 0 minutes, and the platen temperature was room temperature. The EG loadings were set as 0.01/1, 0.05/1, 0.1/1, 0.5/1, and 1/1 by volume (labelled as a, b, c, d, and e, respectively). The Triton X-100 loadings were set as 0.2, 0.1, and 0.06 mg/ml (labelled as 1, 2, and 3, respectively). The values of W and R and their ratios are summarised in table 17.

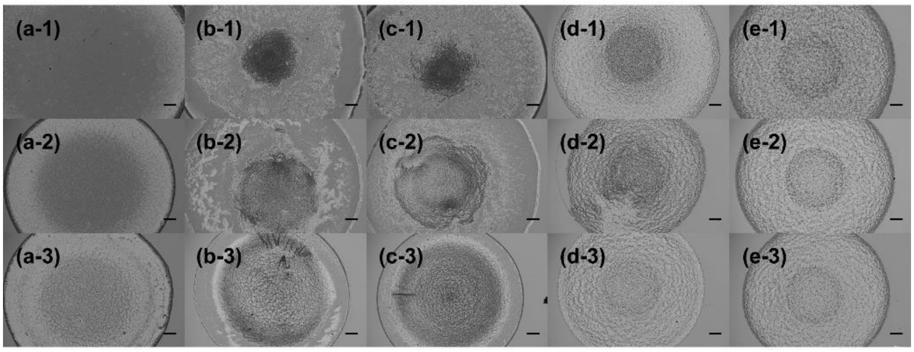

Figure 44 Optical microscope images of the dried dots from inks of '0.1 rGO, 0.01/1 – 1/1 EG, 0.2 – 0.06 Tri'. As for the ink formulations, the EG/DI ratios change horizontally from 0.01/1 to 1/1 (a – e), and Triton loadings change vertically from 0.2 to 0.06 mg/ml (1 – 3), while the rGO loading is maintained at 0.1 mg/ml. The UV time and platen temperature for the substrate are held at 0 minutes and room temperature, respectively. The aim of this stage is to check the effects of modifiers on droplet drying. In general, lower Triton loading results in a longer duration for droplets to reach CMC, which extends the duration of surfactant-induced Marangoni effect and results in the suppression of the CRE. The increase in the EG/DI ratio changes the shape of the dried dots from a ring-dominated structure to a dual-ring structure with a depletion zone when the EG/DI ratio changes from 0.01/1 to 0.1/1; the dot shape becomes a dual-ring structure without a depletion zone when the EG/DI ratio is larger than 0.5/1. This change is caused by the major solvent in the droplet. When the EG/DI ratio is between 0.01/1 and 0.1/1, DI is the major solvent, and the increase in EG results in a longer Marangoni effect. However, the shortened CRE leads to the formation of a depletion zone, as there is not enough time to transport all the rGO flakes back to the edge. Once the EG/DI ratio is between 0.5/1 and 1/1, the major solvent is EG in the droplet. The low vapour pressure of EG and its increased loading in the droplet could make the CRE capable of transporting flakes back to the edge and supressing the depletion zone. Black scale bar represents 200 µm.

	a1	b1	c1	d1	e1
W (µm)	86.22 ± 3.72	54.08 ± 2.34	47.96 ± 3.31	34.69 ± 4.54	61.22 ± 5.41
R (µm)	1.78×10^3 ± 12.54	1.52×10^3 ± 31.09	1.56×10^3 ± 23.21	1.33×10^3 ± 24.31	1.38×10^3 ± 27.67
W/R	0.05	0.04	0.03	0.03	0.04
	a2	**b2**	**c2**	**d2**	**e2**
W (µm)	54.08 ± 3.18	44.90 ± 3.89	20.41 ± 3.89	13.27 ± 3.44	59.18 ± 3.59
R (µm)	1.35×10^3 ± 18.79	1.32×10^3 ± 27.63	1.46×10^3 ± 45.31	1.17×10^3 ± 23.47	1.26×10^3 ±31.99
W/R	0.04	0.03	0.01	0.01	0.05
	a3	**b3**	**c3**	**d3**	**e3**
W (µm)	53.06 ± 4.32	22.45 ± 3.91	22.45 ± 2.39	13.27 ± 3.77	23.47 ± 2.41
R (µm)	1.34×10^3 ± 18.89	1.22×10^3 ± 21.67	1.16×10^3 ± 22.78	1.16 ± 31.01	1.16 ± 23.76
W/R	0.04	0.02	0.02	0.01	0.02

Table 17 Values of W, R, and their ratios of the droplets dried from inks of '0.1 rGO, 0.01/1 – 1/1 EG, 0.06 – 0.2 Tri' dried on Si wafer treated with 0-min UV at room temperature. The dot radius of the above droplets generally decreases when more EG or less Triton have been loaded in the droplet. There is only one exception: the dot radius is slightly increased when the EG/DI ratio increases from 0.5/1 to 1/1. The ring width is supressed when less Triton has been used; it would be supressed when the EG/DI ratio has increased from 0.01/1 to 0.5/1, and it would be supressed again when the EG/DI ratio reaches 1/1.

The third row of figure 44 (rows a-3 to e-3) shows the dots that are the same samples discussed in the previous section. The ring-dominated structure was observed in a-3 due to the water dominated drying process. Then, the dual-ring structure with a depletion zone could be observed when the EG/DI ratio increased to 0.05/1 and 0.1/1, respectively. This type of dried dot could be explained by the shortened duration of water dominated CRE. In this, the particles do not have time to reach the edge, and the depletion zone is formed. When the EG/DI ratio was further increased above 0.5/1, the EG became the major solvent in the droplet. Thus, the CRE regains control of the drying process due to its increased loading and low vapour pressure nature. Thus, the dual-ring structure without a depletion zone is seen in dots a-4 and a-5.

A similar trend can be observed in the other two rows of figure 44. The shape of the dried dots was changed from a ring-dominated structure to a dual-ring structure with a depletion zone when the EG/DI ratio increased from 0.01/1 to 0.1/1. Then, the dots further changed into a dual-ring structure without a depletion zone when the EG/Di ratio increased above 0.5/1.

It is worth noting the increase in dot size when the EG/DI ratio changed from 0.5/1 to 1/1. As mentioned before, the dot diameter should be larger when more EG has been used, as the surface tension of the droplet should be smaller when more EG is included. However, in a binary system (EG/DI system in this project), when the major solvent with less viscosity is more volatile, then a sudden increase in viscosity could be achieved due to the large volume loss of the volatile solvent[164]. Thus, the dot diameter decreases with increases in EG loading, as more energy can be consumed by the higher viscous dissipation. However, when EG is the major solvent, such a phenomenon is supressed, and the dot diameter increases again when more EG is used. This could be explained by the fact that the change of viscosity is not that obvious when EG is the major solvent. So, a lower contact angle could result in a larger dot diameter again.

Regarding the effect of Triton, both the centre disk and the ring stains of dots in the same column (same EG/DI ratio) have been strengthened when the Triton loadings increased from 0.06 to 0.2 mg/ml, except the dots from a-3 to a-1. There is no centre disk in this column; only the strengthening of the ring stain could be observed when the Triton loading increased. The major difference among these three rows is the Triton loadings; the Triton loading increased from the bottom (row 3) to the top (row 1). As discussed before, the higher Triton loading could shorten the duration of the Marangoni effect as the surfactant could easily reach its CMC during evaporation. At the same time, the higher loading of Triton can improve the wetting of the droplet on the substrate, so the diameter of the droplet can be increased, and a lower contact angle can be obtained at the same time. Thus, the evaporation rate can be increased due to the reduced contact angle[165,166]. So, more Triton could be transported into the contact line area, and more DI water would evaporate from this area as well. Thus, the Marangoni effect could also be strengthened in this case. Theoretically, then, both the ring stain and centre disk should become more obvious when the Triton loading is higher (e.g., 0.2 mg/ml) compared to the dot with lower Triton loading. However, the Marangoni flow is stopped once the CMC is reached. The higher loading of Triton thus results in a shorter duration of the Marangoni effect. It is worth noting that although both the strength and duration of EG induced Marangoni flow should decrease when higher EG loading has been used[176], the centre disk could still be observed. This could be explained by a lesser volume loss in the cases of EG/DI > 0.5/1, so the surfactant-induced Marangoni effect could take effect in these cases and help the formation of the centre disk, as the surfactant-induced Marangoni effect lasted longer when the volume lost is less.

In all, the decreased Triton loading results in a strengthened Marangoni effect and an extended evaporation process due to the lower evaporation rate at high contact angle. When the higher Triton loading has been applied, both the CRE and Marangoni effect are strengthened due to the higher evaporation rate originating from the reduced contact angle.

As for the effect of EG loading, the increase in EG loading first shortens the duration of CRE in the case of DI dominated drying, so the ring-dominated structure is turned into a dual-ring structure with a depletion zone. Then, the EG becomes the major solvent as EG loading continues to increase. So, the CRE regains control of drying, and the dual-ring structure without a depletion zone is formed in this case.

Figure 45 shows formulations starting from ‘0.5rGO, 0.01/1EG, 0.2Tri’ (a-1). Then, the rGO loading was maintained at 0.5 mg/ml, the UV was kept at 0 min, and the platen temperature was 25 ºC. The EG loadings were set as 0.01/1, 0.05/1, 0.1/1, 0.5/1, and 1/1 by weight (labelled as a, b, c, d, and e, respectively). The Triton X-100 loadings were set as 0.2, 0.1, and 0.06 mg/ml (labelled as 1, 2, and 3, respectively). The values of W, R, and their ratios are shown in table 18.

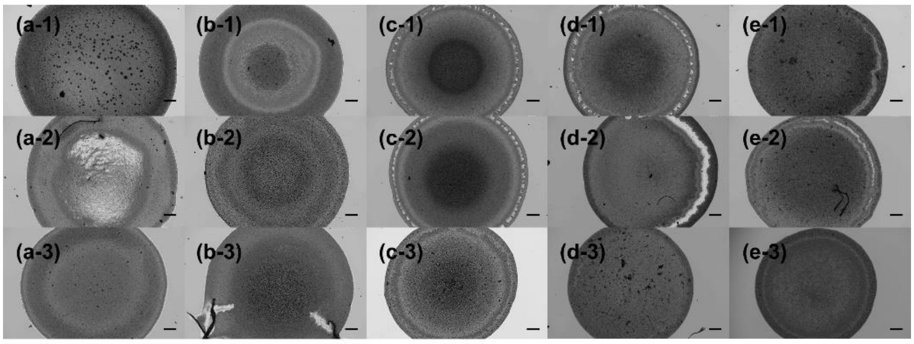

Figure 45 Optical microscope images of dried dots from inks of '0.5 rGO, 0.01/1 – 1/1 EG, 0.2 – 0.06 Tri'. As for the ink formulations, the EG/DI ratios change horizontally from 0.01/1 to 1/1 (a – e), and Triton loadings change vertically from 0.2 to 0.06 mg/ml (1 – 3), while the rGO loading is maintained at 0.5 mg/ml. The UV time and platen temperature for the substrate are held at 0 minutes and room temperature, respectively. The aim of this stage is to check the effects of rGO loading on the effects of a modifier on the droplet drying. Similar effects of Triton and EG have been found when rGO loading is changed from 0.1 to 0.5 mg/ml. In general, the lower Triton loading extends the duration of the surfactant-induced Marangoni effect to supress the CRE. The increase in the EG/DI ratio strengthens the Marangoni effect when the EG/DI ratio changes from 0.01/1 to 0.1/1, and then the dot CRE regains control of droplet drying when the EG/DI ratio is larger than 0.5/1. One of the major effects of increased rGO loading is the widening of structures like ring stains and centre disks, so the depletion zone can be supressed in this case. The other effect is that the duration of the surfactant-induced Marangoni effect can be extended as more Triton is absorbed by the rGO flakes. Thus, the depletion zone could be observed again in the droplet with EG/DI > 0.5/1. Black scale bar represents 200 µm.

	a1	b1	c1	d1	e1
W (µm)	174.49 ± 31.09	382.65 ± 36.97	85.71 ± 33.99	105.10 ± 23.78	95.92 ± 28.98
R (µm)	1.27×10^3 ± 39.78	1.14×10^3 ± 42.90	1.08×10^3 ± 41.23	1.06×10^3 ± 37.45	1.10×10^3 ± 40.90
W/R	0.12	0.33	0.10	0.08	0.09

	a2	b2	c2	d2	e2
W (µm)	80.1 ± 23.33	98.47 ± 29.09	54.08 ± 31.01	71.94 ± 27.67	95.41 ± 33.30
R (µm)	1.19×10^3 ± 41.09	1.13×10^3 ± 43.12	1.10×10^3 ± 42.27	1.07×10^3 ± 34.21	1.06×10^3 ± 41.21
W/R	0.07	0.09	0.07	0.05	0.09

	a3	b3	c3	d3	e3
W (µm)	70.92 ± 27.89	501.02 ± 29.13	75 ± 21.22	91.84 ± 4,01	113.78 ± 31.09
R (µm)	1.17×10^3 ± 37.26	1.17×10^3 ± 34.57	1.04×10^3 ± 38.98	0.99×10^3 ± 12.31	1.02×10^3 ± 46.66
W/R	0.06	0.43	0.07	0.09	0.11

Table 18 Values of W, R, and their ratios of the droplets dried from inks of ‘0.5 rGO, 0.01/1 – 1/1 EG, 0.06 – 0.2 Tri’ dried on a Si wafer treated with 0-min UV at room temperature. The dot radius of the above droplets generally decreases when more EG or less Triton have been loaded in the droplet. The one exception is that the dot radius is slightly increased when the EG/DI ratio increases from 0.5/1 to 1/1. The ring width of droplets changed dramatically, and no clear trend could be found when higher rGO loading was used, as more flakes decreased particle mobility.

Similar effects of EG and Triton on droplet drying uniformity have been found in figure 45 compared to the effects found in figure 44. From a – 1 to e – 1 in the same row, the dot diameter decreased from 1.27×10^3 ± 39.78 to 1.06×10^3 ± 37.45 at first when EG/DI changed from 0.01/1 to 0.5/1 and then slightly increased to 1.10×10^3 ± 40.90 µm as the EG loading increased. Similar trends could be found in all these three rows. Similarly, the width of all ring stains and centre disks become larger and more concentrated when more rGO is used. Talbot et al. found a similar phenomenon in their project as well[176], wherein higher particle loading resulted in a decrease in their mobility during drying and in the formation of wider ring stains and centre disks. This also increases the difficulty in distinguishing the width of the depletion zone between the ring stain and the centre disk and results in a suppression of the depletion zone as well.

In addition, another issue needs to be mentioned, which is the formation of the depletion zone in the droplets with EG > 0.5/1. As discussed before, the depletion zone is formed when the CRE duration is not long enough to push all the particles back to the edge when DI is the major solvent. However, this issue can be supressed when EG becomes the major solvent, as the CRE dominated by EG has a chance to push all the particles back due to its low vapour pressure and increased loading. However, since Triton is not only a surfactant but also a stabiliser to graphene[111], the higher rGO loading would absorb more Triton onto the graphene/liquid interface and result in a similar effect to using less Triton; this extends the duration to reach the CMC in the droplet. So, the surfactant-induced Marangoni effect on all droplets from figure 45 is strengthened in this case. Thus, more flakes should be transported back to the droplet centre due to this strengthened Marangoni effect. There is a chance that the resulting EG dominated CRE could not push all the flakes back to the edge again due to this increased flake loading, so the depletion zone could still be observed when the EG/DI ratio > 0.5/1. In addition, figure 45 shows that all dots in the first row, especially the dots with dual-ring structures, show more clear depletion zone in their structures compared to that of dots that have the same EG/DI ratio but less Triton loading. As mentioned in the previous section, the increased Triton loading results in a smaller surface tension of the droplet, so a smaller contact angle is obtained in this case. Then, the evaporation rate could be increased due to the reduced contact angle[165,166]. So, more Triton can be transported into the contact line area, and more DI water evaporates from this area as well. Thus, the Marangoni effect can also be strengthened in this case. So, both the ring stain and centre disk should become more obvious when Triton loading is higher. However, the Marangoni flow is stopped once the CMC is reached. Thus, the higher loading of Triton results in a shorter duration of the Marangoni effect.

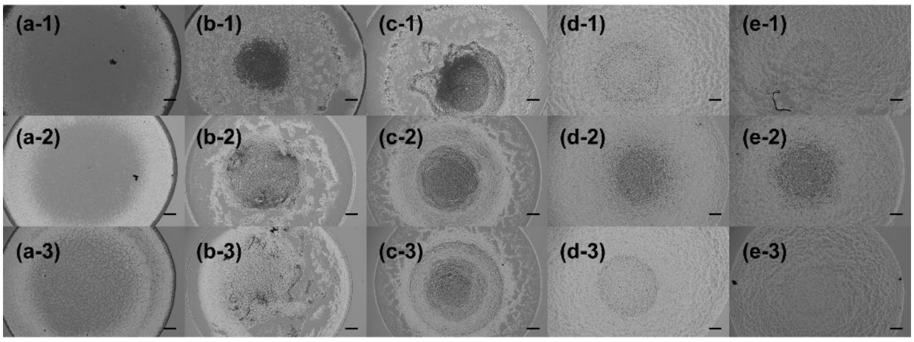

Figure 46 Optical microscope images of dried dots from inks of ‘0.1 rGO, 0.01/1 – 1/1 EG, 0.06 – 0.2 Tri’. As for the ink formulations, the EG/DI ratios change horizontally from 0.01/1 to 1/1 (a – e), and Triton loadings change vertically from 0.2 to 0.06 mg/ml (1 – 3), while the rGO loading is maintained at 0.1 mg/ml. The platen temperature for the substrate is kept at room temperature, while the UV time is changed from 0 to 20 minutes. The aim of this stage is to check the effects of UV time on the effects of modifiers on the droplet drying. Similar effects of Triton and EG have been found when UV time is changed from 0 to 20 minutes. In general, the longer UV time increases the hydrophilicity of the substrate, which results in all the droplets having much larger dot diameters compared to those droplets with 0-minute UV. The dot shapes changed from ring-dominated structures to dual-rings with a depletion zone when EG /DI increased from 0.01/1 to 0.1/1 and further changed into dual-ring structures without a depletion zone when EG/DI > 0.5/1. At the same time, the improved hydrophilicity decreases the droplet contact angle, so both the ring stain and centre disk can be strengthened in this case. Although the change of dot diameter between 0.06 and 0.2 mg/ml Triton is not that obvious due to improved substrate hydrophilicity, the strengthening of the ring stain and centre disk can still be observed in the case of 0.2 mg/ml Triton. Black scale bar represents 200 µm.

Figure 46 shows formulations starting from ‘0.1rGO, 0.01/1EG, 0.2Tri’ (a-1). Then, the rGO loading was maintained at 0.1 mg/ml, the UV was kept at 20 minutes, and the platen temperature was 25 ºC. The EG loadings were set as 0.01/1, 0.05/1, 0.1/1, 0.5/1, and 1/1 by weight (labelled as a, b, c, d, and e, respectively). The Triton X-100 loadings were set as 0.2, 0.1, and 0.06 mg/ml (labelled as 1, 2, and 3, respectively). The values of W and R and their ratios are shown in table 19.

	a1	b1	c1	d1	e1
W (µm)	85.71 ± 13.1	32.65 ± 10.01	38.78 ± 11.23	N/A	70.41 ± 13.21
R (µm)	1.48×10^{3} ± 21.22	1.46×10^{3} ± 22.28	1.44×10^{3} ± 25.18	N/A	1.72×10^{3} ± 22.43
W/R	0.06	0.02	0.03	N/A	0.04
	a2	**b2**	**c2**	**d2**	**e2**
W (µm)	57.14 ± 19.89	46.94 ± 11.90	28.57 ± 8.97	24.49 ± 10.06	46.94 ± 11.47
R (µm)	1.44×10^{3} ± 23.14	1.33×10^{3} ± 25.43	1.43×10^{3} ± 23.58	1.41×10^{3} ± 25.61	1.48×10^{3} ± 22.65
W/R	0.04	0.04	0.02	0.02	0.03
	a3	**b3**	**c3**	**d3**	**e3**
W (µm)	30.62 ± 17.71	18.37 ± 6.22	22.45 ± 11.21	16.33 ± 3.51	53.06 ± 11.15
R (µm)	1.31×10^{3} ± 21.31	1.31×10^{3} ± 19.89	1.33×10^{3} ± 23.77	1.41×10^{3} ± 21.78	1.34×10^{3} ± 23.78
W/R	0.02	0.01	0.02	0.01	0.04

Table 19 Values of W, R, and their ratios of the droplets dried from inks of ‘0.1 rGO, 0.01/1 – 1/1 EG, 0.06 – 0.2 Tri’ dried on a Si wafer with 20-mins UV at room temperature. The diameters of dots, which have EG/DI ratios > 0.5/1, are larger than the dots in the same row with the same Triton loading when 20-minutes UV was applied.

Similar effects of EG and Triton on the suppression of the CRE are observed in figure 46 compared to figure 44. The effect of EG on the droplet drying can be divided into two sections; one is from 0.01/1 to 0.1/1, and the other is from 0.5/1 to 1/1. In the first section, the CRE is continuously supressed as the EG loading increases. Hence, the duration of co-solvents induced Marangoni effect increases as a higher EG loading is used, and the dual-ring structure with a depletion zone can be formed in this case. In the meantime, the decreased Triton loading also supports the suppression of the ring stains. So, the CRE should be supressed from top to bottom.

The major differences are the sizes of the dots: those in columns 4 and 5 in figure 46 are much larger than the dots in the same row. As discussed before, when EG is the major solvent, the sudden change of viscosity due to the large loss in volume of DI is not that effective[164], so the increased EG loading results in a decrease in the contact angle and a larger dot diameter. However, in the case of the longer UV, the spreading of droplets seems to be strengthened more effectively.

In the meantime, the centre disk can still be observed in these six droplets, even with such a large dot diameter. The longer UV time improves the wettability of the substrate, and the spreading of the droplets with EG as their major solvent has been improved dramatically in this case. The main purpose of increasing UV time is to improve the hydrophilicity of the substrate surface. The droplet that lands on such a substrate would have a smaller contact angle and result in a larger dot diameter. Hence, the evaporation rate would be increased as the heat conduction from substrate to droplet has been enhanced[165,166]. So, this increased evaporation rate could result in a faster accumulation of Triton and evaporation of DI water at the contact line area and result in the strengthening of the surfactant-induced and co-solvents induced effects at the same time. However, this strengthening is different from the above case, which extends the duration of the surfactant-induced Marangoni effect. In this case, the strengthening is due to the faster evaporation, so the strengthening is more related to the strength of the Marangoni flow rather than the duration, as a higher surface tension difference can be created in this case due to the higher contact line evaporation rate[175,176]. Thus, the centre disks can still be observed even though dot diameter increased dramatically. However, while the ring stain could be observed, the ring stain did not become more serious in these six droplets. This indicates that the extent of the increased evaporation rates by UV and platen temperature is different. The longer UV time could not cause the EG evaporation rate to change dramatically, so the change of the Marangoni effect is more dramatic compared to that of the CRE. Thus, the centre disk can be strengthened, but the strengthening of CRE is not that obvious in this case.

Figure 47 shows formulations starting from ‘0.1rGO, 0.01/1EG, 0.2Tri’ (a-1). The rGO loading was maintained at 0.1 mg/ml, the UV was kept at 0 minutes, and the platen temperature was 60 ºC for all the above formulations. The EG loadings were set as 0.01/1, 0.05/1, 0.1/1, 0.5/1, and 1/1 by weight (labelled as a, b, c, d, and e, respectively). The Triton X-100 loadings were set as 0.2, 0.1, and 0.06 mg/ml (labelled as 1, 2, and 3, respectively). The values of W, R, and their ratios are shown in table 20.

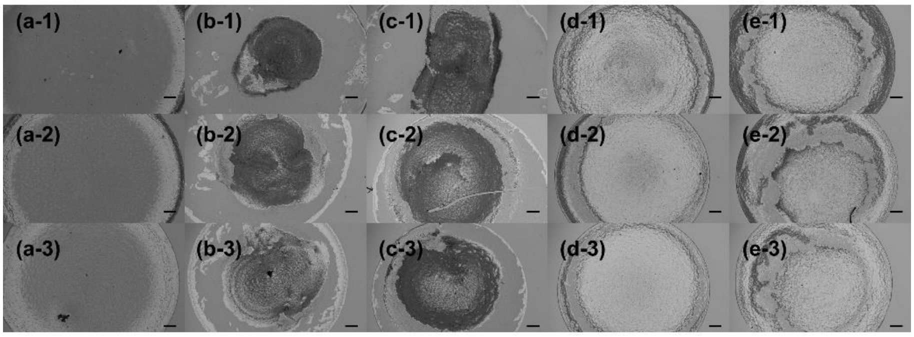

Figure 47 Optimisation of co-solvents and surfactant-induced Marangoni effects on inks of '0.1 rGO, 0.01/1 – 1/1 EG, 0.06 – 0.2 Tri' dried on a Si wafer treated with 0-mins UV Ozone at 60 °C. As for the ink formulations, the EG/DI ratios change horizontally from 0.01/1 to 1/1 (a – e), and the Triton loadings change vertically from 0.2 to 0.06 mg/ml (1 – 3), while the rGO loading is maintained at 0.1 mg/ml. The platen temperature for the substrate was changed from room temperature to 60 ℃, while the UV time was maintained at 0 minutes. The aim of this stage is to check the effects of the platen temperature on the effects of modifiers on the droplet drying. Similar effects of Triton and EG have been found when platen temperature has been changed from room temperature to 60 ℃. In general, the higher platen temperature increases the evaporation rate of the droplets dramatically, which results in all the droplets having both strengthened ring stains and depletion zones. The dot shapes change from a ring-dominated structure to a dual-ring with a depletion zone when EG /DI increases from 0.01/1 to 0.1/1. However, dots with EG/DI > 0.5/1 also have the dual-ring structure with a depletion zone when 60 ℃ platen temperature has been applied. Thus, the increased Triton loading can still strengthen both the CRE and Marangoni effect at the same time due to the reduced contact angle caused by the reduced surface tension. Black scale bar represents 200 µm.

	a1	**b1**	**c1**	**d1**	**e1**
W (µm)	117.86 ± 21.22	32.14 ± 11.10	61.22 ± 12.11	59.18 ± 13.37	178.06 ± 38.78
R (µm)	1.48×10^{3} ± 33.23	1.47×10^{3} ± 21.18	1.46×10^{3} ± 22.23	1.26×10^{3} ± 25.11	1.39×10^{3} ± 45.71
W/R	0.08	0.02	0.04	0.05	0.13
	a2	**b2**	**c2**	**d2**	**e2**
W (µm)	67.35 ± 12.20	71.43 ± 13.77	59.18 ± 12.34	97.96 ± 11.29	227.55 ± 34.54
R (µm)	1.48×10^{3} ± 25.38	1.50×10^{3} ± 26.68	1.49×10^{3} ± 28.17	1.22×10^{3} ± 27.65	1.27×10^{3} ± 46.77
W/R	0.05	0.05	0.04	0.08	0.18
	a3	**b3**	**c3**	**d3**	**e3**
W (µm)	328.57 ± 23.28	138.78 ± 11.29	54.59 ± 14.57	81.63 ± 4.55	358.67 ± 35.12
R (µm)	1.41×10^{3} ± 25.37	1.26×10^{3} ± 26.53	1.23×10^{3} ± 29.87	1.21×10^{3} ± 31.01	1.23 ± 32.28
W/R	0.23	0.11	0.04	0.07	0.29

Table 20 Values of W, R, and their ratios of the droplets dried from inks of '0.1 rGO, 0.01/1 – 1/1 EG, 0.06 – 0.2 Tri' on a Si wafer treated with 0-mins UV Ozone at 60 °C. The diameters of dots decreased with increasing EG/DI ratios from 0.01/1 to 0.5/1 but increased again when EG/DI ratio = 1/1. The dot diameter could be increased when a higher concentration of Triton has been used in the droplet.

Similar effects of EG and Triton on the suppression of the CRE have been observed in figure 47 compared to that of figure 44. However, this time, the depletion zone can be observed in the droplets with EG/DI ratio > 0.5/1. As discussed before, this dual-ring structure with a depletion zone could be explained by the shortened duration of the CRE only section, as it does not have enough time to transport all the flakes back to the edge before the droplet dries. In this section, the different degrees of increase of evaporation rate at the contact line by UV time and platen temperature are proved again.

At the same time, the effect of Triton loading can still be observed, as more Triton leads to a short duration of the surfactant-induced Marangoni effect, so there is no surface tension gradient when the loading of Triton reaches the CMC. Then, the CRE dominates the rest of the droplet drying, which results in a strengthened ring stain compared to the droplets with the same EG/DI ratio in the same column.

It is also worth noting that the strength of the thermally induced Marangoni effect is not in the same magnitude for the surfactant or co-solvents induced Marangoni effect[134]. So, the major effect of higher platen temperature is its enhancement of the droplet evaporation, as both Triton and EG exist in the droplet.

In all, the higher platen temperature strengthens the Marangoni effect and brings back the dual-ring structures with a depletion zone, even in droplets with EG/DI > 0.5/1. Thus, this would degrade the drying uniformity of droplets. However, as discussed in the previous sections, the high platen temperature is necessary because lower platen temperatures cause unexpected drying issues, such as a concentrated bottom caused by the Marangoni effect in the printed square.

In conclusion, the effects of modifier on the droplet drying uniformity can be summarised as follows:

(1) the decrease in Triton loading can extend the duration of the surfactant-induced Marangoni effect, as it would take a longer duration to reach the CMC during evaporation;

(2) the increase in Triton loading can reduce the surface tension of the droplet and result in a smaller contact angle of the droplet. Thus, the evaporation rate increases in the contact line area and results in a strengthening of CRE and Marangoni effect;

(3) the increase in EG loading divides the droplet drying into two categories. One is DI dominated drying, in which the increase of EG loading reduces the duration of the CRE only section, so the capillary flow does not have time to transport all the particles back to the edge; the dual-ring structure with depletion zone is formed in this case. The other is EG dominated drying, in which the increase of EG loading extends the duration of the CRE only section, so capillary flow can have enough time to transport particles back to the edge again; the dual-ring structure without a depletion zone is formed in this case;

(4) the effect of higher rGO loading is not obvious on the droplet drying, except that it can extend the duration of the surfactant-induced Marangoni effect and decrease the particle mobility (as seen by a wider ring satin and a larger centre disk in all formulations);

(5) the effects of longer UV time and higher platen temperature can both increase the evaporation rate of the droplets to different extents. So, both

can strengthen the CRE and Marangoni at the same time. However, the higher platen temperature reverts to the dual-ring structure with a depletion zone again, as it could shorten the drying of EG.

These conclusions are quite similar to what was found in the previous section (section 4.41), which proves the consistency of the findings on the used ranges of modifier loadings, rGO loadings, UV time, and platen temperatures. Thus, they are used as guidelines for the preparation of aimed inks in the coming section.

4.5 Inkjet printing of large rGO flakes

Four major drying issues were found in the inkjet printing of Ink 1-(0.25rGO, 0.1/1EG, 0.1Tri)-1.5μm in section 4.3, which are the CRE, first dot issue, missing front issue, and waviness.

As discussed before, the serious first dot issue can cause the rGO loadings in the first several dots to become higher than the rest of the dots in the same printing sequence. The additional rGO flakes results in an increase in the droplet surface tension, as they can absorb more Triton molecules in the droplets[111]. Then, the amount of Triton in the liquid/vapour interface lessens, and the droplet surface tension increases in this case. Then, the Laplace pressure in these first several droplets is higher than the main section of printed line[163]. Thus, a flow along the printing direction is formed and pushes the flakes along the printing direction to form the missing front.

As for the CRE and waviness issues, previous sections proved that the printer settings and substrate modifications (UV time and platen temperature) only have mild effects on their suppression. In addition, an unexpected drying issue happened when the platen temperature dipped below 60 °C, which was the concentrated bottom of printed square due to the Marangoni effect. In terms of the origin of the waviness issue, it comes from the dual-ring structure with a depletion zone in the dried dot. So, the inappropriate drop spacing was set based on the centre disk rather than the outer ring. Thus, the bulge issue could happen to the outer ring structure and result in the waviness issue while the line printed with the same drop spacing remained straight. Then, two major explorations were conducted in section 4.4 to find different factors' effects on droplet drying uniformity and to try to propose a guideline for the ink formulation that can avoid the dual-ring structure with a depletion zone.

Thus, another 6 inks were formulated based on Ink 1-(0.25rGO, 0.1/1EG, 0.1Tri)-1.5μm with the help of an initial guideline and optimised printer settings. The details of how to develop these seven inks are discussed in this section. Additionally, the rheological properties and Z numbers of these seven inks have been collected and added to the appendix (Table S1). In the meantime, the graphs of the surface tension and viscosity of these seven inks have been added to the Appendix and are shown in figures S3 and S4. All seven of these inks have Z numbers larger than 10, which are in the range of jetting satellites. The issue has been supressed by using a modified waveform developed in section 4.4.2, allowing all inks to be stably jetted out without any issues.

The Ink 1-(0.25rGO, 0.1/1EG, 0.1Tri)-1.5μm from section 4.3 has been used as the starting point for this section. The printer settings and substrate treatments used in this section are optimised combinations adopted from the conclusions drawn from section 4.3 for consistency:

(1) drop spacing: 200 μm for dots and radius of dried dot for lines and square;
(2) maximum printing frequency: 1 kHz;
(3) cartridge temperature: room temperature;
(4) platen temperature: 60 °C;
(5) UV time: 20 minutes for all substrates;
(6) Substrates: Si wafer for all inks, the glass and polyimide (PI) would be used for inks without major drying issues.

All the inks prepared and printed in this section include an extra filtration process with glass wool and a degassing process before they were loaded into the cartridge. The aim of this step is to supress the first dot issue and missing front issue[92].

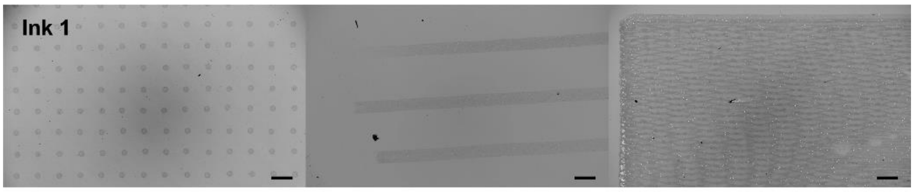

Figure 48 Printed dots, lines, and squares from Ink 1-(0.25rGO, 0.1/1EG, 0.1Tri)-1.5μm. The drop spacing = 200 μm for dots and 25 μm for lines and square; the MPF = 1kHz; and the cartridge and platen temperatures are room temperature and 60 °C, respectively. The first dot issue and missing front issue have been supressed with the help of additional filtration and degassing settings. However, the clear waviness issue can still be observed in the printed squares, which indicates the formation of a dual-ring structure with a depletion zone in the dried dots. Black scale bar represents 200 μm.

As figure 48 shows, the first dot issue and missing front issue have been supressed after the extra filtration and degassing process. This also proves the previous conclusion in section 4.3 that the missing front issue stems from the first dot issue.

Based on the printed dots and lines from figure 48, the average dot diameter is ~52.07 ± 1.22 µm, and the average line is ~115.28 ± 2.13 µm. The line width in the square is ~66.64 ± 1.27 µm, which means that individual printed lines have a larger average width than the average line width in the square. However, the actual width of the line in the square is at least double its appeared width. This is because half of the printed line in the square has been covered by the line printed next to it.

Ink 1-(0.25rGO, 0.1/1EG, 0.1Tri)-1.5µm has Triton loading of about 0.1 mg/ml and an EG/DI ratio of about 0.1/1, the UV time for the substrate is 20 minutes, and the platen temperature is 60 ℃. Based on previous explorations, the major solvent should be DI water-based on its EG/DI ratio, and the 20 minutes UV time and high platen temperature would increase the evaporation rate at the contact line area dramatically. So, both the surfactant and co-solvents induced Marangoni effects would be strengthened at the same time. In the meantime, this increase in the evaporation rate further decreases the duration of CRE, which further helps the formation of the dual-ring structure with a depletion zone. This also explains why the printer settings and substrate modifications could only have mild effects on the suppression of the waviness issue.

As the exploration section discussed, extending the duration of the CRE to the whole droplet drying process is an effective way to supress the depletion zone. In order to take advantage of the co-solvents induced Marangoni effect at the same time, an ink (Ink 2) with more EG loading was prepared. Although the droplet with the best drying uniformity was obtained by using the EG/DI ratio = 0.5/1, the droplet was dried on the substrate treated with 0-minute UV at room temperature. Thus, the EG/DI ratio = 1/1 was selected for the preparation of Ink 2, and the formulation of this ink is Ink 2-(0.25rGO, 1/1EG, 0.1Tri)-1.5µm.

At the same time, using lower platen temperature is also a route to extending the duration of the CRE, as the evaporation rate in the contact line can be decreased in this case. However, the previous result in section 4.3.2 proved that using lower platen temperature would instigate other unexpected drying issues in the printed films. This should be avoided.

In addition, as discussed in the exploration section, although the increase of rGO loading could extend the duration of the surfactant-induced Marangoni effect, it has a chance to reduce the mobility of particles during the drying and widen both the ring stain and centre disk. This is another way to supress the depletion zone. Thus, Ink 3 has been prepared based on Ink 2-(0.25rGO, 1/1EG, 0.1Tri)-1.5µm in this step, and the formulation is Ink 3-(0.5rGO, 1/1EG, 0.2Tri)-1.5µm. It is worthy to note that Triton of Ink 3-(0.5rGO, 1/1EG, 0.2Tri)-1.5µm has been increased from 0.1 to 0.2 mg/ml, as the ink with 0.1 mg/ml Triton could not be jetted out.

Figure 49 shows the printed dots, lines, and thin film based on the optimised printer settings and substrate treatments from Ink 2-(0.25rGO, 1/1EG, 0.1Tri)-1.5µm and Ink 3-(0.5rGO, 1/1EG, 0.2Tri)-1.5µm. The dot diameter and line width of Ink 2-(0.25rGO, 1/1EG, 0.1Tri)-1.5µm are 48.98 ± 1.15 and 81.63 ± 2.21 µm, respectively. The waviness issue was supressed in the printed square. However, the concentrated bottom was formed in this case. This could be explained by the low vapour pressure of EG, which leads to a long drying process, even with platen temperature set at 60 °C. The printed square dried as a thin film rather than individual lines. In such a thin film, the top part was printed and dried first. Thus, less DI is in this part and results in a smaller surface tension.

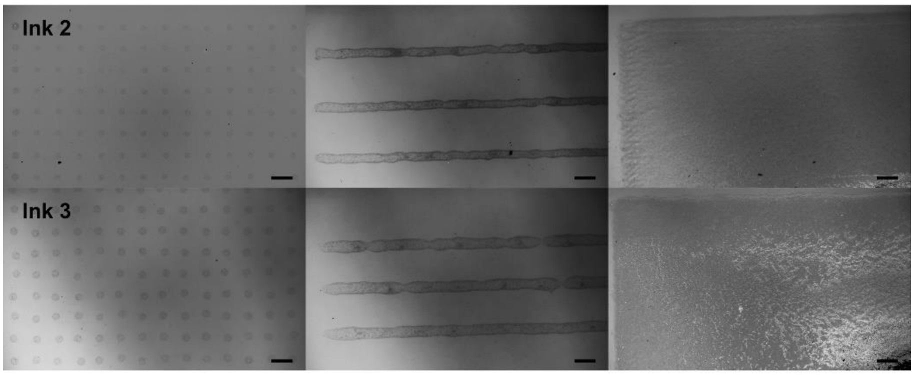

Figure 49 Printed dots, lines, and squares from Ink 2-(0.25rGO, 1/1EG, 0.1Tri)-1.5µm and Ink 3-(0.5rGO, 1/1EG, 0.2Tri)-1.5µm. The drop spacing = 200 µm for dots, and 24 and 35 µm for lines and squares; the MPF = 1kHz; and the cartridge and platen temperatures are room temperature and 60 °C, respectively. The higher EG loading and rGO loading were used to extend the duration of the CRE and decrease the particle mobility, respectively. Although, the waviness issue in the squares have been supressed, the concentrated bottom issue happened, which severely degraded the pattern drying uniformity. Black scale bar represents 200 µm.

Consequently, a surface tension gradient was formed and induced a Marangoni flow form the top to the bottom of the square and transported the rGO to the bottom[134]. The same drying issue happened to Ink 3-(0.5rGO, 1/1EG, 0.2Tri)-1.5µm as well, the decrease of particle mobility may help the suppression of the depletion zone, but the concentrated bottom degrades the pattern drying uniformity severely.

It is worthy to note that the dot diameter and line width of Ink 3-(0.5rGO, 1/1EG, 0.2Tri)-1.5µm are 70.41 ± 2.33 and 97.96 ± 2.67 µm, respectively. The increase of these two values from Ink 2-(0.25rGO, 1/1EG, 0.1Tri)-1.5µm to Ink 3-(0.5rGO, 1/1EG, 0.2Tri)-1.5µm can be attributed to the increase of Triton loading in Ink 3-(0.5rGO, 1/1EG, 0.2Tri)-1.5µm.

In all, although the higher EG loading can supress the waviness issue, the increased EG loading introduces other drying issues in the printed square. Further modification on the ink formulation is still needed.

Thus, another way of extending the duration of the CRE was tried using DI as the major solvent. Since there is major difference in the vapour pressures between EG and DI water[176], there would be only DI water in the new ink formulated at this step to ensure the duration of the CRE is long enough. Ink 4 was designed based on Ink 3-(0.5rGO, 1/1EG, 0.2Tri)-1.5µm; the formulation is Ink 4-(0.5rGO, 0/1EG, 0.2Tri)-1.5µm. Thus, the main competition between the internal flow has been changed from surfactant and co-solvents induced Marangoni flows vs. capillary flow to the surfactant-induced Marangoni flow vs. the capillary flow. Since there is only one solvent in the droplet, the CRE would not be stopped until the droplet dried. Thus, the uniformity of the final dried pattern is decided by the competition between these two flows. As mentioned before, there are two types of factors could affect the strength and duration of surfactant-induced Marangoni flow during the droplet drying[134,175,176]. One is the factors that alter the evaporation rate of the droplet contact line area, like UV time, platen temperature, and so forth. The other type is the factors that affect the duration of the droplet to reach the CMC, like Triton loading and rGO loading, among others. So, there are numerous ways to find the balance between these two flows. However, since the aim of this project is to prepare large rGO water-based ink for FTEs, the addition of less additives and more graphene loadings in the ink is preferred in the premise of ink printability of prepared ink. Thus, Ink 5 has been designed based on Ink 4-

(0.5rGO, 0/1EG, 0.2Tri)-1.5µm with higher rGO loading. The formulation is Ink 5-(1rGO, 0/1EG, 0.2Tri)-1.5µm.

Figure 50 shows printed patterns from Ink 4-(0.5rGO, 0/1EG, 0.2Tri)-1.5µm under the optimised printer settings and substrate treatments. The dot diameter and line width for Ink 4-(0.5rGO, 0/1EG, 0.2Tri)-1.5µm are 54.08 ± 2.18 and 66.33 ± 2.31 µm, respectively. The CRE became more serious, especially in the printed lines. Thus, the CRE is too strong in this case. At the same time, based on the conclusions from section 4.4, both an increase in rGO loading and a decrease in Triton loading could extend the duration of surfactant-induced Marangoni effect. So, a stronger Marangoni effect should be seen, as a higher loading of rGO was selected in this case; this does not match the dried dots from figure 50. A dual-ring structure could be seen in the dried dots from Ink 5-(1rGO, 0/1EG, 0.2Tri)-1.5µm. The addition of more rGO consumed the Triton molecules in the droplet, resulting in a strengthened surfactant-induced Marangoni effect. This explains why the clear multi-ring structure could be observed in the final dots. So, the results indicate that the Marangoni effect is too strong in this case, and the balance between CRE and S-ME has not yet been found.

Then, a new ink was formulated based on Ink 5-(1rGO, 0/1EG, 0.2Tri)-1.5µm, but with more Triton. The formulation of this ink is Ink 6-(1rGO, 1/1EG, 0.3Tri)-1.5µm.

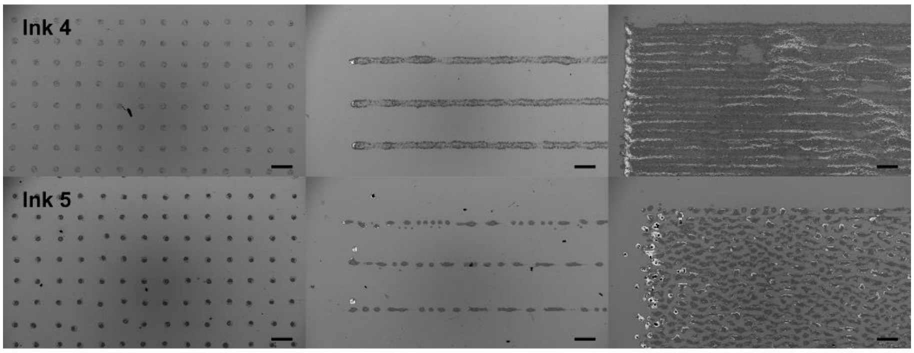

Figure 50 Printed dots, lines, and squares from Ink 4-(0.5rGO, 0/1EG, 0.2Tri)-1.5µm and Ink 5-(1rGO, 0/1EG, 0.2Tri)-1.5µm. The drop spacing = 200 µm for dots and 27 and 29 µm for lines and squares; the MPF = 1kHz; and the cartridge and platen temperatures are room temperature and 60 °C, respectively. The EG was fully removed from the ink, and the DI water is the only solvent in the ink. The competition between internal flows is the capillary flow vs. the surfacing induced Marangoni flow. The printed patterns indicate that CRE dominates during the drying of Ink 4-(0.5rGO, 0/1EG, 0.2Tri)-1.5µm, while a stronger surfactant-induced Marangoni effect was observed from Ink 5-(1rGO, 0/1EG, 0.2Tri)-1.5µm. Black scale bar represents 200 µm.

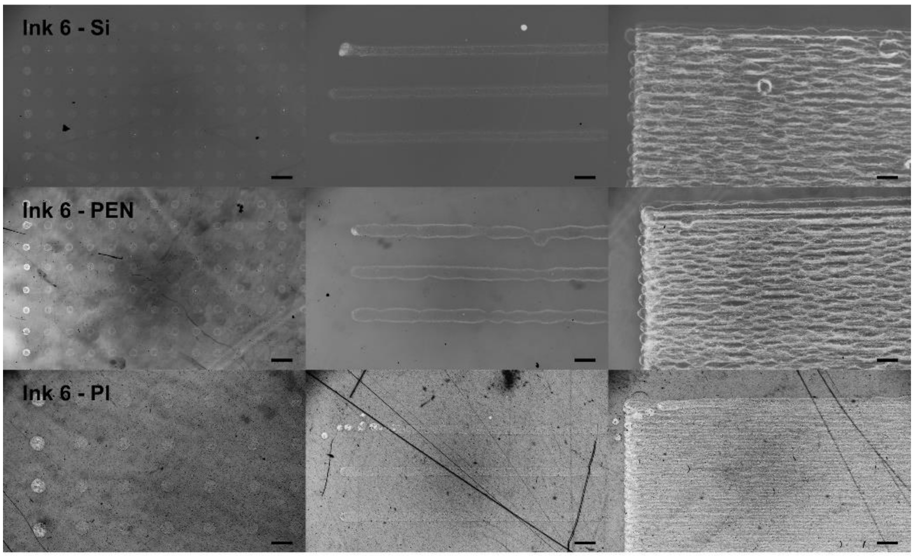

Figure 51 Printed dots, lines, and squares from Ink 6-(1rGO, 0/1EG, 0.3Tri)-1.5µm. The drop spacing = 200 µm for dots, and 45, 50, and 32 µm for lines and square on Si, PEN, and PI, respectively; the MPF = 1kHz; and the cartridge and platen temperatures are room temperature and 60 °C, respectively. The increased Triton loading has brought the balance between the CRE and Marangoni effect in the final printed patterns. No major drying issues are found in the printed patterns and the ink is printed on transparent and flexible substrates to check whether this result applies to substrates beyond Si wafer. Black scale bar represents 200 µm.

Figure 51 shows the printed patterns of Ink 6-(1rGO, 0/1EG, 0.3Tri)-1.5µm on various substrates. The ink is formulated based on Ink 5-(1rGO, 0/1EG, 0.2Tri)-1.5 µm but with higher Triton loading. The dot diameter and line width are 89.80 ± 2.27 and 125.51 ± 4.22 µm on Si wafer, 79.59 ± 2.78 and 114.29 ± 3.25µm on PEN, and 63.78 ± 2.01and 71.43 ± 1.19 µm on PI.

The dots, lines, and squares were uniformly printed. The major drying issues were supressed. The balance between the CRE and Marangoni effect was reached. Ink 5-(1rGO, 0/1EG, 0.2Tri)-1.5µm showed a strong surfactant-induced Marangoni effect during the drying; in order to supress this Marangoni effect, more Triton was used in the formulation of Ink 6. Thus, the Triton makes it easier to reach the CMC as the evaporation progresses. Then, the Marangoni effect was supressed in this case. It is worth noting that this is not the only way to find a balance between the CRE and S-ME. In addition, the previous exploration proves that more Triton results in a decrease in the contact angle and results in an acceleration of the evaporation rate. Then, both CRE and ME would be strengthened, which could lead to the formation of a depletion zone again. However, this is a conclusion based on the presence of EG in the solvent system, where the CRE still exists when one solvent has been fully evaporated. Then, the duration of the rest of the

CRE would decide whether a depletion zone forms or not. However, there is only water in Ink 6-(1rGO, 0/1EG, 0.3Tri)-1.5μm, which could avoid the above issue. Finally, an ink with same formulation of Ink 6-(1rGO, 0/1EG, 0.3Tri)-1.5μm but with larger rGO flakes has been prepared and named Ink 7-(1rGO, 0/1EG, 0.3Tri)-6.5μm.

Figure 52 shows that the dot diameter and line width are 67.35 ± 2.73 and 78.57 ± 3.69 μm. The patterns are relatively uniform, and the major drying issues have been supressed. However, the jetting stability and pattern regularity have been downgraded. Moreover, the large flake has also brought a storage stability issue. The printhead usually blocked after 3 – 5 days of storage.

Finally, since the ink without any drying issues has been formulated, a series of sheet resistance measurements on the printed squares based on Ink 6-(1rGO, 0/1EG, 0.3Tri)-1.5μm was conducted and is shown in figure 53.

Ink 6-(1rGO, 0/1EG, 0.3Tri)-1.5μm were printed on various substrates (Si, PEN, and PI) to evaluate its electrical properties. The 5 cm x 5 cm squares with various repeated prints (1 to 30 prints) were printed on these substrates. The sheet resistances of the printed squares were measured by the 4-probe method.

The sheet resistances of all printed squares under room temperature and annealed at 60 °C for 1 hour were collected and are shown in figure 53 (a) and (b). Then, the sheet resistances of the printed squares on Si and PI annealed at 120 °C for 1 hour are shown in figure 53 (c).

The higher annealing temperature improved the electrical property of the printed film. The smallest sheet resistance is 252.52 ± 0.19 kΩ/□, which is the result from the square with 30 prints on the PI after 1 hour of 120 °C annealing.

As the results indicate, the electrical properties of printed film from Ink 6 are not ideal. This could be mainly caused by the higher loading of Triton in Ink 6.

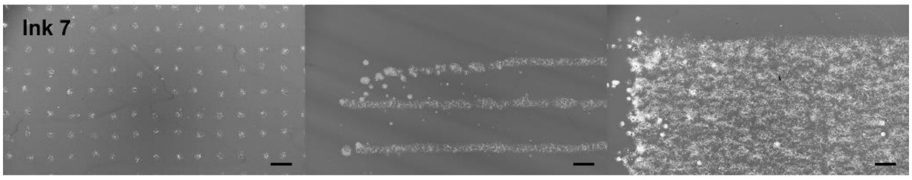

Figure 52 Printed dots, lines, and squares from Ink 7-(1rGO, 0/1EG, 0.3Tri)-6.5μm. The drop spacing = 200 μm for dots and 34 μm for lines and squares; the MPF = 1kHz; and the cartridge and platen temperatures are room temperature and 60 °C, respectively. The use of a large rGO flake size has degraded the printability of the prepared ink. Although there are no major drying issues in the printed patterns, the accuracy and uniformity of these patterns are not ideal. Black scale bar represents 200 μm.

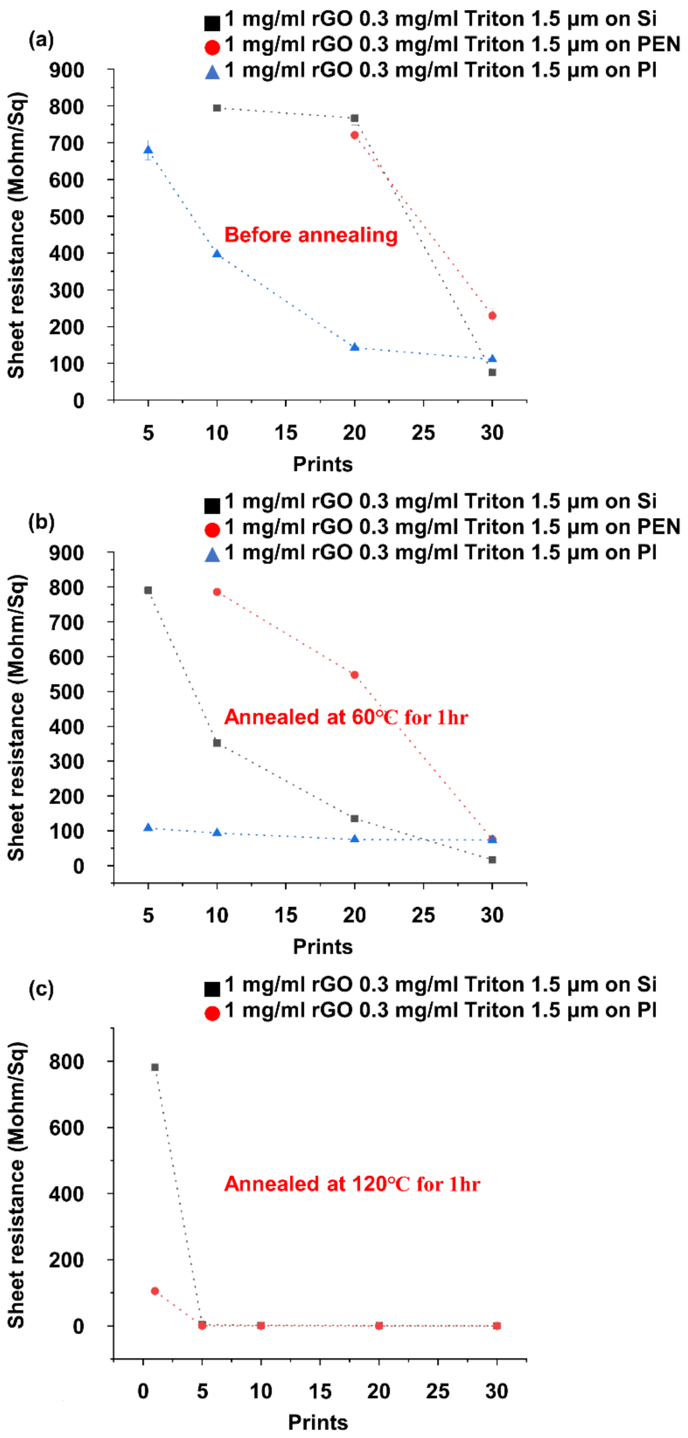

Figure 53 Sheet resistance of Ink 6-(1rGO, 0/1EG, 0.3Tri)-1.5µm on various substrates before and after annealing; (a) shows the sheet resistances of printed squares from Ink 6-(1rGO, 1/1EG, 0.3Tri)-1.5µm on Si wafer, PEN, and PI with different printed layers (prints) before thermal annealing; (b) shows the sheet resistance of printed squares of the same samples after thermal annealing at 60 °C for 1 hour; (c) shows the sheet resistance of printed squares of samples from (b) on Si wafer and PI that went through an additional thermal annealing at 120 °C for 1 hour. The smallest sheet resistance is 252.52 ± 0.19 kΩ/□, which is the result from square sheets with 30 prints on PI after 1 hour of 120 °C annealing.

In all, although the electrical property of the formulated Ink 6-(1rGO, 0/1EG, 0.3Tri)-1.5μm is not ideal, a large rGO water-based ink has been formulated and successfully printed without major drying issues. This is the first time that such water-based ink with such large rGO flakes has been formulated. This achievement directly proves the printability of high-resolution FTEs with large rGO flakes. At the same time, it is worth noting that Ink 6 is not the only option for the final printable ink. There could be other ways of find the balance between the surfactant-induced Marangoni effect and CRE. However, this section revels important challenges that need to be confronted for the preparation of large rGO water-based inks with acceptable drying uniformity in the future.

At the beginning, Ink 1-(0.25rGO, 0.1/1EG, 0.1Tri)-1.5μm was prepared based on the reported similar inks [18,74]. Four major drying issues were found during the printing of Ink 1-(0.25rGO, 0.1/1EG, 0.1Tri)-1.5μm. The first dot issue and missing front issue were supressed via using extra filtration and a degassing process. However, the CRE and waviness issues remained. Since the waviness is believed to be caused by the dual-ring structure with a depletion zone, different inks were prepared to supress this depletion zone. Although the issue has been fixed by increasing the EG loading in the droplet, this solution brings the concentrated bottom issue to the printed square, which is not acceptable to pattern drying uniformity. It is interesting to point out that such an issue happens to Ink 1-(0.25rGO, 0.1/1EG, 0.1Tri)-1.5μm when the platen temperature falls below 60 ℃ as well, and it is believed that this is caused by the low vapour nature of EG. Thus, this revels that although the EG/DI binary system could bring the co-solvents induced Marangoni effect to compete with the CRE, this system could easily bring in dual-ring structures with a depletion zone to the dried dots or lead to a long drying process of the printed square. The former would cause the waviness issue in the printed squares, while the latter would bring the concentrated bottom issue to the printed squares. Although the ink could dry uniformly by using the surfactant-induced Marangoni effect only, this is important to highlight this fact clearly, as many researchers believe the EG/DI an effective method to supress the CRE in the dried droplets [134]. However, there is a gap between the uniformly dried dot and printed continuous patterns.

In addition, since the reported GNP and GO inks [18,74] do not have such issues, it is important to note the reason behind that. As for the former one, although the ink has similar formulation to the ones used in this project, the xanthan gum has been used as the binder control the re-dispersion of particles on the interface during the drying process. Thus, no waviness has been observed. In terms of the latter, although some dual-ring structures with a depletion zone can be observed in the droplet with 2 µm flakes, the ultra-large GO flakes could effectively cover the depletion zone. Hence, no such waviness issue was observed in that project, either. Regarding this project, as previously discussed, the particles have a hydrophilic surface and strong interactions with other interfaces. In other words, the transportation of these flakes is strongly influenced by the internal flows. Thus, the dual-ring structure with a depletion zone causes this unique waviness in this project.

All in all, this project provides new insight into the important factors for the preparation of similar inks in the future.

Chapter 5. Conclusion and future work

As mentioned at the beginning, there are numerous types of inkjet printable water-based graphene inks. The most commonly used materials are GNP and GO. GNP has advantages in its electrical properties, but the use of stabilisers and limitations on flake size are disadvantages[13]. By contrast, GO boasts large flake sizes and superior dispersibility in water; this gives it an advantage in reducing the contact resistance among the flakes and simplicity in ink preparation[13]. However, the reduction process limits the available range of flexible and transparent substrates, which is not an ideal option for printing FTEs.

In this project, an inkjet printable large rGO water-based ink (Ink 6-(1rGO, 0/1EG, 0.3Tri)-1.5µm) has been successfully formulated and printed without major drying issues. This is the first time that a water-based ink with large rGO flakes (~1.5 µm) is printed from a nozzle with a diameter of ~21.5 µm. This ink offers two major advantages for the preparation of inkjet-printed FTEs:

(1) less contact resistance due to the large rGO flakes;

(2) a simple annealing process, which broadens the available range of flexible and transparent substrates, as no further reduction is needed.

Although the electrical conductivity of the final printed thin film is not ideal, the successful printing of such an ink still contributes insight into potential methods for future inkjet-printed FTEs.

Three key steps were taken to prepare this inkjet printable large rGO water-based ink.

In the first step, Ink 1-(0.25rGO, 0.1/1EG, 0.1Tri)-1.5μm was prepared based on reported similar inks[18,74]. Four major drying issues were found during its printing. Two of them – the CRE and the first dot issue – are common issues; the other two are unique and include the missing front issue and the waviness issue. A series of different printer settings and substrate modifications were applied to explore these issues, and the reasons behind the two unique drying issues were discovered to be the first dot issue and a dual-ring structure with a depletion zone in a dried dot, respectively. The former could be suppressed by the extra filtration and degassing process[92], but the latter requires the ink to be reformulated.

In the second step, a series of explorations on the effects of individual factors (loadings of Triton, EG, rGO, UV time, and platen temperature) and the comprehensive effects of modifiers (mixture of Triton, EG, and DI) have been conducted to study how they influence the droplet drying. The conclusions are as follows:

(1) the decrease in Triton loading could extend the duration of the surfactant-induced Marangoni effect, as it takes a longer duration to reach the CMC during evaporation;

(2) the increase in Triton loading reduces the surface tension of droplets and results in a smaller contact angle of the droplet. Thus, the evaporation rate would increase in the contact line area, which results in a strengthening of CRE and the Marangoni effect;

(3) the increase in EG loading divides the droplet drying into two categories. One is DI dominated drying, in which the increase of EG loading reduces the duration of the CRE only section, so the capillary flow does not have time to transport all the particles back to the edge, and the dual-ring structure with a depletion zone is formed in this case. The other is EG dominated drying, in which the increase of EG loading extends the duration of the CRE only section, so the capillary flow has enough time to

transport particles back to the edge again, and the dual-ring structure without a depletion zone is formed in this case;

(4) the effect of higher rGO loading on the droplet drying is not obvious, except that it could extend the duration of surfactant-induced Marangoni effect and decrease the particle mobility (wider ring satin and larger centre disk in all formulations);

(5) the effects of longer UV time and higher platen temperature both increase the evaporation rate of droplets by different extents, thus strengthening the CRE and Marangoni at the same time. However, higher platen temperature could further return the dual-ring structure with a depletion zone, as it shortens the drying of EG.

These conclusions have been used to guide the formulation of inks in the final step. In addition, it has been found that letting the duration of the coffee ring effect dominate the droplet drying will be an effective way to find the equilibrium point, rather than changing the strength of the capillary or Marangoni flow.

In the third step, seven inks have been prepared based on Ink 1-(0.25rGO, 0.1/1EG, 0.1Tri)-1.5µm and the conclusions above. Although the final ink (Ink 6-(1rGO, 0/1EG, 0.3Tri)-1.5µm) has been successfully printed without drying issue, the most important finding in this step is the gap between the uniformly dried droplet and the uniformly dried printed continuous pattern (e.g., square). Although the droplet dried uniformly following the above guideline, the printed square from the same ink with the same printer settings and substrate modifications exhibited serious concentrated bottom issues. Then, Ink 6-(1rGO, 0/1EG, 0.3Tri)-1.5µm discarded the co-solvents induced Marangoni effect to achieve the balance between CRE and Marangoni effect. It is worth noting that Ink 6-(1rGO, 0/1EG, 0.3Tri)-1.5µm is not the only possible formulation of large rGO water-based inkjet printable ink; more formulations or substrate treatments could be used or applied as long as the balance between CRE and Marangoni effect is achieved as the premise of printability.

In terms of future work, all the printable inks in this project have a Z number larger than 10 due to their high surface tension and low viscosity. By using the modified waveform, the ink with such rheological properties and large flakes could be stably jetted out. Thus, there is a possibility to print large rGO water-based inks without the addition of EG or Triton by further modifying the waveform. In the meantime, the viscosity could be controlled by using larger flakes or higher rGO loading in the future. So, a series of inks with larger rGO flakes and water only could be prepared in the future. The start point could be Ink 6-(1rGO, 0/1EG, 0.3Tri)-1.5µm with the optimised printer settings and substrate modifications. The main conflicts would be optimisation of rGO loading and average flake size via waveform. Since most of the stabilisers are insulating materials, the addition of Triton would further degrade the electrical conductivity of the final ink, then the advantage of using larger flakes to reduce the contact resistance is not obvious. If this proposal is achieved, then there will be a new future for graphene-based inkjet-printed FTEs.

Reference

1. Novoselov, K. S. *et al.* Electric Field Effect in Atomically Thin Carbon Films. *Science* **306**, 666–669 (2004).
2. Wan, X., Huang, Y. & Chen, Y. Focusing on Energy and Optoelectronic Applications: A Journey for Graphene and Graphene Oxide at Large Scale. *Acc. Chem. Res.* **45**, 598–607 (2012).
3. Lee, C., Wei, X., Kysar, J. W. & Hone, J. Measurement of the Elastic Properties and Intrinsic Strength of Monolayer Graphene. *Science* **321**, 385–388 (2008).
4. Balandin, A. A. *et al.* Superior Thermal Conductivity of Single-Layer Graphene. *Nano Lett.* **8**, 902–907 (2008).
5. Mayorov, A. S. *et al.* Micrometer-Scale Ballistic Transport in Encapsulated Graphene at Room Temperature. *Nano Lett.* **11**, 2396–2399 (2011).
6. Nair, R. R. *et al.* Fine Structure Constant Defines Visual Transparency of Graphene. *Science* **320**, 1308–1308 (2008).

7. Kaur, M., Kaur, M. & Sharma, V. K. Nitrogen-doped graphene and graphene quantum dots: A review onsynthesis and applications in energy, sensors and environment. *Adv. Colloid Interface Sci.* **259**, 44–64 (2018).

8. Kumar, A., Sharma, K. & Dixit, A. R. A review of the mechanical and thermal properties of graphene and its hybrid polymer nanocomposites for structural applications. *J. Mater. Sci.* **54**, 5992–6026 (2019).

9. Nag, A., Mitra, A. & Mukhopadhyay, S. C. Graphene and its sensor-based applications: A review. *Sens. Actuators Phys.* **270**, 177–194 (2018).

10. Schwierz, F. Graphene transistors. *Nat. Nanotechnol.* **5**, 487–496 (2010).

11. Zhang, Z. *et al.* Graphene-Based Mixed-Dimensional van der Waals Heterostructures for Advanced Optoelectronics. *Adv. Mater.* **31**, 1806411 (2019).

12. Torrisi, F. & Carey, T. Graphene, related two-dimensional crystals and hybrid systems for printed and wearable electronics. *Nano Today* **23**, 73–96 (2018).

13. Tran, T. S., Dutta, N. K. & Choudhury, N. R. Graphene inks for printed flexible electronics: Graphene dispersions, ink formulations, printing techniques and applications. *Adv. Colloid Interface Sci.* **261**, 41–61 (2018).

14. Gao, M., Li, L. & Song, Y. Inkjet printing wearable electronic devices. *J. Mater. Chem. C* **5**, 2971–2993 (2017).

15. Ago, H. CVD Growth of High-Quality Single-Layer Graphene. in *Frontiers of Graphene and Carbon Nanotubes: Devices and Applications* (ed. Matsumoto, K.) 3–20 (Springer Japan, 2015). doi:10.1007/978-4-431-55372-4_1.

16. Marcano, D. C. *et al.* Improved Synthesis of Graphene Oxide. *ACS Nano* **4**, 4806–4814 (2010).

17. Yi, M. & Shen, Z. A review on mechanical exfoliation for the scalable production of graphene. *J. Mater. Chem. A* **3**, 11700–11715 (2015).

18. He, P. & Derby, B. Inkjet printing ultra-large graphene oxide flakes. *2D Mater.* **4**, 021021 (2017).

19. Jabari, E. *et al.* 2D printing of graphene: a review. *2D Mater.* **6**, 042004 (2019).

20. De, S. & Coleman, J. N. Are There Fundamental Limitations on the Sheet Resistance and Transmittance of Thin Graphene Films? *ACS Nano* **4**, 2713–2720 (2010).

21. Huang, L., Huang, Y., Liang, J., Wan, X. & Chen, Y. Graphene-based conducting inks for direct inkjet printing of flexible conductive patterns and their applications in electric circuits and chemical sensors. *Nano Res.* **4**, 675–684 (2011).

22. Dreyer, D. R., Todd, A. D. & Bielawski, C. W. Harnessing the chemistry of graphene oxide. *Chem. Soc. Rev.* **43**, 5288–5301 (2014).

23. Garg, B., Bisht, T. & Ling, Y.-C. Graphene-Based Nanomaterials as Heterogeneous Acid Catalysts: A Comprehensive Perspective. *Molecules* **19**, 14582–14614 (2014).

24. Dreyer, D. R., Park, S., Bielawski, C. W. & Ruoff, R. S. The chemistry of graphene oxide. *Chem. Soc. Rev.* **39**, 228–240 (2009).

25. Lerf, A., He, H., Forster, M. & Klinowski, J. Structure of Graphite Oxide Revisited. *J. Phys. Chem. B* **102**, 4477–4482 (1998).

26. Erickson, K. *et al.* Determination of the Local Chemical Structure of Graphene Oxide and Reduced Graphene Oxide. *Adv. Mater.* **22**, 4467–4472 (2010).
27. Brodie, B. C. XIII. On the atomic weight of graphite. *Philos. Trans. R. Soc. Lond.* **149**, 249–259 (1859).
28. Staudenmaier, L. Process for the preparation of graphitic acid. *Ber Dtsch Chem Ges* **31**, 1481–1487 (1898).
29. Hofmann, U. & König, E. Untersuchungen über Graphitoxyd. *Z. Für Anorg. Allg. Chem.* **234**, 311–336 (1937).
30. Hummers Jr, W. S. & Offeman, R. E. Preparation of graphitic oxide. *J. Am. Chem. Soc.* **80**, 1339–1339 (1958).
31. Kovtyukhova, N. I. *et al.* Layer-by-Layer Assembly of Ultrathin Composite Films from Micron-Sized Graphite Oxide Sheets and Polycations. *Chem. Mater.* **11**, 771–778 (1999).
32. Zhao, J., Pei, S., Ren, W., Gao, L. & Cheng, H.-M. Efficient Preparation of Large-Area Graphene Oxide Sheets for Transparent Conductive Films. *ACS Nano* **4**, 5245–5252 (2010).
33. Wang, S. J., Geng, Y., Zheng, Q. & Kim, J.-K. Fabrication of highly conducting and transparent graphene films. *Carbon* **48**, 1815–1823 (2010).
34. Dimiev, A. M. & Tour, J. M. Mechanism of Graphene Oxide Formation. *ACS Nano* **8**, 3060–3068 (2014).
35. Ogino, I., Yokoyama, Y., Iwamura, S. & Mukai, S. R. Exfoliation of Graphite Oxide in Water without Sonication: Bridging Length Scales from Nanosheets to Macroscopic Materials. *Chem. Mater.* **26**, 3334–3339 (2014).

36. Hutchings, I. M. & Martin, G. D. *Inkjet technology for digital fabrication*. (Wiley Online Library, 2013).

37. Dong, L., Yang, J., Chhowalla, M. & Loh, K. P. Synthesis and reduction of large sized graphene oxide sheets. *Chem. Soc. Rev.* **46**, 7306–7316 (2017).

38. Chen, J. *et al.* Synthesis of graphene oxide sheets with controlled sizes from sieved graphite flakes. *Carbon* **110**, 34–40 (2016).

39. Su, C.-Y. *et al.* Electrical and Spectroscopic Characterizations of Ultra-Large Reduced Graphene Oxide Monolayers. *Chem. Mater.* **21**, 5674–5680 (2009).

40. Jia, J., Kan, C.-M., Lin, X., Shen, X. & Kim, J.-K. Effects of processing and material parameters on synthesis of monolayer ultralarge graphene oxide sheets. *Carbon* **77**, 244–254 (2014).

41. Kim, D. W., Kim, D., Min, B. H., Lee, H. & Jung, H.-T. Sonication-free dispersion of large-area graphene oxide sheets using internal pressure from release of intercalated carbon dioxide. *Carbon* **88**, 126–132 (2015).

42. Ang, P. K., Wang, S., Bao, Q., Thong, J. T. L. & Loh, K. P. High-Throughput Synthesis of Graphene by Intercalation−Exfoliation of Graphite Oxide and Study of Ionic Screening in Graphene Transistor. *ACS Nano* **3**, 3587–3594 (2009).

43. Dong, L. *et al.* Reactivity-Controlled Preparation of Ultralarge Graphene Oxide by Chemical Expansion of Graphite. *Chem. Mater.* **29**, 564–572 (2017).

44. Lin, S., Dong, L., Zhang, J. & Lu, H. Room-Temperature Intercalation and ∼1000-Fold Chemical Expansion for Scalable Preparation of High-Quality Graphene. *Chem. Mater.* **28**, 2138–2146 (2016).

45. Stankovich, S. *et al.* Synthesis of graphene-based nanosheets via chemical reduction of exfoliated graphite oxide. *Carbon* **45**, 1558–1565 (2007).

46. Fernández-Merino, M. J. *et al.* Vitamin C Is an Ideal Substitute for Hydrazine in the Reduction of Graphene Oxide Suspensions. *J. Phys. Chem. C* **114**, 6426–6432 (2010).

47. Zhang, J. *et al.* Reduction of graphene oxide viaL-ascorbic acid. *Chem. Commun.* **46**, 1112–1114 (2010).

48. Moon, I. K., Lee, J., Ruoff, R. S. & Lee, H. Reduced graphene oxide by chemical graphitization. *Nat. Commun.* **1**, 73 (2010).

49. Schniepp, H. C. *et al.* Functionalized Single Graphene Sheets Derived from Splitting Graphite Oxide. *J. Phys. Chem. B* **110**, 8535–8539 (2006).

50. Xin, G. *et al.* Large-Area Freestanding Graphene Paper for Superior Thermal Management. *Adv. Mater.* **26**, 4521–4526 (2014).

51. Rozada, R., Paredes, J. I., Villar-Rodil, S., Martínez-Alonso, A. & Tascón, J. M. D. Towards full repair of defects in reduced graphene oxide films by two-step graphitization. *Nano Res.* **6**, 216–233 (2013).

52. Zhu, Y. *et al.* Microwave assisted exfoliation and reduction of graphite oxide for ultracapacitors. *Carbon* **48**, 2118–2122 (2010).

53. Agarwal, V. & Zetterlund, P. B. Strategies for reduction of graphene oxide – A comprehensive review. *Chem. Eng. J.* **405**, 127018 (2021).

54. Park, S. *et al.* Hydrazine-reduction of graphite- and graphene oxide. *Carbon* **49**, 3019–3023 (2011).

55. Pei, S., Zhao, J., Du, J., Ren, W. & Cheng, H.-M. Direct reduction of graphene oxide films into highly conductive and flexible graphene films by hydrohalic acids. *Carbon* **48**, 4466–4474 (2010).

56. Li, D., Müller, M. B., Gilje, S., Kaner, R. B. & Wallace, G. G. Processable aqueous dispersions of graphene nanosheets. *Nat. Nanotechnol.* **3**, 101–105 (2008).
57. Acik, M. & Chabal, Y. J. A review on thermal exfoliation of graphene oxide. *J. Mater. Sci. Res.* **2**, 101 (2013).
58. Botas, C. *et al.* Critical temperatures in the synthesis of graphene-like materials by thermal exfoliation–reduction of graphite oxide. *Carbon* **52**, 476–485 (2013).
59. Menéndez, J. A. *et al.* Microwave heating processes involving carbon materials. *Fuel Process. Technol.* **91**, 1–8 (2010).
60. Dideikin, A. T. & Vul', A. Y. Graphene Oxide and Derivatives: The Place in Graphene Family. *Front. Phys.* **6**, (2019).
61. Hernandez, Y. *et al.* High-yield production of graphene by liquid-phase exfoliation of graphite. *Nat. Nanotechnol.* **3**, 563–568 (2008).
62. Skaltsas, T., Ke, X., Bittencourt, C. & Tagmatarchis, N. Ultrasonication Induces Oxygenated Species and Defects onto Exfoliated Graphene. *J. Phys. Chem. C* **117**, 23272–23278 (2013).
63. Chauhan, D. S., Quraishi, M. A., Ansari, K. R. & Saleh, T. A. Graphene and graphene oxide as new class of materials for corrosion control and protection: Present status and future scenario. *Prog. Org. Coat.* **147**, 105741 (2020).
64. Parviz, D. *et al.* Dispersions of Non-Covalently Functionalized Graphene with Minimal Stabilizer. *ACS Nano* **6**, 8857–8867 (2012).
65. Texter, J. Graphene dispersions. *Curr. Opin. Colloid Interface Sci.* **19**, 163–174 (2014).

66. L. Moore, T. *et al.* Nanoparticle colloidal stability in cell culture media and impact on cellular interactions. *Chem. Soc. Rev.* **44**, 6287–6305 (2015).

67. Lozsán, A., García-Sucre, M. & Urbina-Villalba, G. Steric interaction between spherical colloidal particles. *Phys. Rev. E* **72**, 061405 (2005).

68. Johnson, D. W., Dobson, B. P. & Coleman, K. S. A manufacturing perspective on graphene dispersions. *Curr. Opin. Colloid Interface Sci.* **20**, 367–382 (2015).

69. Le Ba, T., Mahian, O., Wongwises, S. & Szilágyi, I. M. Review on the recent progress in the preparation and stability of graphene-based nanofluids. *J. Therm. Anal. Calorim.* **142**, 1145–1172 (2020).

70. Grimme, S. Do Special Noncovalent π–π Stacking Interactions Really Exist? *Angew. Chem. Int. Ed.* **47**, 3430–3434 (2008).

71. Zhang, M., Gao, B., Li, Y., Zhang, X. & Hardin, I. R. Graphene-coated pyrogenic carbon as an anode material for lithium battery. *Chem. Eng. J.* **229**, 399–403 (2013).

72. Heard, K. W. J. *et al.* Initial Studies Directed toward the Rational Design of Aqueous Graphene Dispersants. *ACS Omega* **4**, 1969–1981 (2019).

73. Shin, Y. *et al.* Enhanced liquid phase exfoliation of graphene in water using an insoluble bis-pyrene stabiliser. *Faraday Discuss.* **227**, 46–60 (2021).

74. McManus, D. *et al.* Water-based and biocompatible 2D crystal inks for all-inkjet-printed heterostructures. *Nat. Nanotechnol.* **12**, 343–350 (2017).

75. Saidina, D. S., Eawwiboonthanakit, N., Mariatti, M., Fontana, S. & Hérold, C. Recent Development of Graphene-Based Ink and Other Conductive Material-Based Inks for Flexible Electronics. *J. Electron. Mater.* **48**, 3428–3450 (2019).

76. Wajid, A. S. *et al.* Polymer-stabilized graphene dispersions at high concentrations in organic solvents for composite production. *Carbon* **50**, 526–534 (2012).
77. Jo, K. *et al.* Stable Aqueous Dispersion of Reduced Graphene Nanosheets via Non-Covalent Functionalization with Conducting Polymers and Application in Transparent Electrodes. *Langmuir* **27**, 2014–2018 (2011).
78. Karim, N. *et al.* All inkjet-printed graphene-based conductive patterns for wearable e-textile applications. *J. Mater. Chem. C* **5**, 11640–11648 (2017).
79. Sriprachuabwong, C. *et al.* Inkjet-printed graphene-PEDOT:PSS modified screen printed carbon electrode for biochemical sensing. *J. Mater. Chem.* **22**, 5478–5485 (2012).
80. Gao, Y., Shi, W., Wang, W., Leng, Y. & Zhao, Y. Inkjet Printing Patterns of Highly Conductive Pristine Graphene on Flexible Substrates. *Ind. Eng. Chem. Res.* **53**, 16777–16784 (2014).
81. Fan, X. *et al.* PEDOT:PSS for Flexible and Stretchable Electronics: Modifications, Strategies, and Applications. *Adv. Sci.* **6**, 1900813 (2019).
82. Jain, N., Singh, V. K. & Chauhan, S. A review on mechanical and water absorption properties of polyvinyl alcohol based composites/films. *J. Mech. Behav. Mater.* **26**, 213–222 (2017).
83. Hsieh, A. G., Korkut, S., Punckt, C. & Aksay, I. A. Dispersion Stability of Functionalized Graphene in Aqueous Sodium Dodecyl Sulfate Solutions. *Langmuir* **29**, 14831–14838 (2013).
84. BaoMin Wang & Ruying Zhao. Dispersion of Graphene in Aqueous Solution. *Russ. J. Phys. Chem. A* **92**, 1558–1562 (2018).

85. Smith, R. J., Lotya, M. & Coleman, J. N. The importance of repulsive potential barriers for the dispersion of graphene using surfactants. *New J. Phys.* **12**, 125008 (2010).

86. Hernandez, Y., Lotya, M., Rickard, D., Bergin, S. D. & Coleman, J. N. Measurement of Multicomponent Solubility Parameters for Graphene Facilitates Solvent Discovery. *Langmuir* **26**, 3208–3213 (2010).

87. Zu, S.-Z. *et al.* Supramolecular Surface Modification and Dispersion of Graphene in Water and Organic Solvents. *J. Nanosci. Nanotechnol.* **13**, 946–953 (2013).

88. Shih, C.-J., Lin, S., Strano, M. S. & Blankschtein, D. Understanding the Stabilization of Liquid-Phase-Exfoliated Graphene in Polar Solvents: Molecular Dynamics Simulations and Kinetic Theory of Colloid Aggregation. *J. Am. Chem. Soc.* **132**, 14638–14648 (2010).

89. Khan, U. *et al.* Solvent-Exfoliated Graphene at Extremely High Concentration. *Langmuir* **27**, 9077–9082 (2011).

90. Park, J. & Yan, M. Covalent Functionalization of Graphene with Reactive Intermediates. *Acc. Chem. Res.* **46**, 181–189 (2013).

91. Liu, Y. & Derby, B. Experimental study of the parameters for stable drop-on-demand inkjet performance. *Phys. Fluids* **31**, 032004 (2019).

92. L68P0Fujifilm20DimatixDMP280020User20Manual20v13.11464600.pdf.

93. Menon, E. S. *Transmission pipeline calculations and simulations manual*. (Gulf Professional Publishing, 2014).

94. Sieradzka, M., Ślusarczyk, C., Biniaś, W. & Fryczkowski, R. The Role of the Oxidation and Reduction Parameters on the Properties of the Reduced Graphene Oxide. *Coatings* **11**, 166 (2021).

95. Eda, G., Mattevi, C., Yamaguchi, H., Kim, H. & Chhowalla, M. Insulator to Semimetal Transition in Graphene Oxide. *J. Phys. Chem. C* **113**, 15768–15771 (2009).
96. Mattevi, C. *et al.* Evolution of Electrical, Chemical, and Structural Properties of Transparent and Conducting Chemically Derived Graphene Thin Films. *Adv. Funct. Mater.* **19**, 2577–2583 (2009).
97. Suk, J. W., Piner, R. D., An, J. & Ruoff, R. S. Mechanical Properties of Monolayer Graphene Oxide. *ACS Nano* **4**, 6557–6564 (2010).
98. Zheng, Q., Li, Z., Geng, Y., Wang, S. & Kim, J.-K. Molecular Dynamics Study of the Effect of Chemical Functionalization on the Elastic Properties of Graphene Sheets. *J. Nanosci. Nanotechnol.* **10**, 7070–7074 (2010).
99. Khoei, A. R. & Khorrami, M. S. Mechanical properties of graphene oxide: A molecular dynamics study. *Fuller. Nanotub. Carbon Nanostructures* **24**, 594–603 (2016).
100. Liu, L., Zhang, J., Zhao, J. & Liu, F. Mechanical properties of graphene oxides. *Nanoscale* **4**, 5910–5916 (2012).
101. Gao, W. *et al.* Effect of flake size on the mechanical properties of graphene aerogels prepared by freeze casting. *RSC Adv.* **7**, 33600–33605 (2017).
102. Wassei, J. K. & Kaner, R. B. Graphene, a promising transparent conductor. *Mater. Today* **13**, 52–59 (2010).
103. Cao, L., Sahu, S., Anilkumar, P., Kong, C. Y. & Sun, Y.-P. Linear and nonlinear optical properties of modified graphene-based materials. *MRS Bull.* **37**, 1283–1289 (2012).
104. Yan, H. *et al.* Infrared Spectroscopy of Wafer-Scale Graphene. *ACS Nano* **5**, 9854–9860 (2011).

105. Xie, S. *et al.* Graphene Oxide Transparent Hybrid Film and Its Ultraviolet Shielding Property. *ACS Appl. Mater. Interfaces* **7**, 17558–17564 (2015).

106. Tang, Y., Gao, P., Wang, M., Zhu, J. & Wan, X. A novel glycopolymeric ultraviolet absorber covering UV-A and UV-B ranges. *RSC Adv.* **4**, 22617–22620 (2014).

107. Shen, Y. *et al.* Evolution of the band-gap and optical properties of graphene oxide with controllable reduction level. *Carbon* **62**, 157–164 (2013).

108. Kong, D., Le, L. T., Li, Y., Zunino, J. L. & Lee, W. Temperature-Dependent Electrical Properties of Graphene Inkjet-Printed on Flexible Materials. *Langmuir* **28**, 13467–13472 (2012).

109. Rogala, M. *et al.* Graphene oxide overprints for flexible and transparent electronics. *Appl. Phys. Lett.* **106**, 041901 (2015).

110. Kim, H. *et al.* Sheet Size-Induced Evaporation Behaviors of Inkjet-Printed Graphene Oxide for Printed Electronics. *ACS Appl. Mater. Interfaces* **8**, 3193–3199 (2016).

111. Dua, V. *et al.* All-Organic Vapor Sensor Using Inkjet-Printed Reduced Graphene Oxide. *Angew. Chem. Int. Ed.* **49**, 2154–2157 (2010).

112. Lim, S. *et al.* Inkjet-Printed Reduced Graphene Oxide/Poly(Vinyl Alcohol) Composite Electrodes for Flexible Transparent Organic Field-Effect Transistors. *J. Phys. Chem. C* **116**, 7520–7525 (2012).

113. Lian, H., Qi, L., Luo, J. & Zhang, R. Drop-on-demand printing of edge-enhanced and conductive graphene twin-lines by coalescence regulation and multi-layers overwriting. *2D Mater.* **8**, 035004 (2021).

114. Derby, B. Inkjet printing of functional and structural materials: fluid property requirements, feature stability, and resolution. *Annu. Rev. Mater. Res.* **40**, 395–414 (2010).

115. Torrisi, F. *et al.* Inkjet-Printed Graphene Electronics. *ACS Nano* **6**, 2992–3006 (2012).

116. de Gans, B.-J., Duineveld, P. C. & Schubert, U. S. Inkjet Printing of Polymers: State of the Art and Future Developments. *Adv. Mater.* **16**, 203–213 (2004).

117. Li, J., Rossignol, F. & Macdonald, J. Inkjet printing for biosensor fabrication: combining chemistry and technology for advanced manufacturing. *Lab. Chip* **15**, 2538–2558 (2015).

118. Martin, G. D., Hoath, S. D. & Hutchings, I. M. Inkjet printing - the physics of manipulating liquid jets and drops. *J. Phys. Conf. Ser.* **105**, 012001 (2008).

119. Jang, D., Kim, D. & Moon, J. Influence of Fluid Physical Properties on Ink-Jet Printability. *Langmuir* **25**, 2629–2635 (2009).

120. Shimoda, T., Morii, K., Seki, S. & Kiguchi, H. Inkjet Printing of Light-Emitting Polymer Displays. *MRS Bull.* **28**, 821–827 (2003).

121. Cummins, G. & Desmulliez, M. P. Y. Inkjet printing of conductive materials: a review. *Circuit World* **38**, 193–213 (2012).

122. Pai, M., Bermejo-Moreno, I., Desjardins, O. & Pitsch, H. Role of Weber number in the primary breakup of liquid jets in crossflow. **62**, LK.009 (2009).

123. McKinley, G. H. & Renardy, M. Wolfgang von Ohnesorge. *Phys. Fluids* **23**, 127101 (2011).

124. Reis, N. & Derby, B. Ink Jet Deposition of Ceramic Suspensions: Modeling and Experiments of Droplet Formation. *MRS Online Proc. Libr. OPL* **625**, (2000).

125. Hill, T. Y., Reitz, T. L., Rottmayer, M. A. & Huang, H. Controlling Inkjet Fluid Kinematics to Achieve SOFC Cathode Micropatterns. *ECS J. Solid State Sci. Technol.* **4**, P3015 (2015).

126. Duineveld, P. C. *et al.* Ink-jet printing of polymer light-emitting devices. in *Organic Light-Emitting Materials and Devices V* vol. 4464 59–67 (SPIE, 2002).

127. Tanner, L. H. The spreading of silicone oil drops on horizontal surfaces. *J. Phys. Appl. Phys.* **12**, 1473–1484 (1979).

128. Stringer, J. & Derby, B. Formation and Stability of Lines Produced by Inkjet Printing. *Langmuir* **26**, 10365–10372 (2010).

129. Soltman, D. & Subramanian, V. Inkjet-Printed Line Morphologies and Temperature Control of the Coffee Ring Effect. *Langmuir* **24**, 2224–2231 (2008).

130. Beedasy, V. & Smith, P. J. Printed Electronics as Prepared by Inkjet Printing. *Materials* **13**, 704 (2020).

131. Sadek, C. *et al.* Drying of a single droplet to investigate process–structure–function relationships: a review. *Dairy Sci. Technol.* **95**, 771–794 (2015).

132. Deegan, R. D. *et al.* Capillary flow as the cause of ring stains from dried liquid drops. *Nature* **389**, 827–829 (1997).

133. Deegan, R. D. *et al.* Contact line deposits in an evaporating drop. *Phys. Rev. E* **62**, 756–765 (2000).

134. Parsa, M., Harmand, S. & Sefiane, K. Mechanisms of pattern formation from dried sessile drops. *Adv. Colloid Interface Sci.* **254**, 22–47 (2018).

135. Zhang, Y., Yang, S., Chen, L. & Evans, J. R. G. Shape Changes during the Drying of Droplets of Suspensions. *Langmuir* **24**, 3752–3758 (2008).

136. Chen, S.-P., Chiu, H.-L., Wang, P.-H. & Liao, Y.-C. Inkjet Printed Conductive Tracks for Printed Electronics. *ECS J. Solid State Sci. Technol.* **4**, P3026 (2015).

137. Fukuda, K., Sekine, T., Kumaki, D. & Tokito, S. Profile Control of Inkjet Printed Silver Electrodes and Their Application to Organic Transistors. *ACS Appl. Mater. Interfaces* **5**, 3916–3920 (2013).

138. Gugliotti, M., Baptista, M. S., Politi, M. J., Todd P. Silverstein, & Carl D. Slater. Surface Tension Gradients Induced by Temperature: The Thermal Marangoni Effect. *J. Chem. Educ.* **81**, 824 (2004).

139. Lim, J. A. *et al.* Self-Organization of Ink-jet-Printed Triisopropylsilylethynyl Pentacene via Evaporation-Induced Flows in a Drying Droplet. *Adv. Funct. Mater.* **18**, 229–234 (2008).

140. Paredes, J. I., Villar-Rodil, S., Solís-Fernández, P., Martínez-Alonso, A. & Tascón, J. M. D. Atomic Force and Scanning Tunneling Microscopy Imaging of Graphene Nanosheets Derived from Graphite Oxide. *Langmuir* **25**, 5957–5968 (2009).

141. Dhar, P. *et al.* Percolation network dynamicity and sheet dynamics governed viscous behavior of polydispersed graphene nanosheet suspensions. *J. Nanoparticle Res.* **15**, 2095 (2013).

142. Borecki, M., Korwin-Pawlowski, M. L., Beblowska, M., Szmidt, J. & Jakubowski, A. Optoelectronic Capillary Sensors in Microfluidic and Point-of-Care Instrumentation. *Sensors* **10**, 3771–3797 (2010).
143. Guo, Y., Patanwala, H. S., Bognet, B. & Ma, A. W. K. Inkjet and inkjet-based 3D printing: connecting fluid properties and printing performance. *Rapid Prototyp. J.* **23**, 562–576 (2017).
144. O' Mahony, C., Haq, E. U., Silien, C. & Tofail, S. A. M. Rheological Issues in Carbon-Based Inks for Additive Manufacturing. *Micromachines* **10**, 99 (2019).
145. Nahid, M. M. *In Quest of Printed Electrodes for Light-emitting Electrochemical Cells: A Comparative Study between Two Silver Inks*. (2012).
146. Tang, Z., Fang, K., Bukhari, M. N., Song, Y. & Zhang, K. Effects of Viscosity and Surface Tension of a Reactive Dye Ink on Droplet Formation. *Langmuir* **36**, 9481–9488 (2020).
147. Chen, A. U. & Basaran, O. A. A new method for significantly reducing drop radius without reducing nozzle radius in drop-on-demand drop production. *Phys. Fluids* **14**, L1–L4 (2002).
148. Hamad, A., Archacki, A. & Mian, A. Characteristics of nanosilver ink (UTDAg) microdroplets and lines on polyimide during inkjet printing at high stage velocity. *Mater. Adv.* **1**, 99–107 (2020).
149. Miccichè, C. *et al.* Inkjet printing Ag nanoparticles for SERS hot spots. *Anal. Methods* **10**, 3215–3223 (2018).

150. Arrabito, G. *et al.* Monitoring few molecular binding events in scalable confined aqueous compartments by raster image correlation spectroscopy (CADRICS). *Lab. Chip* **16**, 4666–4676 (2016).
151. Krainer, S., Smit, C. & Hirn, U. The effect of viscosity and surface tension on inkjet printed picoliter dots. *RSC Adv.* **9**, 31708–31719.
152. Jun, H.-Y., Kim, S.-J. & Choi, C.-H. Ink Formulation and Printing Parameters for Inkjet Printing of Two Dimensional Materials: A Mini Review. *Nanomaterials* **11**, 3441 (2021).
153. Calvert, P. Inkjet Printing for Materials and Devices. *Chem. Mater.* **13**, 3299–3305 (2001).
154. Li, Y., Lv, C., Li, Z., Quéré, D. & Zheng, Q. From coffee rings to coffee eyes. *Soft Matter* **11**, 4669–4673 (2015).
155. Li, Y., Yang, Q., Li, M. & Song, Y. Rate-dependent interface capture beyond the coffee-ring effect. *Sci. Rep.* **6**, 24628 (2016).
156. Mampallil, D. & Eral, H. B. A review on suppression and utilization of the coffee-ring effect. *Adv. Colloid Interface Sci.* **252**, 38–54 (2018).
157. Yang, M. *et al.* The application of coffee-ring effect in analytical chemistry. *TrAC Trends Anal. Chem.* **157**, 116752 (2022).
158. Yang, J., Zheng, F. & Derby, B. Stability of Lines with Zero Receding Contact Angle Produced by Inkjet Printing at Small Drop Volume. *Langmuir* **37**, 26–34 (2021).
159. Duineveld, P. C. The stability of ink-jet printed lines of liquid with zero receding contact angle on a homogeneous substrate. *J. Fluid Mech.* **477**, 175–200 (2003).

160. Tao, Z., Le Borgne, B., Mohammed-Brahim, T., Jacques, E. & Harnois, M. Spreading and drying impact on printed pattern accuracy due to phase separation of a colloidal ink. *Colloid Polym. Sci.* **296**, 1749–1758 (2018).

161. Dinh, N. T. *et al.* High-resolution inkjet printing of conductive carbon nanotube twin lines utilizing evaporation-driven self-assembly. *Carbon* **96**, 382–393 (2016).

162. Abunahla, R., Rahman, M. S., Naderi, P. & Grau, G. Improved Inkjet-Printed Pattern Fidelity: Suppressing Bulges by Segmented and Symmetric Drop Placement. *J. Micro Nano-Manuf.* **8**, (2020).

163. Walsh, E. J. *et al.* Microfluidics with fluid walls. *Nat. Commun.* **8**, 816 (2017).

164. Lim, G.-H. *et al.* A transition solvent strategy to print polymer:fullerene films using halogen-free solvents for solar cell applications. *Org. Electron.* **15**, 449–460 (2014).

165. Chandra, S., di Marzo, M., Qiao, Y. M. & Tartarini, P. Effect of liquid-solid contact angle on droplet evaporation. *Fire Saf. J.* **27**, 141–158 (1996).

166. Panwar, A. K., Barthwal, S. K. & Ray, S. Effect of evaporation on the contact angle of a sessile drop on solid substrates. *J. Adhes. Sci. Technol.* **17**, 1321–1329 (2003).

167. Zhong, X., Crivoi, A. & Duan, F. Sessile nanofluid droplet drying. *Adv. Colloid Interface Sci.* **217**, 13–30 (2015).

168. Shao, X., Duan, F., Hou, Y. & Zhong, X. Role of surfactant in controlling the deposition pattern of a particle-laden droplet: Fundamentals and strategies. *Adv. Colloid Interface Sci.* **275**, 102049 (2020).

169. Bera, B. *et al.* Antisurfactant (Autophobic) Behavior of Superspreader Surfactant Solutions. *Langmuir* **37**, 6243–6247 (2021).
170. Sempels, W., De Dier, R., Mizuno, H., Hofkens, J. & Vermant, J. Auto-production of biosurfactants reverses the coffee ring effect in a bacterial system. *Nat. Commun.* **4**, 1757 (2013).
171. Prediger, P. *et al.* Graphene oxide nanomaterials for the removal of non-ionic surfactant from water. *J. Environ. Chem. Eng.* **6**, 1536–1545 (2018).
172. Crivoi, A. & Duan, F. Effect of Surfactant on the Drying Patterns of Graphite Nanofluid Droplets. *J. Phys. Chem. B* **117**, 5932–5938 (2013).
173. Anyfantakis, M. & Baigl, D. Manipulating the Coffee-Ring Effect: Interactions at Work. *ChemPhysChem* **16**, 2726–2734 (2015).
174. Zhang, W., Yu, T., Liao, L. & Cao, Z. Ring formation from a drying sessile colloidal droplet. *AIP Adv.* **3**, 102109 (2013).
175. Talbot, E. L., Berson, A., Yang, L. & Bain, C. D. Internal flows and particle transport inside picoliter droplets of binary solvent mixtures. in *NIP & digital fabrication conference.* vol. 2013 307–312 (Society for Imaging Science and Technology, 2013).
176. Talbot, E. L., Berson, A. & Bain, C. D. Drying and deposition of picolitre droplets of colloidal suspensions in binary solvent mixtures. in *NIP & Digital Fabrication Conference* vol. 2012 420–423 (Society for Imaging Science and Technology, 2012).
177. Lee, H. H., Fu, S. C., Tso, C. Y. & Chao, C. Y. H. Study of residue patterns of aqueous nanofluid droplets with different particle sizes and concentrations on different substrates. *Int. J. Heat Mass Transf.* **105**, 230–236 (2017).

178. Moffat, J. R., Sefiane, K. & Shanahan, M. E. R. Nanofluid Droplet Evaporation Kinetics and Wetting Dynamics on Flat Substrates. *J. Nano Res.* **7**, 75–80 (2009).

179. Sefiane, K. On the Formation of Regular Patterns from Drying Droplets and Their Potential Use for Bio-Medical Applications. *J. Bionic Eng.* **7**, S82–S93 (2010).

Appendix

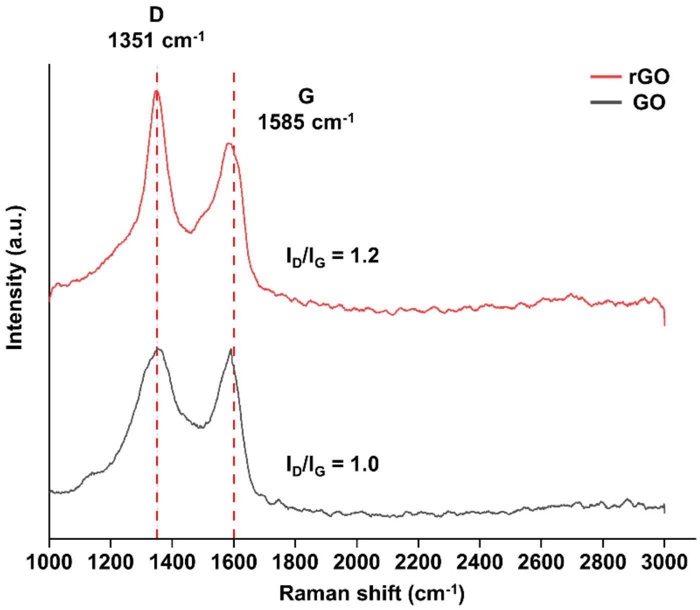

Figure S 1 The Raman results of GO and rGO without stabiliser reduced at 80°C for 72 hours by L–AA. The I_D/I_G increases from 1.0 to 1.2 after the reduction process. This increase indicates a higher ratio of sp^2 domain in the rGO, which proves the restoration of graphene structure after the reduction.

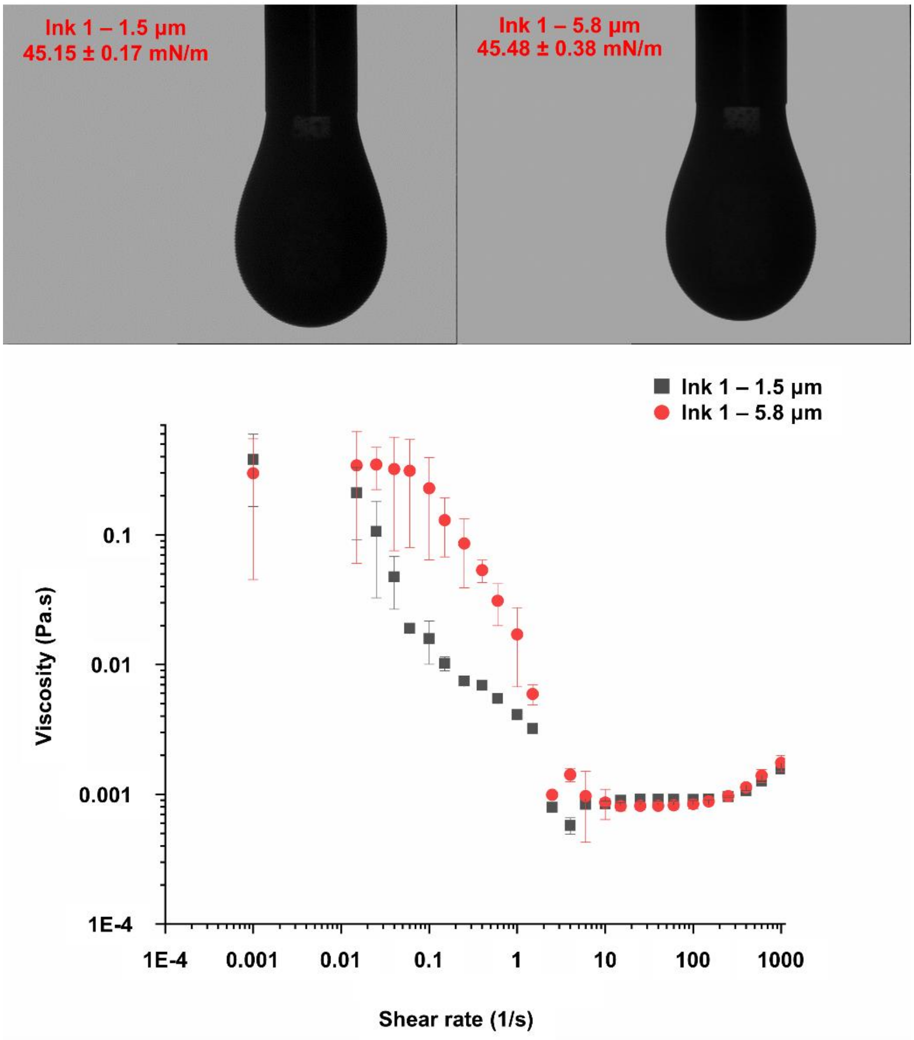

Figure S 2 The graphs of the surface tension and viscosity of Ink 1–(0.25rGO, 0.1/1EG, 0.1Tri)–1.5µm and Ink 1–(0.25rGO, 0.1/1EG, 0.1Tri)–5.8µm. The average surface tensions of Ink 1 – 1.5 µm and Ink 1 – 5.8 µm are 45.15 ± 0.17 mN/m and 45.58 ± 0.38 m/Nm. The average viscosities of these two inks are 1.57 ± 0.01 mPa.s and 1.75 ± 0.25 mPa.s at 1000 1/s.

No.	Ink formulation	Surface tension (mN/m)	Viscosity (mPa.s)	Density (mg/µl)	Re	We	Z
1	0.25 rGO, 0.1/1 EG/DI, 0.1 Tri, 1.5 µm	45.15 ± 0.17	1.57 ± 0.01	1	82.17	17.14	19.84
2	0.25 rGO, 1/1 EG/DI, 0.1 Tri, 1.5 µm	43.14 ± 0.13	1.80 ± 0.01	1	71.67	17.94	16.92
3	0.5 rGO, 1/1 EG/DI, 0.2 Tri, 1.5 µm	44.26 ± 1.23	2.06 ± 0.01	1	62.62	17.49	14.97
4	0.5 rGO, 0/1 EG/DI, 0.2 Tri, 1.5 um	46.68 ± 2.40	1.72 ± 0.01	1	75.00	16.58	18.42
5	1 rGO, 0/1 EG/DI, 0.2 Tri, 1.5 µm	48.27 ± 1.90	1.80 ± 0.01	1	71.67	16.03	17.90
6	1 rGO, 0/1 EG, 0.3 Tri, 1.5 um	44.56 ± 2.09	1.81 ± 0.01	1	71.27	17.37	17.10
7	1 rGO, 0/1 EG, 0.3 Tri, 6.5 um	45.06 ± 1.93	1.90 ± 0.06	1	67.89	17.17	16.38

Table S 1 The rheological properties and Z numbers of seven inks. All the inks have Z numbers larger than 10, which indicate the damping effect of these inks are not strong enough to supress the Rayleigh instability.

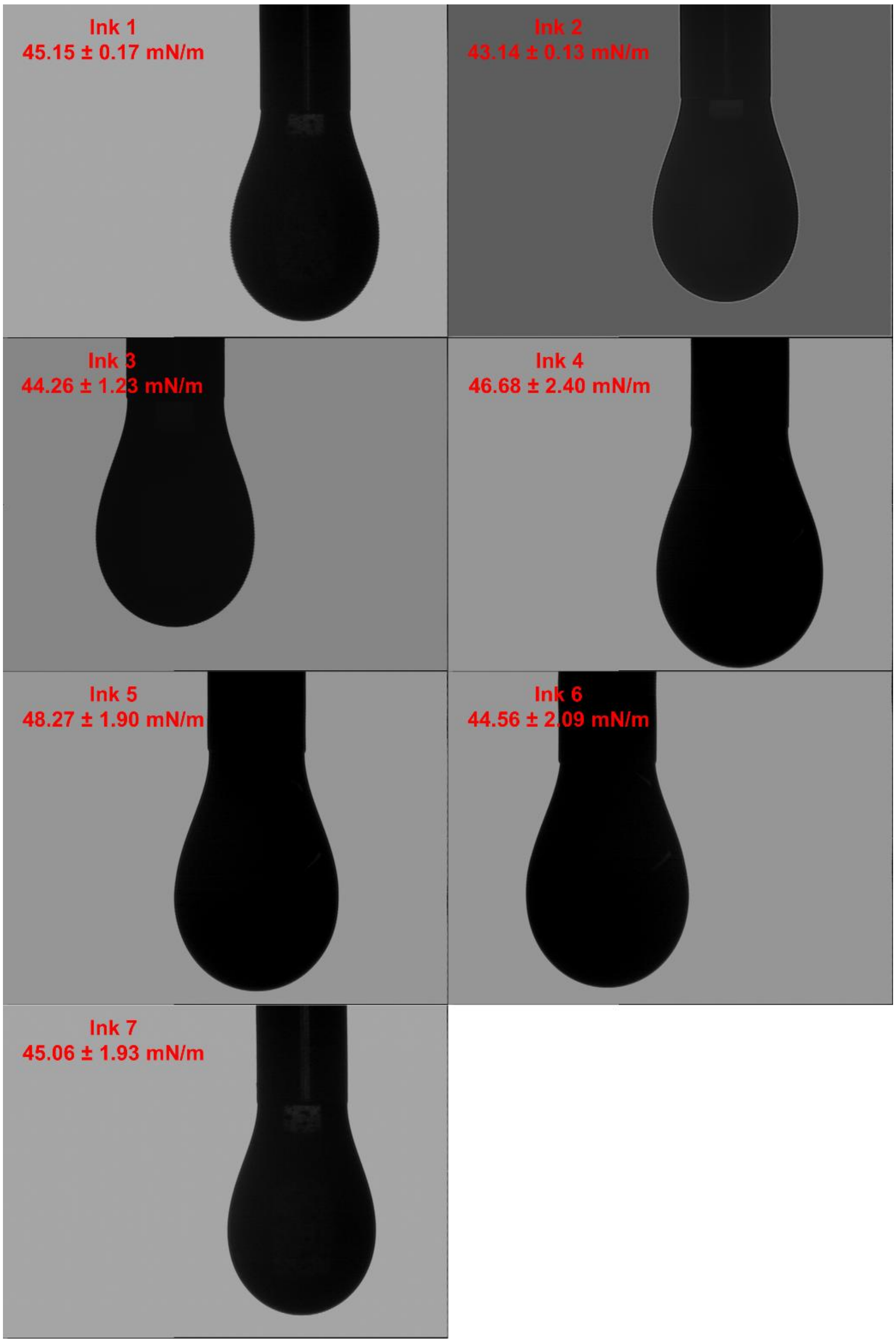

Figure S 3 The graphs of the surface tension of seven inks. All the inks have the surface tensions close to that of ideal fluid for DMP-2831 printer (28 – 42 mN/m at printing temperature).

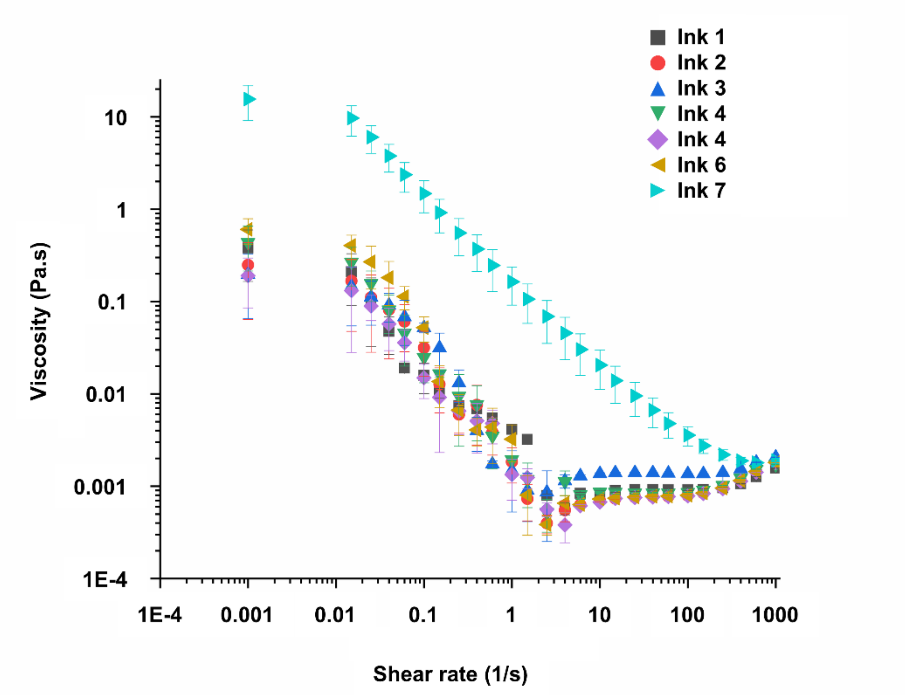

Figure S 4 The graphs of the viscosity of seven inks. All the inks have the viscosities around 2 mPa.s at 1000 1/s, which much less than that of ideal fluid for DMP-2831 printer (10 – 12 mPa.s at printing temperature).